PHYSIK-DEPARTMENT

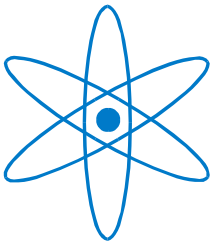

Nonlinear Phenomena during Bulk CO Electrooxidation on Pt Electrodes

Dissertation

von

Souradip Malkhandi

TECHNISCHE UNIVERSITÄT

MÜNCHEN

Technische Universität München
Fakultät für Physik
Lehrstuhl für Grenzflächen und Energieumwandlung E19

Nonlinear Phenomena during Bulk CO Electrooxidation on Pt Electrodes

Souradip Malkhandi

Vollständiger Abdruck der von der Fakultät für Physik der Technischen Universität München zur Erlangung des akademischen Grades eines

Doktors der Naturwissenschaften (Dr. rer. nat.)

genehmigten Dissertation.

Vorsitzender: Univ.-Prof. Dr. Ralf Metzler

Prüfer der Dissertation:

1. Univ.-Prof. Dr. Katharina Krischer
2. Prof. D. Sci. Elena R. Savinova,
   Université Louis Pasteur, Straßburg/Frankreich

Die Dissertation wurde am 11.08.2008 bei der Technischen Universität München eingereicht und durch die Fakultät für Physik am 23.10.2008 angenommen.

Abstract

This experimental thesis deals with cooperative phenomena that occur during the electrodissolution of CO on Pt electrodes. Three aspects are considered. Using a self-designed electronic control device, evidence for the existence of a postulated chemical positive feedback loop in the reaction mechanism is obtained. Measurements at both, low concentration of supporting electrolyte and low CO bulk concentration yielded information about the competitive adsorption of CO, OH and anions. Thereby, conditions could be established that promoted CO oxidation at surprisingly low potentials. Further, the interaction of strongly adsorbing anions with the elementary steps of CO electrooxidation is shown to cause an oscillatory instability in wide parameter ranges. The oscillations are chemical in nature and present the first experimental example of a so-called strictly potentiostatic oscillator where the electrode potential acts as a parameter.

Zusammenfassung

In dieser Arbeit werden kooperative Phänomene, die bei der Elektrooxidation von CO an Platinelektroden auftreten, untersucht. Mithilfe einer Rückkopplungskontrolle wird die Existenz einer positiven Rückkopplungsschleife im Reaktionsmechanismus nachgewiesen. Messungen bei niedrigen Konzentrationen von Leitelektrolyten und CO liefern Information über Wechselwirkungen bei der Adsorption von CO, OH and Anionen. Hierbei werden Bedingungen identifiziert, die die Oxidation von CO bei erstaunlich niedrigen Potentialen begünstigen. Des Weiteren wird gezeigt, dass die Wechselwirkung von stark adsorbierenden Anionen mit den Elementarschritten der CO-Elektrooxidation in weiten Parameterbereichen zu einer oszillatorischen Instabilität führt. Die Oszillationen entstehen aufgrund des Wechselspiels zweier chemischer Rückkopplungsschleifen und stellen das erste experimentelle Beispiel eines so genannten strikt potentiostatischen Oszillators dar.

Contents

Chapter 1: Introduction

CO electrooxidation is among the most intensively studied electro-catalytic reactions [1-4]; yet, it still receives unbroken attention. This outstanding position reflects its fundamental and practical importance. CO as a relatively simple molecule has served as a prototype system for studies of chemisorption phenomena and of electron, proton and oxygen transfer processes [5, 6]. It is an intermediate in the electrooxidation of most organic molecules, starting with the next simple C1-species formic acid or formaldehyde. Understanding the basic steps of CO electrooxidation is thus also the first step towards a better understanding of electrooxidation of many other organic compounds. Furthermore, it is a contaminant in industrial hydrogen or hydrogen feed streams from carbon-based fuels (e.g. reformed natural gas or methanol), but even traces of CO cause a dramatic deactivation of an Pt anode, which is the most active catalyst for hydrogen electrooxidation. Thus, Pt anodes in low-temperature fuel cells suffer from unacceptable high overpotentials. Therefore, a thorough understanding of CO electrooxidation is also of foremost importance in the development of improved low temperature fuel cells. This thesis aims at making a contribution to a better understanding of the dynamics of this reaction.

Most of the more recent studies of CO electrooxidation on Pt have employed a surface science approach and have focused on microscopic structural features and elementary steps. Investigations have been done with single-crystals, utilizing in-situ electrochemical measurements such as 'classical' potentiodynamic techniques [5-21], scanning tunnelling microscopy [22-24], Fourier transform infrared spectroscopy [25-37], surface x-ray scattering [18, 38, 39], sum frequency generation [40, 41] as well as ex-situ surface science techniques on emersed electrodes in UHV [42, 43]. Initially, mainly so-called stripping experiments were performed, i.e. CO was adsorbed on the

electrode from CO-containing electrolytes and then the CO dissolved in the electrolyte was driven out by purging the electrolyte with argon. Subsequently, the electrooxidation or 'stripping' of the adsorbed CO molecules was studied [6, 44]. More recent experiments also involve steady state conditions, i.e. CO remains dissolved in the bulk of the electrolyte while adsorbed CO is oxidized [26, 45-47]. This type of experiments is often referred to as CO bulk electrooxidation. A comprehensive review of all these studies can be found in [3].

Besides many details on microscopic structural features and structure reactivity relationships, which differ for different electrode orientations, the studies revealed that independent of the surface structure the main route through which CO is oxidized is a simple Langmuir Hinshelwood surface reaction. This means that adsorbed CO is oxidized by reacting with a second adsorbed species, which is either OH or activated water, depending on the electrode potential and other experimental conditions. Thus, there is a competition of CO and OH (or water) for free surface sites. In a wide parameter range, this feature causes the occurrence of an autocatalytic or positive feedback loop, which in turn promotes dynamic instabilities. In fact, bistability between high and low current branches has been observed, the most fundamental manifestation of a self-enhancing reaction cycle [45, 48].

Bistability is one example of a dynamic instability. In general, dynamics instabilities may arise in open systems that are kept far from thermodynamic equilibrium [49-60]. They are studied in the interdisciplinary field of Nonlinear Dynamics and always involve cooperative phenomena. This implies that the system's behaviour cannot be understood by studying only the properties of the individual molecules making up the system. Rather, the behaviour is determined by nonlinear interactions between the system's variables, thus impeding a description that is based on any linear approximation. Therefore, also CO electrooxidation cannot be fully understood without studying the interaction of all the different reactions *and transport steps*. However, so far, despite the many studies on CO electrooxidation, this 'nonlinear point of view' has hardly been taken. Besides the above mentioned reports of bistability, there are only very few further publications in which attention was paid to nonlinear behaviour [61-63]. Azevedo et al. [63] observe oscillatory current densities, however, without being able to offer a plausible explanation for the oscillatory instability. Oscillations under galvanostatic conditions are reported in [45], but again their origin is unsolved. Bonnefont et al. [61] demonstrate that the positive feedback cycle can lead to a Turing instability, and thus to

spatially inhomogeneous adsorbate distributions if the electrolyte resistance exceeds a critical value. Also from a different perspective can the study of diluted supporting electrolytes contribute to an understanding of the dynamics of CO electrooxidation. Often it is assumed that the supporting electrolyte only ensures that the electrolyte is conductive, but does not chemically interact with the electrode surface. However, this picture is strongly idealized. Most anions adsorb to some extent on the electrode surface. This is also true for the most frequently used anions of the base electrolyte, namely sulphate and perchlorate, though to a very different extent. While sulphate ions are known to strongly adsorb on Pt electrodes, the interaction between perchlorate ions and most noble metal surfaces is much weaker. However, any adsorption of anions on the electrode will reduce the number of free surface sites for CO electrooxidation. Thus, not only CO and OH but also anions compete for free surface sites. The importance of anions for the mechanism of CO electrooxidation has been pointed out in some papers [17, 20, 64], but a systematic study is still missing. Hence, it is also unknown whether the interaction can be reduced to a pure Langmuirian one, i.e. is restricted to the competition for free adsorption sites, or whether there are attractive or repulsive interactions between anions and adsorbed CO and OH molecules. But in any case, the interaction between anion dynamics and CO and OH dynamics might introduce further feedback loops or alter the effect of existing ones and thus might lead to fundamentally different dynamic instabilities, a point of view that had been completely neglected before the beginning of this thesis.

The goal of this thesis was to study CO electrooxidation on Pt from a nonlinear dynamics point of view, with special emphasis on the role of anion adsorption for the dynamic instabilities. In particular, the following questions were addressed:

1) Can the above mentioned positive feedback loop in the dynamics of CO electrooxidation be proven in independent experiments?

This seemed to be of particular importance, since the postulated feedback loop is of chemical nature. This is in contrast to almost all oscillating electrochemical systems whose dynamic instabilities were shown to be linked to a self-enhancing feedback loop of the electrode potential. Thus, the autocatalytic cycle of these systems is of electrical rather than chemical nature, leading to qualitatively different dynamic manifestations.

2) Does the interaction of anions with CO and OH adsorption lead to qualitatively different behaviour or to so-far uncovered cooperative effects? This is a comprehensive

problem, which comprises several aspects, such as: What is the role of the surface structure? Does the nature of the anion matter for the qualitative behaviour?

The first question obviously requires experiments with single crystals. To approach the second one, experiments with anions with widely different adsorption strengths have to be carried out. One aspect of all studies of CO electrooxidation is also to understand under which conditions CO electrooxidation causes the least poisoning effect, and thus in a fuel cell the least overpotential at the anode. Hence, in our context we would like to deduce the relative concentrations of CO, OH and anions that support the most negative electrode potentials at which CO is still oxidized. Here, conditions that have received only little attention so far seem to be promising, namely, low concentrations of both, the electrolyte and dissolved CO.

These questions are addressed in chapters 4-6 below and are preceded by a concise introduction to those basic concepts of nonlinear dynamics and electrochemistry that are essential for an understanding of the following chapters (chapter 2) and a description of the experimental set-up and methods employed (chapter 3). In chapter 4, it is shown that oscillations during CO electrooxidation can be induced by using a feedback control scheme that changes the effective electrode capacitance, proving the existence of the chemical positive feedback loop. Chapter 5 deals with CO electrooxidation in diluted electrolytes and low CO bulk concentrations on single crystal electrodes. In section 5.1 surprisingly low, though transient, onset-potentials of CO electrooxidation are discussed. Section 5.2 concentrates on stationary electrooxidation rates and discusses conditions under which the potential that still supports steady reaction rates in the bistable region is minimized. In chapter 6, CO electrooxidation is studied in concentrated supporting electrolytes (0.5 M H_2SO_4 and 0.5 M $HClO_4$) that contain small amounts of strongly adsorbing anions, such as halides. It is shown that these anions introduce a further feedback loop and thus alter the dynamics of the system qualitatively. The behaviour on poly-crystalline Pt electrodes is compared with the one of the three low-indexed single crystal surfaces. Chapter 7, finally, summarizes the main results and gives an outlook of future challenges that have to be tackled to eventually have full control over the CO electrooxidation reaction.

Chapter 2: Background

In this chapter, a brief introduction to electrochemistry, nonlinear dynamical systems, nonlinear dynamics of electrochemical systems and CO electrooxidation on platinum is given; hereby only those aspects are considered that form the basis of the following chapters.

2.1 The electrochemical interface & electrochemistry

2.1.1 The electrochemical interface

One of the primary concerns of electrochemistry is how a charge transfer process takes place across the electrode|electrolyte interface. The interface is the region in which characteristic properties, most importantly the electrostatic potential, differ from their values in the two bulk volume phases.

It is experimentally found that an electrode|electrolyte interface behaves like a capacitor when no charge transfer across the interface takes place [65, 66]. The interface is the region in which free net charge accumulates. The charges on the electrode represent an excess or deficiency of electrons and reside in a thin layer of less than 0.1 Å. The charges in the solution are made of an excess of either cations or anions near the electrode surface. This interfacial region is called electrical double layer [67-70]. The solution side of the double layer can be modelled as several parallel layers [71-73], which are shown in Figure 2.1. The layer closest to the electrode contains solvent molecules and specifically adsorbed species, which can be ions or neutral molecules.

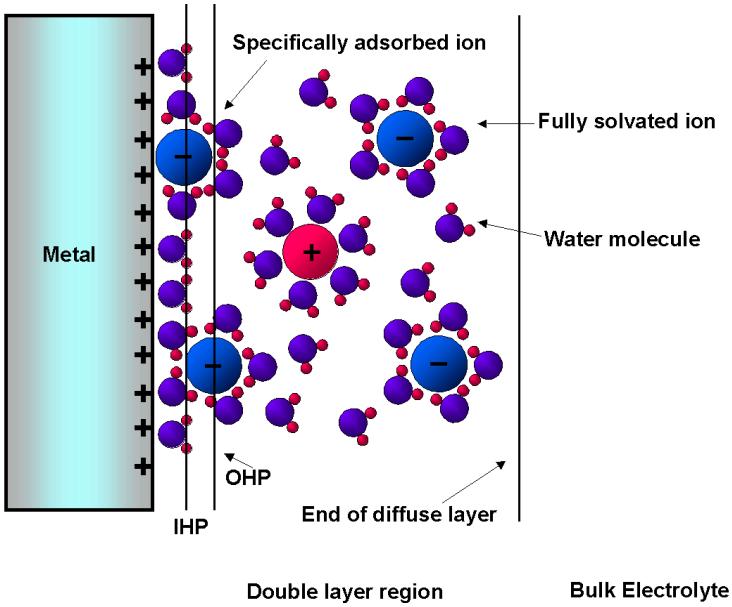

Figure 2.1: Double layer region of an electrochemical interface. Large blue and red circles indicate anions and cations, respectively. Small blue circles with two red points attach denote water molecules, where the blue circle symbolizes the oxygen atom and red points the hydrogen atoms. 'IHP' and 'OHP' stand for inner and outer Helmholtz plane, respectively.

The plane through the electrical centre of the specifically adsorbed species is designated as inner Helmholtz plane (IHP). The plane next to the IHP is the plane of nearest approach of solvated ions and is referred to as outer Helmholtz plane (OHP). The interaction of solvated ions with the electrode is usually independent of the chemical nature of ions and therefore these ions are denoted as non-specifically adsorbed ions. IHP and OHP together form the Helmholtz layer. When the electrolyte concentration is low i.e. the charge carrier density in the electrolyte is low, the space charge region extends into the electrolyte beyond the OHP because of the counter acting entropic and electrostatic forces. This third 'layer' is called diffuse layer. Its extension depends on the ionic strength of the electrolyte. It diminishes for a highly concentrated electrolyte and extends over several 10 nm for ion concentrations $< 10^{-3}$ M.

A theoretical description of the double layer structure was first proposed by Helmholtz [74, 75], who modelled it as a simple parallel plate capacitor. A limitation of this model is that it predicts the double layer capacitance to be constant while experimental results show that the latter varies with the electrode potential and the ion concentration. Independently from each other Gouy and Chapman [76, 77] developed a theory that incorporates the concept of the diffuse layer of charge considering the attraction or

repulsion of ions to or from the electrode (depending on their polarity) and randomisation due to thermal motion. These considerations yield the Poisson Boltzmann equation

$$\nabla^2\phi = -\frac{e}{\varepsilon_r\varepsilon_0}\sum_i n_i z_i e^{\frac{-z_i e\phi}{kT}} \tag{2.1}$$

where ϕ is the electrostatic potential, e the electronic charge, k the Boltzmann constant, T the absolute temperature, n_i the bulk concentration of ith ion with charge number z_i, ε_0 the permittivity of the vacuum and ε_r the relative permittivity of the solution. Considering a plane electrode and an electrolyte that consists of one anionic and one cationic species with both charge number z, the potential distribution at a distance x from the electrode (i.e. the solution of equation 2.1.) is given by

$$\frac{\tanh(ze\phi/4kT)}{\tanh(ze\phi_0/4kT)} = e^{-x/\lambda} \tag{2.2}$$

where ϕ_0 is the potential at $x = 0$ and λ is the characteristic thickness of the double layer and is given by

$$\lambda = \left(\frac{\varepsilon_r\varepsilon_0 kT}{2n(ze)^2}\right)^{1/2} \tag{2.3}$$

Whenever ϕ_0 is sufficiently low, equation (2.2) reduces to an exponential form

$$\phi = \phi_0 \exp(-x/\lambda) \tag{2.4}$$

The Gouy-Chapmann model - though correctly capturing the relation of double layer capacitance with the concentration and ϕ - predicts an unlimited rise in differential capacitance at high ϕ_0. Stern [78] proposed an improved model where in contrast to the Gouy-Chapmann model, ions are not treated as point charges. In this confined Stern model, the double layer capacitance consists of the OHP and the diffuse double layer (Figure 2.2). The total double layer capacitance C_d is thus given by

$$\frac{1}{C_d} = \frac{1}{C_H} + \frac{1}{C_D} \tag{2.5}$$

where C_H is the capacitance arising from the charge in the OHP and C_D the capacitance related to the diffuse layer.

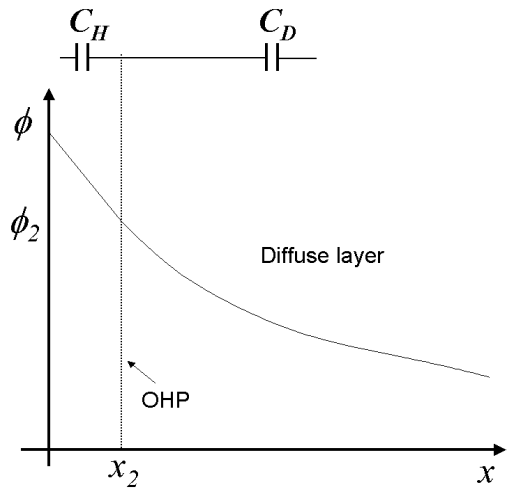

Figure 2.2: Double layer capacitance as a series network of Helmholtz and diffuse layer capacitance (top) and potential profile as a function of the distance from the electrode surface x, for a dilute electrolyte. ϕ_2 is the potential at the outer Helmholtz plane (OHP) situated at x_2.

2.1.2 Electrochemical reaction & reaction rate theory

In the following, the basic principle of an elementary reaction rate theory is presented, which allows an easy understanding of the kinetics of electrochemical reactions. Consider two substances A and B, which undergo the following elementary reactions

$$\mathrm{A} \underset{k_b}{\overset{k_f}{\rightleftarrows}} B \tag{2.6}$$

where k_f and k_b are the forward and reverse rate constants, respectively. Then, the rates of the reactions are given by

$$v_f = k_f C_A \text{ and } v_b = k_b C_B \tag{2.7}$$

where v_f and v_b are the forward and reverse reaction rates, respectively, and C_A and C_B are the concentrations of species A and B. Therefore, the expression for the net reaction rate v_{net}, which is the difference between the forward and the reverse reaction rate, reads

$$v_{net} = k_f C_A - k_b C_B \tag{2.8}$$

At equilibrium, the net reaction rate is zero, that is, the forward and the reverse reaction rates are equal.

Experimentally, it is well established that the rate constant depends exponentially on the temperature:

$$k = Ae^{-E_A/RT} \tag{2.9}$$

where E_A is the activation energy, A the frequency factor or pre-exponential term, R the gas constant, and T the absolute temperature. The pre-exponential factor A and the activation energy E_A can be interpreted as the number of trials attempted on a reaction and the probability for the reaction to occur, respectively. Equation (2.9) can also be interpreted in the framework of the activated complex theory [79]. In this theory, the reactant and the product occupy minima on the potential energy surface (PES), and the reaction coordinate progresses along a complex favoured path on the PES. This energy path contains an energy barrier that has to be crossed, which is called the activation energy. A sketch of a 1D potential energy curve as a function of the reaction coordinate is shown in Figure 2.3. The heights of the energy barriers measured from the energy level of the reactant and product are called activation energy for the forward (E_{AF}) and backward (E_{AB}) reaction, respectively.

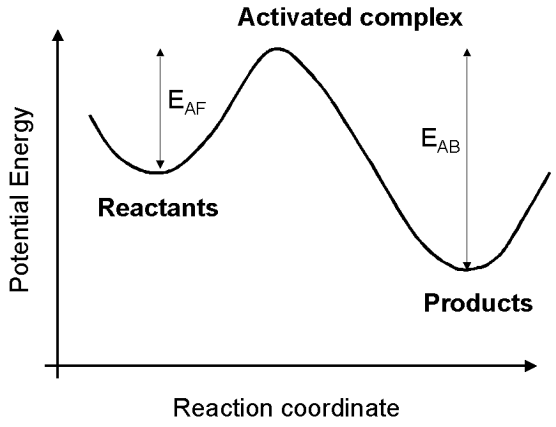

Figure 2.3: Simplified schematic of a reaction path on a one dimensional potential energy surface illustrating the idea of the activated complex.

This idea of the theory of the activated complex is applicable to an electrochemical reaction also. However, the PES becomes a function of the electrode potential [80]. Therefore, the activation energy changes with the applied voltage and the direction and the rate of an electrode reaction can be altered by changing the sign or magnitude of the applied voltage [65]. Consider a simple electron transfer reaction, where n electrons are transferred to an oxidized species O.

$$\mathrm{O} + n\mathrm{e} \rightarrow \mathrm{R} \tag{2.10}$$

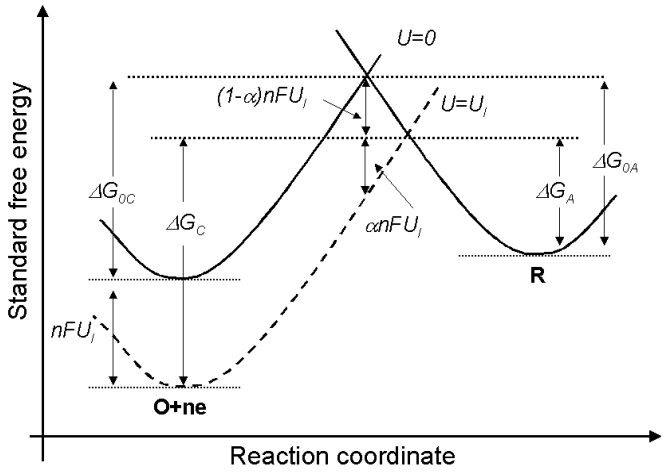

Figure 2.4: Standard free energy diagram for a simple redox reaction (2.10) and $U = 0$ (bold curve) and $U = U_1$ (dashed curve). U is measured with respect to the standard equilibrium electrode potential. The free energy for the activation changes with the applied potential U.

Figure 2.4 shows the standard free energy diagram for the above reaction, where the reduction (or cathodic) and the oxidation (or anodic) standard free energies are ΔG_C and ΔG_A, respectively. ΔG_{0C} and ΔG_{0A} denote the respective standard free energy at electrochemical equilibrium. The solid curves correspond to the standard equilibrium electrode potential, $U = 0$ V (i.e. we measure U vs. the equilibrium potential). By changing the potential by an amount U_1, the energy of an electron on the electrode changes by nFU_1, consequently the solid curve for O+ne shifts by that amount, as shown in Figure 2.4 by the dotted line. In this expression, F is the Faraday constant.

In the presence of an applied potential U_1, the new activation barrier for the oxidation is less than ΔG_{0A} by an amount $(1-\alpha)nFU_1$ and for the reduction it is higher than ΔG_{0C} by an amount αnFU_1. The parameter α, denoted as the transfer coefficient, has a value between one and zero. Hence, the expressions for the new activation barrier for the oxidation ΔG_C and the reduction ΔG_A can be written as

$$\Delta G_A = \Delta G_{0A} - (1-\alpha)nFU_1 \tag{2.11}$$

$$\Delta G_C = \Delta G_{0C} + \alpha nFU_1 . \tag{2.12}$$

Using equation (2.9), the rate constants can be expressed as a function of the applied voltage U

$$k_f = A_f e^{-\Delta G_C / RT} = A_f e^{-\Delta G_{0C} / RT} e^{-\alpha nFU / RT} \tag{2.13}$$

$$k_b = A_b e^{-\Delta G_A / RT} = A_b e^{-\Delta G_{0A} / RT} e^{(1-\alpha) nFU / RT} \tag{2.14}$$

Here A_f and A_b denote the pre-exponential factor of the forward and the backward reaction, respectively. Now, when the interface is at equilibrium, we can write

$$C_O k_f = C_R k_b \tag{2.15}$$

where the concentrations of 'O' and 'R' are denoted as C_O and C_R, respectively. For equal concentrations $C_O = C_R$ it follows

$$k_f = k_b \tag{2.16}$$

or

$$A_f e^{-\Delta G_{0C} / RT} e^{-\alpha nFU_0 / RT} = A_b e^{-\Delta G_{0A} / RT} e^{(1-\alpha) nFU_0 / RT} = k_0 \tag{2.17}$$

The quantity k_0 is known as a standard rate constant. Rewriting the rate constants in terms of the standard rate constant

$$k_f = k_0 e^{-\alpha nF(U-U_0)/RT} \tag{2.18}$$

$$k_b = k_0 e^{(1-\alpha) nF(U-U_0)/RT}, \tag{2.19}$$

the expression for the net current i for an electrode of effective area A is obtained:

$$i = nAFk_0[C_O e^{-\alpha nF(U-U_0)/RT} - C_R e^{(1-\alpha) nF(U-U_0)/RT}] \tag{2.20}$$

2.1.3 Forced convection: The rotating electrode

An electro-catalytic surface reaction involves a convective or diffusive transport of the reactants and the products. If the mass transport rate is comparable to or slower than the rate of the surface reactions, the electrode kinetic is not rate determining, what is under most circumstances undesirable. A slow mass transfer can be enhanced by using a forced convection method. In a forced convection system, either the electrode moves with respect to the solution (rotating or vibrating electrode) or the electrolyte flows over the electrode, e.g., by employing an external pump. The advantages of a controlled convective mass transport method are that

(a) a steady state is attained quickly and high precision measurements are possible;

(b) the rate of the mass transfer to the electrode can be altered by changing a control parameter such as the flow rate or the rotation rate of the electrode; and

(c) known and reproducible mass transfer conditions are easily achievable, which is difficult otherwise.

Among the various forced convection systems, the rotating disk electrode (RDE) is widely used. It is easy to manufacture and for steady state conditions the Navier-Stokes equation can be solved analytically to predict the fluid dynamics near the electrode. Usually an RDE is cylindrical in shape, made of a chemically inert material, such as PTFE, and the working electrode is embedded in that inert material. The electrode is connected to a controlled stepper motor through a metal shaft and a brush contact is used to make the electrical connection. The rotation rate of the motor is a control parameter for the mass transport. The streamlines near the electrode as obtained from the hydrodynamic equation under steady state conditions are shown in Figure 2.5a.

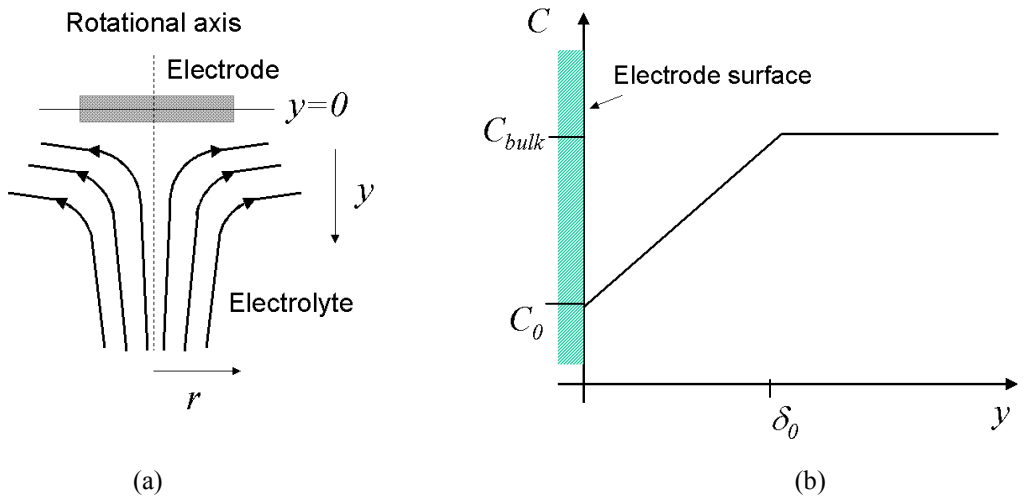

Figure 2.5: (a) Streamlines near a RDE at steady state (b) Concentration profile in front of the electrode according to the linear diffusion layer model.

Knowing the velocity profile, the concentration profile can be calculated from the convective diffusion equation. Again, for steady state conditions the limiting current can be calculated, from which the diffusion layer thickness δ_0 can be extracted. δ_0 corresponds roughly to the distance from the electrode in which mass transport by diffusion takes place, i.e. it is assumed that up to this distance convection can be neglected. Outside of the diffusion layer the electrolyte is well mixed through convection. δ_0 can be adjusted through the rotation rate, and is given by

$$\delta_0 = 1.61 D^{1/3} \omega^{-1/2} \nu^{1/6} \tag{2.21}$$

where D is the diffusion coefficient of the reacting species in the electrolyte, ω the angular frequency of the rotor, and ν the kinematic viscosity of the electrolyte.

The linear diffusion layer model assumes that the concentration is equal to the bulk concentration up to a distance δ_0 and varies linearly between δ_0 and the electrode surface, where the concentration c_0 at the electrode surface adjusts according to the reaction rate and mass transport (Figure 2.5b). Here c_{bulk} is the concentration of the species in the bulk. Assuming further that δ_0 is constant, the temporal change of c_0 can be obtained [81, 82] as illustrated in Figure 2.6 . The dashed line indicates the concentration profile at a time t and the solid line indicates the profile at a time $t+dt$. The shaded area is equal to the difference between the amount of matter that diffuses towards the electrode surface and the amount of matter that reacts at the surface in dt. Hence,

$$\frac{1}{2}\delta_0[c_0(t+dt) - c_0(t)] = \frac{D(c_{bulk} - c_0)}{\delta_0} dt - k_r c_0(t) dt \tag{2.22}$$

Therefore, within the linear diffusion layer approximation the temporal evolution of c_0 is governed by

$$\frac{dc_0}{dt} = \frac{2D(c_{bulk} - c_0)}{\delta_0^2} - \frac{2k_r c_0}{\delta_0} \tag{2.23}$$

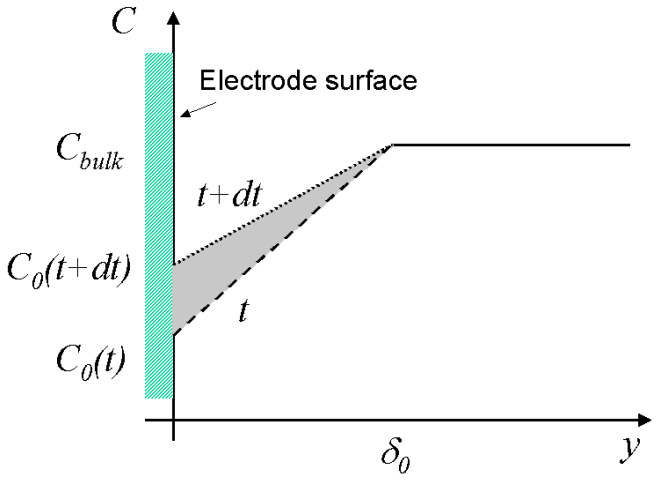

Figure 2.6: Schematic illustrating the temporal changes of c_0 with the linear diffusion layer model for a RDE.

2.2 Nonlinear dynamics

2.2.1 Dynamical system

In this work, we denote by the term dynamical system a continuous system that evolves in time. The state of the system is described by a state vector X whose components are the phase space variables such that

$$X \in \mathbb{R}^n$$

and the evolution law is given by,

$$\dot{X} = f(X, \alpha) \text{ with } \alpha \in \mathbb{R} \tag{2.24}$$

where α is a parameter and the function f is

$$f : \mathbb{R}^n \to \mathbb{R}^n$$

2.2.2 Fixed point of the dynamical system and its stability

The fixed points X^0 of the dynamical system 2.24 are given by

$$\dot{X} = f(X^0, \alpha) = 0 \tag{2.25}$$

The fixed points are also known as equilibrium points of the system. Whether a fixed point X^0 is stable or not depends on the response of the system with respect to a small perturbation. Upon an infinitesimal perturbation, it may return to the fixed point or may evolve away from the fixed point. In the first case, the fixed point is stable; in the second case, it is unstable. The stability of a fixed point can be obtained from a linear stability analysis. Limiting our analysis to a two-dimensional system, (which however can be easily extended to an n-dimensional system), equation (2.24) can be written as

$$\begin{pmatrix} \dot{x}_1 \\ \dot{x}_2 \end{pmatrix} = \begin{pmatrix} f_1(x_1, x_2, \alpha) \\ f_2(x_1, x_2, \alpha) \end{pmatrix}. \tag{2.26}$$

The fixed point $x_1^0,\ x_2^0$ of the system is then determined by the solution of the equation

$$\begin{pmatrix} f_1(x_1^0, x_2^0, \alpha) \\ f_2(x_1^0, x_2^0, \alpha) \end{pmatrix} = \begin{pmatrix} 0 \\ 0 \end{pmatrix}. \tag{2.27}$$

Expanding the function $f(X,\alpha)$ in a Taylor series around x_1^0, x_2^0, the temporal evolution of a small perturbation $\boldsymbol{h} = X\text{-}X^0$ can be expressed as

$$\dot{h}_1 = f_1(x_1^0, x_2^0, \alpha) + \left.\frac{\partial f_1}{\partial x_1}\right|_{X^0} h_1 + \left.\frac{\partial f_1}{\partial x_2}\right|_{X^0} h_2 + .. \textit{ higher order terms} \qquad (2.28)$$

and

$$\dot{h}_2 = f_2(x_1^0, x_2^0, \alpha) + \left.\frac{\partial f_2}{\partial x_1}\right|_{X^0} h_1 + \left.\frac{\partial f_2}{\partial x_2}\right|_{X^0} h_2 + .. \textit{ higher order terms} \qquad (2.29)$$

where the partial derivatives are evaluated at the fixed point.

Neglecting the higher order terms in equations (2.28, 2.29), we can write

$$\begin{pmatrix} \dot{h}_1 \\ \dot{h}_2 \end{pmatrix} = \begin{pmatrix} \frac{\partial f_1}{\partial x_1} & \frac{\partial f_1}{\partial x_2} \\ \frac{\partial f_2}{\partial x_1} & \frac{\partial f_2}{\partial x_2} \end{pmatrix} \begin{pmatrix} h_1 \\ h_2 \end{pmatrix} \qquad (2.30)$$

or

$$\begin{pmatrix} \dot{h}_1 \\ \dot{h}_2 \end{pmatrix} = \boldsymbol{J} \begin{pmatrix} h_1 \\ h_2 \end{pmatrix} \qquad (2.31)$$

where $\boldsymbol{J}$ is the Jacobi matrix. These linear equations admit solutions of the form

$$\boldsymbol{h} = \boldsymbol{v} e^{\mu t} \qquad (2.32)$$

and we arrive at the Eigenvalue problem,

$$\left[\boldsymbol{J} - \mu \boldsymbol{I}\right] \boldsymbol{v} = 0 \qquad (2.33)$$

where $\boldsymbol{I}$ is the identity matrix. For a nontrivial solution, it is necessary that

$$\det(\boldsymbol{J} - \mu \boldsymbol{I}) = 0 \qquad (2.34)$$

The eigenvalues μ_1 and μ_2 determine how the quantity $\boldsymbol{h}$ behaves with time. For example, when at least one of them is positive, $|\boldsymbol{h}|$ increases with time, and the system moves away from the fixed point. Thus, the eigenvalues determine the stability of a fixed point.

Case 1: μ_1, μ_2 is real and $\mu_1 \cdot \mu_2 > 0$. In this situation, both eigenvalues have the same sign. If both μ are negative

$$\lim_{t\to\infty} e^{\mu_i t} = 0$$

Thus, $|\boldsymbol{h}|$ decreases with time and the fixed point is stable. In this case, the fixed point is known as a stable node. If they are both positive

$$\lim_{t\to\infty} e^{\mu_i t} = \infty$$

Thus, $|\boldsymbol{h}|$ increases with time and the fixed point is unstable. The fixed point is known as an unstable node.

Case 2: μ_1 , μ_2 is real and $\mu_1 \cdot \mu_2 < 0$. In this situation, the eigenvalues have opposite signs. The fixed point is unstable and is called a saddle point.

Case 3: μ_1 , μ_2 is complex conjugate with non-zero real part; i.e.

$$\mu_{1,2} = \alpha \pm i\beta \text{ and}$$

$$\boldsymbol{h} = \boldsymbol{v}_1 e^{\alpha t} e^{i\beta t} + \boldsymbol{v}_2 e^{\alpha t} e^{-i\beta t}$$

In this situation, any trajectory close to the fixed point is oscillatory. The fixed point is a stable focus if $\alpha < 0$ and an unstable focus if $\alpha > 0$.

2.2.3 Bifurcation

The word 'bifurcation' means division into two. In a more general context, it is used to indicate a qualitative change of a picture or behaviour under the variation of parameters on which the object being studied depends [55, 83-85]. In the context of dynamical systems, a bifurcation denotes a change in the number or the stability of limit sets. Consider a continuous time dynamical system that depends upon the parameter α :

$$\dot{X} = f(X, \alpha) \quad X \in \mathbb{R}^n \text{ and } \alpha \in \mathbb{R} \tag{2.35}$$

As the parameter α varies, the phase portrait also changes, where a phase portrait is a phase space representation that contains all asymptotic states to which the system tends to as $t \to \pm\infty$. When the phase portrait changes qualitatively under the variation of the parameter, a bifurcation occurs. Therefore, before and after a bifurcation the phase portraits are topologically different or not homeomorphic. In general, two shapes are topologically identical if there is a continuous deformation that converts one shape into the other one. When a bifurcation occurs in a small neighbourhood of an equilibrium or fixed point, it is called a local bifurcation of the equilibrium. There are also bifurcations

that cannot be detected by looking only at a small neighbourhood of an equilibrium; such a bifurcation is called a global bifurcation [86]. It is associated with a global configuration change in phase space. Generally, in a two dimensional system the following bifurcations may occur:

1) a saddle node bifurcation of fixed points
2) a Hopf bifurcation
3) a saddle loop bifurcation
4) a saddle node bifurcation of limit cycles
5) a saddle node bifurcation with infinite period.

The first two kinds are local bifurcations; which implies that they can be detected with a linear stability analysis around a fixed point. The remaining ones are the global bifurcations, and more sophisticated methods are required for their detection.

2.2.4 Saddle node bifurcation

In the case of a saddle node bifurcation, two stationary states, a saddle point and a node merge at the bifurcation point. This degenerate saddle-node pair disappears when the parameter is changed in one direction and two fixed points separate when the parameter changes in the other direction. Thus, in a saddle node bifurcation, a pair of fixed points is created or destroyed. A saddle node bifurcation occurs when one eigenvalue of the Jacobi matrix $\boldsymbol{J}$ becomes zero, which implies that the determinant of the linear eigenvalue problem is zero.

Consider the dynamical system

$$\frac{dx}{dt} = \alpha - x^2 . \tag{2.36}$$

For $\alpha < 0$, it has no fixed points, and for $\alpha > 0$ it has two fixed points at $\pm\sqrt{\alpha}$, one of which is stable and the other one unstable. The bifurcation occurs at $\alpha = 0$. Therefore, depending on the direction of change of α, two fixed points are created or annihilated (Figure 2.7).

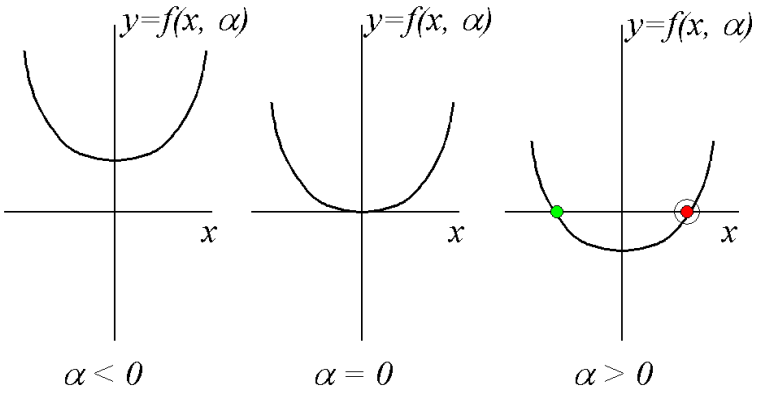

Figure 2.7: A simple example of a saddle node bifurcation. The green and red dot indicates a stable and an unstable fixed point, respectively.

2.2.5 Hopf bifurcation

In a Hopf bifurcation a limit cycle is born or destroyed. The Hopf bifurcation can be conveniently detected in a linear stability analysis of fixed points [55, 87, 88]. It occurs when the eigenvalues of a linearized system become purely imaginary: $\mu_{1,2} = \pm i\beta$ and

$$\frac{d\,\mathrm{Re}\,\mu(\alpha_0)}{d\alpha} \neq 0 \tag{2.37}$$

where α is the parameter value at which $\mathrm{Re}\,\mu(\alpha_0) = 0$. At $\alpha = \alpha_0$ the fixed point changes its stability and the Hopf theorem guarantees that a limit cycle is born with zero amplitude and a period

$$T_0 = \frac{2\pi}{\beta} \tag{2.38}$$

There are two types of Hopf bifurcations, so-called supercritical and subcritical Hopf bifurcations, which are shown in Figure 2.8. In a supercritical Hopf bifurcation, the limit cycle is stable and exists at parameter values at which the fixed point is unstable. In case of a subcritical bifurcation, the limit cycle is unstable and coexists with the stable equilibrium point.

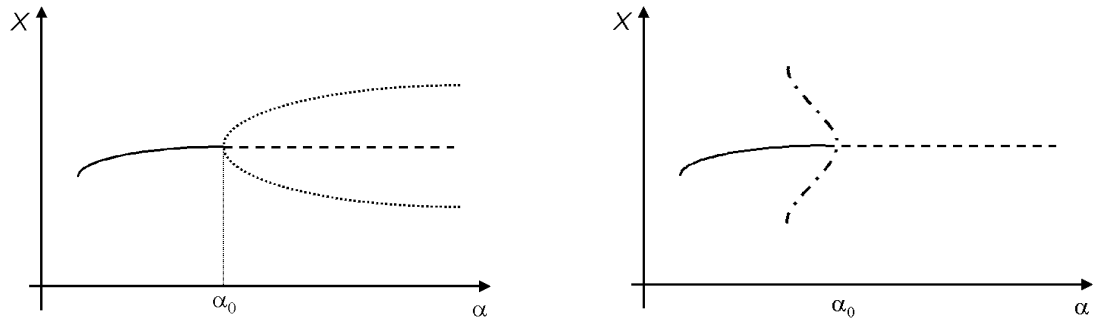

(a) (b)

Figure 2.8: Supercritical (a) and subcritical (b) Hopf bifurcation Solid line: stable fixed point dashed line: unstable fixed point. Dotted line: maxima and minima of the stable limit cycle; dot dashed line: maxima and minima of the unstable limit cycle.

2.2.6 Reaction diffusion system

In the previous section, we have described a dynamical system, whose temporal evolution is governed by a finite number of ordinary differential equations (ODEs). When the dynamical system is a spatially distributed system, it is described by partial differential equations, and the dynamical system is thus infinite dimensional. The evolution of a spatially distributed chemical system is usually modelled by a system of reaction diffusion equations:

$$\frac{\partial \overline{u}}{\partial t} = \boldsymbol{D}\nabla^2 \overline{u} + \overline{f}(\overline{u}). \tag{2.39}$$

In spatially one dimensional systems that we consider below the Laplace operator reads

$$\nabla^2 u_1 = \frac{\partial^2 u_1}{\partial x^2} \tag{2.40}$$

The components of the vector $\overline{u}$ contain the dependent variables u_i, x is the spatial coordinate, and $\boldsymbol{D}$ the diffusion coefficient matrix. The first term of eq. (2.39) describes diffusion of the species, and the second term specifies their homogeneous dynamics. The interaction between reaction and diffusion in systems exhibiting e.g. bistability or oscillations lead to pattern formation [53, 55-59].

2.3 Nonlinear dynamics of the electrochemical interface

2.3.1 Bistability in an electrochemical system

A bistable system can exist in two different stable states for identical experimental conditions. These stable states can be fixed points, limit cycles, or limit cycles with fixed point etc [52, 89]. They are stable under sufficiently small perturbations, but a stronger perturbation may cause a transition between the states. One component is sufficient to exhibit bistability. A positive feedback is a necessary condition for bistability to occur.

A large number of electrochemical systems exhibits bistability under certain condition. Consider $i_F(\phi_{DL})$-relations with either an N-shaped or an S-shaped characteristic, as shown in Figure 2.9, where $i_F(\phi_{DL})$ is the Faradaic reaction current and ϕ_{DL} is the double layer potential. In the following sections, we discuss how bistable behaviour arises in these so called N-NDR and S-NDR systems, respectively.

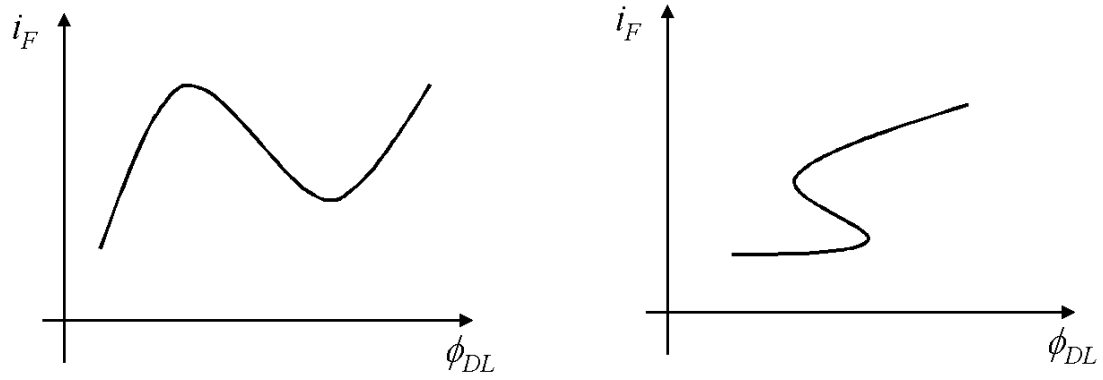

Figure 2.9: (a) N- and (b) S-NDR current vs. electrode potential characteristics for an electrochemical system.

2.3.1.1 Bistability and N-NDR systems

The dynamics of an electrified interface is illustrated easiest with a simple equivalent circuit of the electrode|electrolyte interface, which is shown in Figure 2.10

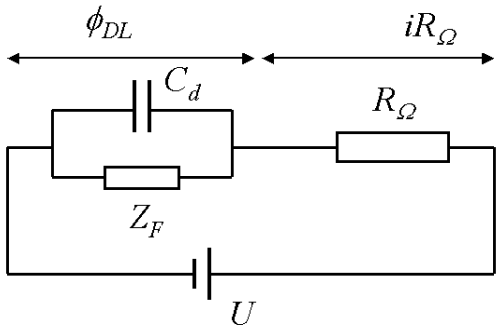

Figure 2.10: Equivalent circuit of an electrochemical interface. C_d: double layer capacitance ($C_d = CA$ where C: specific double layer capacitance; A: electrode area;) Z_F: Faradaic impedance; R_Ω: ohmic (electrolyte) resistance; ϕ_{DL}: double layer potential; U: external or applied voltage; i: current.

The charge balance of this equivalent circuit leads to the following differential equation, where $i_F(\phi_{DL})$ is the Faradaic reaction current and A the surface area of electrode.

$$CA\frac{d\phi_{DL}}{dt} + i_F(\phi_{DL}) = \frac{U - \phi_{DL}}{R_\Omega} \tag{2.41}$$

An N-NDR system exhibits bistabililty when a fixed point lies in the negative differential resistance region of the current voltage curve and the ohmic resistance of the circuit is larger than the absolute value of the Faradaic impedance of the reaction. The steady states of this system can be found graphically by plotting the current potential relation at the interface and the load line, given by the expression on the rhs in Eq. 2.41, in one graph, as shown in Figure 2.11a. The intersections of both curves are steady states of the system. In a certain voltage and series resistance range, three fixed points are found.

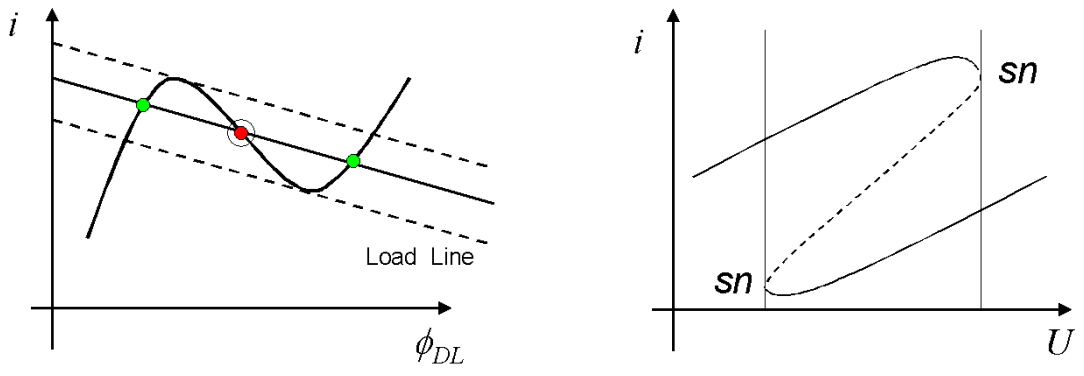

(a) (b)

Figure 2.11: (a) Load lines and N-NDR current vs. electrode potential characteristic. (b) Bistable region in a current vs. external voltage plot. The dashed load lines in (a) are for values of U at which the *sn* bifurcations occur.

The two outer fixed points are stable and the middle one is unstable. Figure 2.11b shows the bistable region in a *U-i* plot. The origin of the bistability can be easily seen when one assumes that the system is operated galvanostatically, i.e. the current is kept constant. Consider a fixed point on the middle (unstable) branch of the i_F-ϕ_{DL} characteristic. If ϕ_{DL} increases slightly due to a perturbation, the current decreases and consequently ϕ_{DL} increases further. This increase of ϕ_{DL} continues until the system reaches the outer branch of the N. The argumentation is exactly the same in case of the potentiostatic mode if the ohmic series resistance is sufficiently large. Thus, the parameters U and R_Ω determine the bistable region.

2.3.1.2 Bistability and S-NDR systems

The stationary current voltage curve of an S-NDR system shows a bistability in the i_F - ϕ_{DL} curve in a potentiostatic experiment with a vanishing ohmic resistance. The existence of the bistability in the i_F-ϕ_{DL} characteristic, where ϕ_{DL} takes on the role of a parameter, indicates the presence of an autocatalytic chemical variable, on which the current depends. Thus, in an S-NDR system the dynamic equations contain a chemical autocatalytic loop [61, 90]. Electrochemical systems belonging to the class of S-NDR systems are complementary in most dynamic properties to N-NDR systems. S-shaped current-potential characteristics may arise in systems with a potential-dependent surface phase transitions between a disordered (dilute) and an ordered (condensed) adsorption state [91] or due to attractive interactions among the adsorbed molecules. They are characterized by

(a) an S-shaped current potential characteristic of the interface. As discussed before, this characteristic exhibits bistability;

the unstable branch or the middle, sandwiched branch is unstable and cannot be detected in a potentiostatic experiment; and

(b) the current voltage characteristic becomes single-valued if an ohmic series resistance is present in the system and exceeds a critical value.

2.3.2 Oscillations and electrochemical systems

From a more physical point of view, oscillations often emerge owing to the interaction of a positive and a negative feedback loop between two variables of the system. The positive feedback loop acts destabilizing, the negative one stabilizing [49, 57].

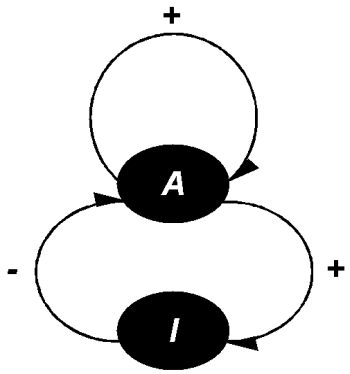

Figure 2.12: Interaction of activator (*A*) and inhibitor (*I*) variables that lead to oscillations.

The interaction of the two feedback loops is illustrated in Figure 2.12. Here, *A* denotes the species or variable that is associated with the destabilizing process and is often referred as activator. *I* stands for the inhibitor, indicating that this variable inhibits the further growth of *A*. The arrows indicate the interactions between the species: *A* acts autocatalytic for its own production and activates the production of *I*, while *I* inhibits the growth of *A*. Such a feedback scheme leads to oscillations if the activator changes on a faster time-scale than the inhibitor. Here we explain electrochemical oscillators with the help of the activator inhibitor picture.

2.3.2.1 Oscillations and N-NDR systems

As we have discussed in the previous section, N-NDR systems show bistability, which arises from a positive feedback loop. Therefore, whenever there is at least one additional slow process that introduces a negative feedback loop into an N-NDR system may exhibit sustained oscillations. In some electrochemical systems, the N-NDR region is masked by another parallel electro-chemical process and the NDR region is not seen in the current potential curve. Such kind of systems are denoted as hidden N-NDR systems (HN-NDR) [50, 92-94]. In N-NDR and HN-NDR oscillators [50, 92-94] the mechanistic features of the negative feedback are different. In non-hidden N-NDR systems, one of the known sources of negative feedback is the mass transport limitation of the reactive

species, which is governed by equation (2.21). The negative feedback is easily seen: If ϕ_{DL} increases, the current decreases and, thus, the consumption of the reactive species is reduced and the mass transfer replenishes its concentration in front of the electrode. However, as the concentration in the vicinity of the electrode increases, the current increases, which prompts a decrease in ϕ_{DL}.

In HN-NDR systems, the most common mechanism, which masks the N-NDR behaviour, is the adsorption of a species, which inhibits the main Faradaic reactions. If the isotherm of the poisoning species is such that its coverage decreases with the increasing ϕ_{DL} around the N-NDR region, it introduces a negative feedback into the system. Thus, the system again possesses a stabilizing and destabilizing loop that causes oscillations: An initial increase in ϕ_{DL} leads to a decrease in current because of the N-NDR characteristics. This is because the coverage reacts upon a change in ϕ_{DL} much more slowly than the electron transfer process.

Under an external control, i.s. under potentiostatic control and a sufficiently high series resistance or under galvanostatic control, the decrease in current prompts a further increase of ϕ_{DL} and establishes a positive feedback loop. Again, increasing ϕ_{DL} causes a decrease in the coverage of the poisoning species, which in turn leads to an increase in current since more surface becomes available for the current carrying reaction, which establishes the negative feedback loop. Therefore, the system can oscillate under both potentiostatic and galvanostatic control, which is the essential difference to an N-NDR system, which only oscillates under potentiostatic condition and moderate electrolyte (ohmic) resistance.

2.3.2.2 Oscillations and S-NDR systems

As already said, an S-NDR system has a chemical autocatalysis and the electrode potential may behave as a negative feedback variable. Thus, also in an S-NDR system the feedback loops, necessary for the oscillations, are present. Figure 2.13 shows the relative locations of saddle node and Hopf bifurcations in the U/R_Ω parameter plane for an S-NDR system [51], which are universal. The bistable region is largest for zero ohmic resistance, and narrows for increasing values of R_Ω and U. At large values of R_Ω and U oscillatory behaviour exists in a region opposite to the bistable region. However, oscillations arise only if the destabilizing process is faster than the stabilizing process. In

other words, the typical time scale on which the autocatalytic species changes has to be faster than the double layer charging.

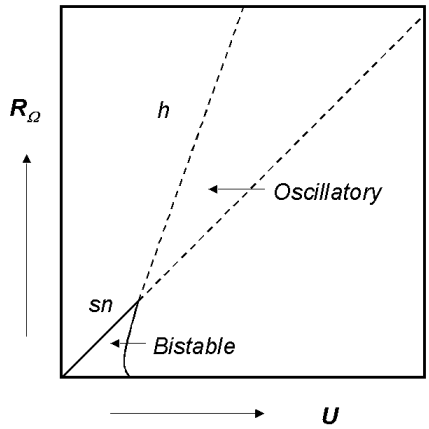

Figure 2.13: Region of saddle node and Hopf bifurcation in an S-NDR system.

This is possible only for the extremely fast reactions or adsorption steps, or large values of the double layer capacitance, which makes oscillations in any S-NDR system very unlikely, and in fact, up to now there is no S-NDR system known, which exhibits oscillations.

2.3.3 Pattern formation in electrochemical systems

So far, we have assumed that there are no spatial variations parallel to the electrode, i.e., the electrode potential and all chemical concentrations or coverages are uniform along the electrode surface. However, the interaction of the reaction dynamics and spatial transport processes might also induce pattern formation, like it is known of reaction diffusion systems. However, in electrochemical systems the dominant spatial coupling was shown not to be diffusion of chemical species, but so-called migration coupling mediated by the electrostatic potential. The corresponding reaction migration equation results from a local charge balance and reads [50]

$$C\frac{\partial \phi_{DL}}{\partial t} = -i_F - \sigma \left.\frac{\partial \phi}{\partial z}\right|_{z=WE} \tag{2.42}$$

Here, σ is the conductivity of the electrolyte, ϕ the electrostatic potential in the electrolyte. i_F denotes the Faradaic current density and z is the spatial direction perpendicular to the electrolyte, the positive direction pointing into the electrolyte. z =

WE is at the working electrode. Thus, the last term of Eq. (2.42) is the local migration current density entering the interface.

Since the electrolyte is an electroneutral medium, the potential distribution outside the double layer obeys to a very good approximation Laplace's equation. Hence, $\phi(x.y.z)$ can be calculated when appropriate boundary conditions to Laplace's equation are specified. The knowledge of the potential distribution, in turn, allows the local migration current density at the interface to be calculated.

The migration coupling was shown to be nonlocal, i.e., a change of the electrostatic potential at a specific position $(x_0, y_0)_{z=WE}$ at the interface changes the migration current density not only in the direct neighborhood of $(x_0, y_0)_{z=WE}$ but in an entire neighboring range [50, 51]. Physically, the nonlocal coupling results from the tendency of the electrolyte to stay electroneutral: A change of the electrostatic potential at a position at the interface (in mathematical terms of a boundary condition to Laplace's equation) leads to a simultaneous adjustment of the potential distribution in the entire electrolyte, and thus also of the electric field at the interface. The coupling range depends on the distance between the working electrode and the counter electrode. Thus, it depends on the geometry of the electrochemical cell.

Depending on the experimental operation mode and the cell design, besides migration coupling, all positions of the electrode might also be globally coupled. As defined in [51] "A global coupling exists if a local change of a variable is felt by all the other locations with the same strength independent of their distance to the locations of the local variations." In an electrochemical experiment, there are two sources of global coupling. First, any external series resistance leads to a global coupling under constant outer voltage conditions. This can be seen easily: Assume that there is a local fluctuation of the current density at the electrode, which changes the total current slightly. Then, also the voltage drop across the Ohmic resistance in series to the cell changes. The outer applied voltage is equal to the sum of the voltage drop across the external resistor and the electrochemical cell. Hence, when the voltage drop across the resistor changes, the voltage drop between any location of the WE and the RE also has to change. Realizing that constant current conditions, or the galvanostatic operation mode, can be seen as the limit of the potentiostatic operation mode with a resistor in series to the cell and the outer

voltage as well as the series resistance approaching infinity, it is obvious that a global coupling exists also under galvanostatic conditions.
Finally, it could be shown that whenever the RE is postioned between the WE and the CE, a (weighted) global feedback is introduced [51]. For the case of a ring WE and the RE positioned on the axis of the ring, we are again dealing with a global coupling in the strict sense.

In summary, at the electrode|electrolyte interface the interaction between the uniform dynamics of the electrochemical system and migration coupling mediated by the electrostatic potential in the electrolyte or global coupling introduced through the external control of the system might lead to the spontaneous formation of potential and/or concentration patterns.

2.4 CO electrooxidation on Pt

CO electrooxidation proceeds through the reaction of adsorbed CO and an oxygenated surface species, most likely OH. In the following, the surface electrochemical processes of the different reaction steps are shortly summarized.

2.4.1 Adsorption of CO on Pt

In a heterogeneously catalysed reaction, at least one of the reactants has to adsorb on the catalyst surface before the reaction takes place. This is true for a heterogeneous gas phase reaction as well as an electro-catalytic reaction. Thus, the study of adsorption is fundamental for the understanding of electro-catalytic reactions [95]. Two types of adsorption processes have to be distinguished: physisorption and chemisorption. Physisorption is the weakest form of adsorption, in which the main attraction is caused by van der Waals forces. The equilibrium positions of the atoms result from the balance between Pauli repulsion and van der Waals attraction. In chemisorption, a significant hybridization between the adsorbate and the substrate electronic state occurs and a chemical bond is created. The concept of the highest occupied molecular orbital (HOMO) and the lowest un-occupied molecular orbital (LUMO) are conveniently used to explain the formation of chemical bonds. However, in case of a solid surface, energy bands instead of discrete energy levels have to be considered. In case of a solid without a

band gap, the HOMO and LUMO can be considered as an electronic state at the Fermi level. In Refs. [95-97] the importance of the local density of states at the Fermi surface for chemisorption is discussed.

The first step of CO electrooxidation on platinum surfaces is the adsorption of CO. The adsorption of a CO molecule on a metallic surface was studied by Blyholder [98] using the Hückel theory. Blyholder proposed that only the 5σ (HOMO) and the 2π (LUMO) orbital of a CO molecule play a role for the bonding to the metal surface. On adsorption, charge transfer occurs from the bonding 5σ orbital towards the metal, and charge back transfer from the metal towards the antibonding 2π orbital. Because of this interaction, the completely filled 5σ orbital of the free CO molecule becomes partially emptied (donation of electron to the metal), and the originally empty 2π orbital becomes partially filled (back donation of electron to the CO molecule). The CO remains neutral after the adsorption [99] because of the exchange of the charge (Figure 2.14).

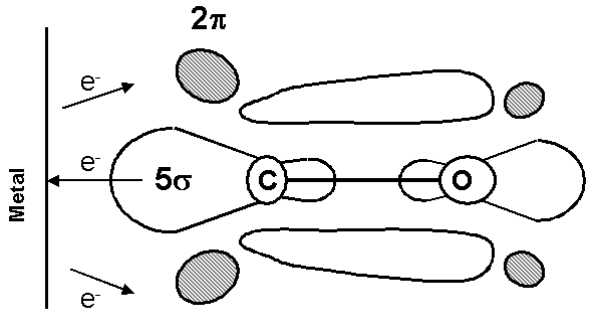

Figure 2.14: Molecular orbital picture of adsorbed CO on a metal surface [99].

Furthermore, it is found that a CO molecule adsorbs perpendicularly to the surface with the C end down [100]. The net effect of donation and back donation is a lowering of the CO bond, which manifests itself in a lower vibrational frequency of the CO molecule compared to the CO molecule in the gas phase. The strength of this effect depends on the adsorption site, and the vibrational frequencies of the adsorbed CO molecule can be used to distinguish different adsorption sites. For example, the overlap between the metal band and the 2π orbital is stronger at a hollow position than an on top position. Consequently, the vibrational frequency at a hollow position is lower than at an on top position. The same considerations hold for CO adsorption at a metal|aqueous electrolyte interface.

2.4.2 Adsorbed oxygenated species

CO electrooxidation on Pt takes place through the reaction of adsorbed CO with OH or other oxygenated species on the surface. In the following a brief introduction in the adsorption of OH on Pt is given [101-104]. The CV of a polycrystalline Pt electrode is shown in Figure 2.15. The peaks in the potential range between 0 mV and 250 mV are related to underpotential adsorption and desorption of hydrogen. Adjacent at positive potentials is the so called double layer region between 270 mV and 800 mV, in which only a capacitive current flows. The onset of Pt electrooxidation starts around 820 mV during the positive sweep. A broad electrooxidation wave with two or three little humps are observed beyond the onset of oxidation. On the reverse sweep a single peak arises from the oxide desorption, which is shifted towards more negative potential with increasing positive turning potential. This shift of the desorption peak is an evidence of the irreversibility of the oxide formation process.

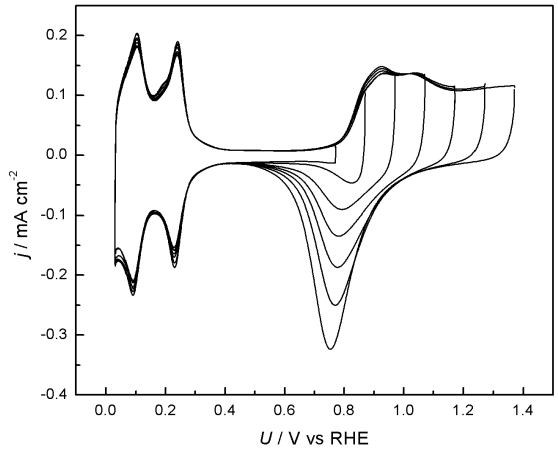

Figure 2.15: Cyclic voltammogram (CV) of a rotating polycrystalline platinum disk electrode in 0.5 M H_2SO_4 for different positive turning potentials; scan rate: 100 mV/s; rotation rate: 1200 rpm.

The details of OH adsorption and oxide formation are quite complicated and are in part discussed controversially. However most authors agree with the picture discussed by Conway [101] and illustrated in Figure 2.16. In Figure 2.16, blue circles represent platinum atoms, yellow circles OH molecules, and dashed circles oxygen atoms.

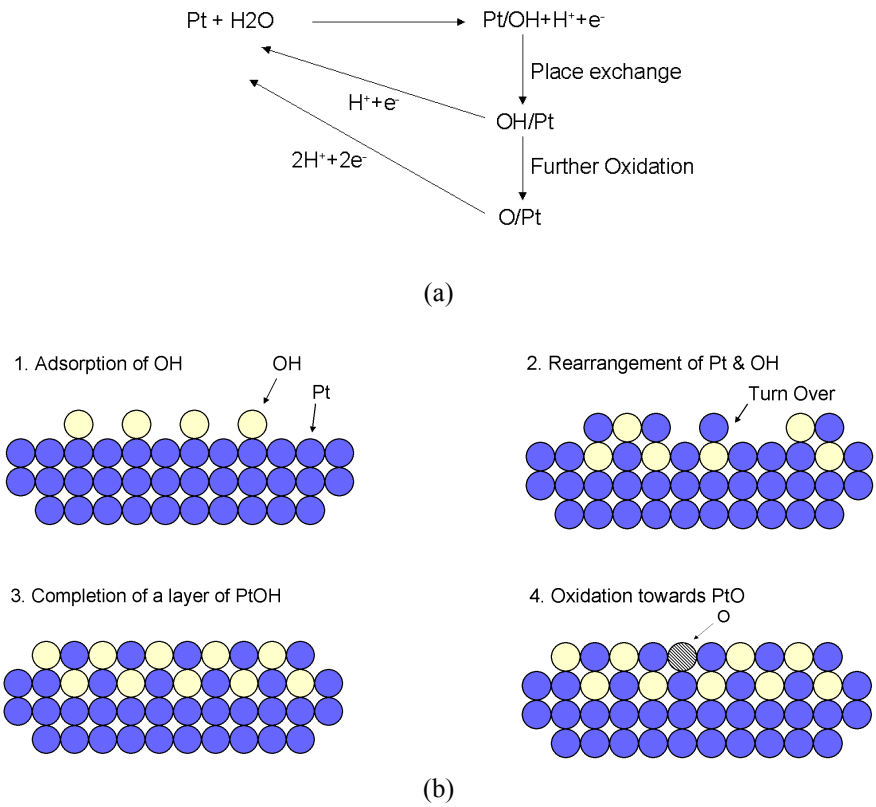

Figure 2.16: Oxide formation mechanism and place exchange process; Figure (a) shows the reaction steps. Figure (b) shows atomistic description of the process, where blue circles denote platinum atoms, yellow circles adsorbed OH species, and gray circles oxygen atoms.

In the first electrooxidation step (left upper image) adsorbed OH molecules are formed until half a monolayer is completed. Further electrooxidation occurs through a place exchange process between OH and Pt atoms leading to a formation of 3D PtOH layer (second and third pictures in Figure 2.16). The subsequent electrooxidation of OH within the 3D layer yields PtO.

An alternative electrooxidation mechanism was proposed by Birss et al. [105] on the basis of electrochemical quartz-crystal microbalance (EQCM) experiments. Birss et al. observed that the anodic mass-response profile in the 850 mV–1400 mV (vs RHE) potential region involves a continuous mass increase, which contradicts the above discussed mechanism. A two-electron mechanism of Pt surface electrooxidation that excluded OH as an intermediate state was proposed instead. This picture was supported by Harrington [106] based on his simulation of ac voltammetry recorded over the region of Pt oxide-film formation, and is also supported by Jerkiewicz group [43, 107, 108].

Besides these studies based on methods from electrochemical surface science, Siegmeier [109] compared the calculated bifurcation structure that two models describing the

oxidation of H_2-CO mixtures on Pt yield with experiments. One model assumes the formation of OH as the first step in Pt electrooxidation and the other one the direct two-electron oxidation to oxide. In case of the ´OH- model´, he obtained a nearly qualitative agreement while in case of the oxide model the discrepancy between simulations and experiments remained huge. Based on these recent results and the large body of literature that presents support of the ´OH -model´, we also base our discussion in this work on this more common model.

Finally, we mention that the onset potential of surface electrooxidation is also very sensitive to the electrolyte concentration and the presence of further anions in the electrolyte. The effect of the presence of halides on the OH formation was first mentioned by Breiter [110] and later investigated thoroughly by other groups [111-113]. This issue will be discussed in detail in the fifth chapter.

2.4.3 Surface reaction mechanism

In general, a surface reaction occurs through either the Langmuir-Hinshelwood (LH) mechanism or the Eley-Rideal (ER) mechanism [114, 115]. Consider the reaction between two species A and B to the product A-B. If the reaction proceeds through the LH mechanism, first both the reactants adsorb on the surface, then they react to form the product A-B on the surface, which finally desorbs from the surface. In the ER mechanism one of the reactants, which we assume to be A, adsorbs on the surface and reacts with the non-adsorbed reactant B to form the product A-B, which then again desorbs from the surface. The LH and ER mechanisms are illustrated in Figure 2.17a and Figure 2.17b, respectively.

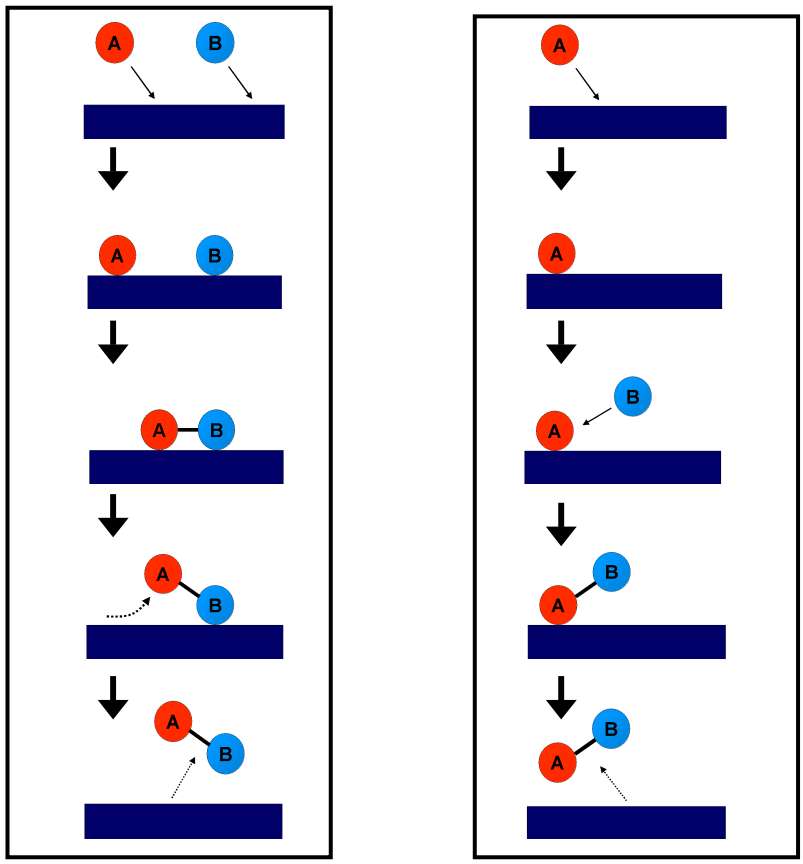

Figure 2.17: Surface reaction mechanisms (a) Langmuir Hinshelwood mechanism (b) Eley Rideal mechanism; 'A' and 'B ' are the reactants; The dark rectangle represents the surface.

In an elementary chemical reaction between two species in a diluted solution, the bulk reaction rate is proportional to the product of the concentrations of the two species. Applying this idea to the LH mechanism, the reaction rate will be proportional to the product of the coverages of the two species. However, this is an assumption, which arises from the mean field (MF) approximation [116], originally introduced by Bragg and Williams [117, 118]. Thus, considering a reaction with reacting species A and B, we can write

$$M+A \rightleftharpoons A_{ad} \tag{2.43}$$

$$M+B \rightleftharpoons B_{ad} \tag{2.44}$$

$$A_{ad}+B_{ad} \rightleftharpoons A\text{-}B+2M \tag{2.45}$$

Here M denotes an adsorption site. The expression for the reaction rate is

$$r_{AB} = k_r \theta_A \theta_B \tag{2.46}$$

The quantities θ_A, θ_B, and k_r are the coverages of the two reactants A and B, and the reaction rate constant, respectively. (In case of an electrochemical reaction, k_r is potential dependent). In MF theory, one of the basic assumptions is that the adsorbed species are uniformly distributed over the surface as a two-dimensional lattice gas. It neglects spatial correlations (the correlation between distributions of molecules on the surface) and fluctuations among the reactants [119]. However, often the spatial distribution of the reactants cannot be neglected in the calculation of the surface reaction rate [120, 121]. For example, if one species forms an island, and the reaction takes place only on the circumference of the island, (preferential reactivity at the perimeter of the adsorbate islands) [122], the reaction rate will not be proportional to the product of the coverages of the reactants.

2.4.4 The electrooxidation of CO

As already mentioned, the electrooxidation of CO proceeds through the Langmuir Hinshelwood mechanism. Furthermore, it can be shown that the Langmuir–Hinshelwood mechanism leads to an instability in the current-voltage characteristic if the adsorption rate of one of the products comes into the transport limited region [123]. Cyclic voltammograms during CO electrooxidation on a Pt electrode thus exhibit a bistable region, as can be seen in Figure 2.18. Starting at low potential, the current remains close to zero up to about 850 mV vs. RHE and the electrode is covered by CO. At 850 mV sufficient OH can adsorb to react off the monolayer of CO, which manifests itself in a sharp ignition peak. For potentials positive to the ignition peak the electrooxidation current remains high and potential independent, i.e. the reaction rate is determined by mass transfer. On the reverse scan towards lower potentials, the reaction remains high beyond the firing potential, resulting in a hysteresis. Thus, the underlying stationary current potential curve is S-shaped, and the bistable region is enclosed by two saddle node bifurcations.

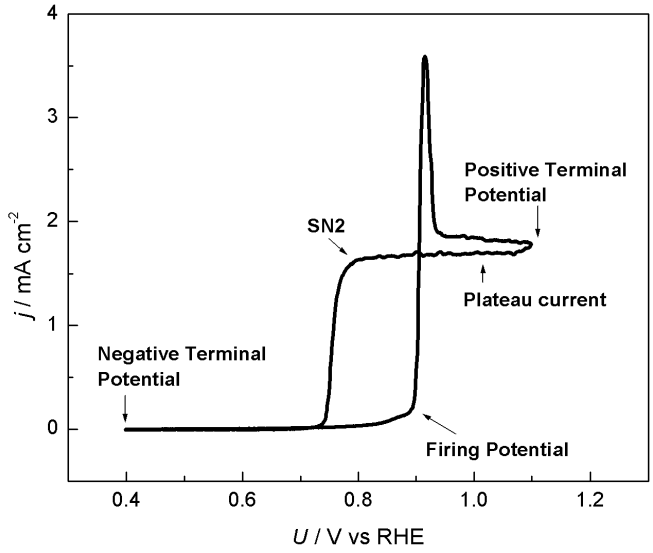

Figure 2.18: Cyclic voltammogram of a rotating polycrystalline Pt electrode in CO saturated 0.1 M $HClO_4$ solution. Scan rate: 50 mV/s; rotation rate 1200 rpm;

The SN2-point in Figure 2.18 marks the saddle node bifurcation point at lower potential while the saddle node bifurcation at the high potential is denoted as ´firing potential´. Koper et al. [45] discussed a simple model for the electrochemical CO electrooxidation that reproduces the S-shaped curve under potentiostatic control. However, oscillatory behaviour also found in the experiments is not predicted in their model. The model takes into account the following reaction steps:

(a) A finite mass transport rate of CO from the bulk to the electrode surface.

$$CO_{bulk} \leftrightarrow CO_s \tag{2.47}$$

(b) Competitive adsorption of CO and OH.

$$CO_s + M \rightarrow CO_{ad} \tag{2.48}$$

$$H_2O + M \rightarrow OH_{ad} + H^+ + e^- \tag{2.49}$$

(c) Reaction between adsorbed species.

$$CO_{ad} + OH_{ad} \rightarrow CO_2 + H^+ + e^- + 2M \tag{2.50}$$

Here 'M' denotes an active site on the surface. These reaction steps can be translated to a mathematical model that consists of a system of ordinary differential equations for the coverages of the surface with CO and OH, respectively, and the concentration of CO in front of the electrode. This simple model already reproduces the bistable behaviour including the observed trend upon changes of parameters such as the mass transfer rate

of CO. As outlined in [51], a reaction mechanism giving rise to bistability must have a positive or autocatalytic feedback loop. In our case, the feedback loop is produced by the Langmuir Hinshelwood mechanism together with slow transport of CO: Consider a CO covered state close to the firing potential. Assume that owing to a fluctuation there is a critical number of free surface sites onto which CO and OH will adsorb. Adsorbed OH however, which has initially still a low coverage, will react with adsorbed CO, recovering two free surface sites per reaction and leading to a finite reaction current. The latter, however will decrease the concentration of CO in front of the electrode somewhat, and as a consequence, the rate of OH formation relative to the adsorption rate of CO increases. This, in turn, will lead to a higher reaction rate that causes the concentration of CO in front of the electrode to decrease further; Hence, the fact that CO adsorption becomes diffusion controlled while OH adsorption is always reaction controlled constitutes a positive feedback and causes the primary instability. An analogous consideration holds close to the SN2 point. Starting point for the investigation of this thesis is thus an understanding of this primary instability during CO bulk electrooxidation.

Chapter 3: Experimental methods

In this chapter, the description of the experimental instruments, procedures, methods, and the specifications of chemicals and gases is presented. A detailed description of the electrode preparation for both, polycrystalline and single crystal Pt electrodes is given with the results of the pre-treatment of single crystals in a rotating disk electrode system.

3.1 Electrochemical cell

The electrochemical cell, with which all experiments of this work were performed, is illustrated in Figure 3.1. The cylindrically shaped cell was made of glass. Two gas inlet tubes were attached to the main cell opposite of each other to allow for nearly symmetrical gas flow. A glass cylinder 'B' was used to prevent gas bubbles from attaching at the working electrode surface.

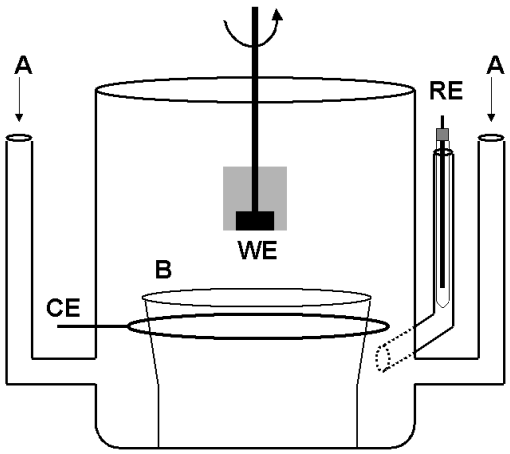

Figure 3.1: A schematic of the electrochemical cell. WE: working electrode; CE: counter electrode; RE: reference electrode; A: gas inlet tube; B: glass cylinder to prevent gas bubbles to attach at the working electrode surface.

Experiments were carried out with a three-electrode arrangement, which allows to study the current flow as a function of the potential of the working electrode (WE) only. This is achieved by measuring the potential with respect to a reference electrode (RE), which carries hardly any current but senses only the potential. Thus, the potential of the RE is independent of the cell current and reproducible and stable under the operating conditions. The current flows through the counter electrode (CE), whose potential is adjusted in such a way that either the potential difference between the WE and the RE or the current through the cell is equal to a preset value. The junction between the RE compartment and the main cell was located below the CE to exclude a global coupling through the external circuit [51]. In most cases, the potential drop between the WE and the RE was minimized by working with a concentrated base electrolyte (0.5 M H_2SO_4 or 0.5 M $HClO_4$). For 0.5 M H_2SO_4 the cell resistance was 14 Ω. Throughout this work, the RE was a saturated $Hg|Hg_2SO_4$ electrode, which was kept in a separate compartment. All the potentials in the experiments were measured against this electrode. However, in all figures the potentials are given with respect to the reversible hydrogen electrode (RHE), which was determined using the RE potential and the pH of the solution according to

$$U_{\mathrm{RHE}} = U_{\mathrm{Hg|Hg_2SO_4}} + 0.640 + 0.058\,\mathrm{pH}$$

The CE was a 1 mm thick Pt wire bent to a ring of 65 mm in diameter. It was located parallel and at a distance of 45 mm to the WE to ensure a symmetrical current flow between WE and CE.

Polycrystalline platinum (99.999%) and single crystal platinum disk electrodes were used in the experiments. The polycrystalline disk electrode was embedded in a solid PTFE cylinder and the single crystal disk electrodes were assembled in a PTFE holder before an experiment. The exposed geometrical surface area of the polycrystalline and the single crystal electrodes were 0.197 cm^2 and 0.102 cm^2, respectively.

3.2 Instrumentation

The electronic device, which controls the current through the electrochemical cell is called potentiostat. The potentiostat measures the potential difference between the WE and the RE, and pumps current through the CE (either direction) such that the potential difference between the WE and the RE remains constant at some predefined value. The user could adjust the predefined potential difference and may control the experiment in

different ways. Many times a linear ramp voltage, which cycles periodically between two limits (the lower and upper voltage) is used. This experiment is called cyclic voltammetry, and the current voltage curve of a full cycle is called a cyclic-voltammogram (CV). The experimentalist sets the lower and upper voltage with a predefined slope (scan rate). Usually a potentiostat can also be operated as a galvanostat. In this operation mode, the current is set to some predefined value and the electrode potential is adjusted in such a way that the current can be maintained. The Electronic Laboratory of the Fritz-Haber-Institute der MPG, Berlin, built the potentiostat that was employed in all experimental studies reported here. A Sun Solaris based Real Time system was used for the data acquisition. The rotating electrode system consisted of a variable speed rotator with a controller from Pine Research Instrumentation.

3.3 Chemicals and electrolyte solution

The purity of the used chemicals is an important issue in electrochemical experiments. Contaminations present in the electrolyte may adsorb on the electrode surface and influence the surface processes either by taking part in the reactions or by blocking active sites. Therefore, all the chemicals used in this work were of high purity grade unless otherwise specified (concentrated $HClO_4$ (Suprapure Merck), H_2SO_4 (Suprapure Merck), and HBF_4 (Aldrich `Purum'). For the same reason, ultra pure water was used in the experiments (Millipore MilliQ). The water had 18.2 MΩ cm specific resistance and less than 4 ppb TOC (total organic carbon). The purity levels of the gases used were 99.999% (Ar, Linde) and 99.997% (CO, Air liquid), respectively. Various mixtures of Ar and CO were generated using computer operated mass flow controllers. Special care has been taken during the assembling of the gas pipe and the valve to prevent contaminations.

3.4 Cleaning procedure and electrode preparation

All glasswares used in the experiments were intensively cleaned. The standard procedure consisted of boiling all glassware in concentrated pro analysis grade nitric acid for one to four days, depending on the level of contamination. In case of a high contamination level the glassware was further treated with an $H_2O_2 + H_2SO_4$ mixture (1:2) for three to seven days, and after this treatment the glassware was first rinsed with water and then

immersed in water for one to two days before starting an experiment. Normally, this intensive cleaning procedure was applied once a month or, when the base CV indicated the presence of contaminations in the system. Otherwise, the glassware was rinsed with water for five times before and after the experiment. Between experiments, it was kept in or filled up with water. All PTFE parts of the system were cleaned in an ultrasonic bath, alternately with concentrated sulphuric acid and concentrated sodium hydroxide solution for five minutes each. This procedure was repeated three times. Finally the PTFE parts were cleaned three times in water for five minutes each.

3.4.1 Polycrystalline Pt electrode

The pre-treatment of the polycrystalline electrode was a two-step procedure. First, the electrode was polished with diamond pastes from 10 to 1 micron particle size. When switching to another polishing paste and at the end of the polishing procedure the electrode was cleaned consecutively with acetone, ethanol, and methanol in an ultrasonic bath each time for five minutes. Immediately before every experiment, the electrode was kept in an ultrasonic bath of a mixture of concentrated sulphuric acid and hydrogen peroxide mixture (1:1) for one to five minutes, and thereafter in water for five minutes, three times in a row with new water each time.

3.4.2 Single crystalline Pt electrode

Experiments with platinum single crystals in a rotating electrode system are rare owing to the sensitive nature of the single crystal surfaces. The problem arises from the pre-treatment of the crystal. During the pretreatment of the crystal, temperature can rise up to 1200 K impeding a permanent fixation of the electrode in the rotating electrode holder. On the other hand, a separately pretreated crystal is exposed to air during the assembling process, and a long exposure to air modifies the pretreated surface. In this work, a special electrode holder was designed that allowed for a fast assembly of the electrode in the holder. In this work, Pt(110), Pt(111), and Pt(100) single crystal (MaTek) disk electrodes were used. A platinum wire was spot-welded on the backside of the disks in the form of a little handle in such a way that it could be manipulated with a Pt hook that was attached to a glass rod. The single crystal was flame-annealed to light red glow using a butane burner. The propane flame was applied to the backside of the single crystal, so that the surface of interest did not come into a direct contact with the flame. During the heating,

the crystal colour was monitored in the absence of daylight for easier judgment of the crystal colour and thus crystal temperature. The hot crystal was immediately transferred to a glass vessel filled with a mixture of hydrogen and argon. A schematic of the glass chamber is shown in Figure 3.2.

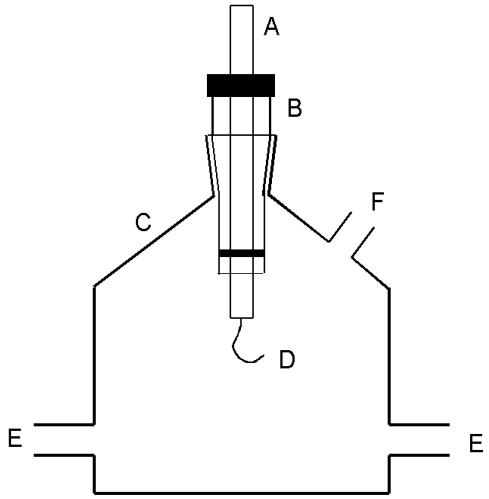

Figure 3.2: Glass vessel used for cooling the single crystal after flame annealing; A: glass rod with attached Pt hook (D); B: glass tube holder for the glass rod A; C: glass vessel; E: inlet for gases; F: outlet for gas.

The crystal was allowed to cool down in an H_2+Ar flow (1:1) for about 5 minutes, before CO was added to the gas mixture for another five minutes. Then, the H_2 and Ar flow was switched off and only a CO flow was maintained for three more minutes. After this procedure, the crystal had adapted to room temperature again and was covered by CO. It was quickly transferred to the PTFE electrode holder, which is depicted in Figure 3.3.

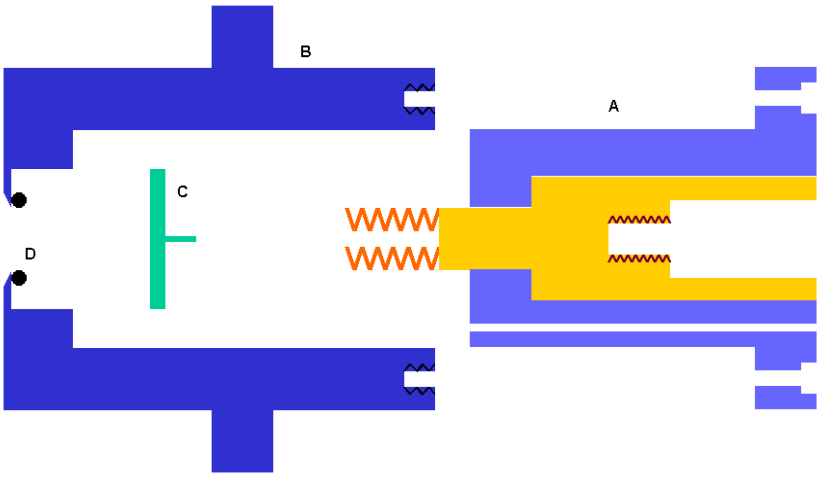

Figure 3.3: Holder for single crystal electrode that could be attached to a rotator. A: inner part of the PTFE holder with electric contact and thread for attachment to the rotating shaft, B: outer part of the PTFE holder, C: single crystal, D: O-ring.

The crystal was inserted in the outer part of the PTFE holder (B), then the inner PTFE part (A) was attached, and a drop of water was added to the crystal surface. Finally, the assembled electrode was mounted on the shaft of the rotator and inserted into the electrochemical cell at a voltage of 40 mV (RHE). Before the transfer, the electrolyte was purged with Ar. The pretreatment was repeated when the CV did not show the fingerprint of the respective single crystal.

A thorough study of different pretreatment procedures and their effect on the surface quality was carried out by Kolb et al. [124]. The influence of flame annealing on the surface state was also discussed in [14, 18, 21, 32, 45, 64, 125-131]. It was found that cooling in air produces rough and defect rich surfaces due to the presence of oxygen [124, 132-134]. Therefore, a reducing atmosphere was maintained while cooling the crystal by employing a mixture of H_2 or CO with Ar. Using CO has the additional advantage that it adsorbs strongly and thus protects the surface against contaminations [124]. When cooling a Pt(100) electrode in a H_2+Ar mixture or in CO gas leads to an unreconstructed surface [124]. In case of Pt(110), the (1×2)→(1×1) phase transition occurs at 810°C. Therefore the (1×1) structure is obtained when the crystal is cooled down rapidly. On the other hand, slow cooling results in the (1×2) structure [14]. In both cases, an H_2+Ar mixture was used. It is known from UHV studies of Pt(110) that adsorbed CO lifts the (1×2) reconstruction. Therefore, it is expected that in our case the pretreatment leads to a (1×1) surface.

3.4.3 Base CV of rotating Pt(110), Pt(100), and Pt(111) in 0.5 M H_2SO_4

Below stationary cyclic voltammograms of the three low-indexed Pt single crystal electrodes are presented to document that the developed rotating electrode system for the single crystals worked satisfactorily. Figures 3.4a, 3.4b, and 3.4c show stationary CVs of the rotating Pt(110), Pt(100), and Pt(111) electrodes in 0.5 M H_2SO_4, respectively. In all cases, the upper turning voltage was deliberately kept negative to the oxide formation region to avoid any surface oxidation. These CVs show the characteristic features of the respective single crystal surfaces. They were stable for more than one hour.

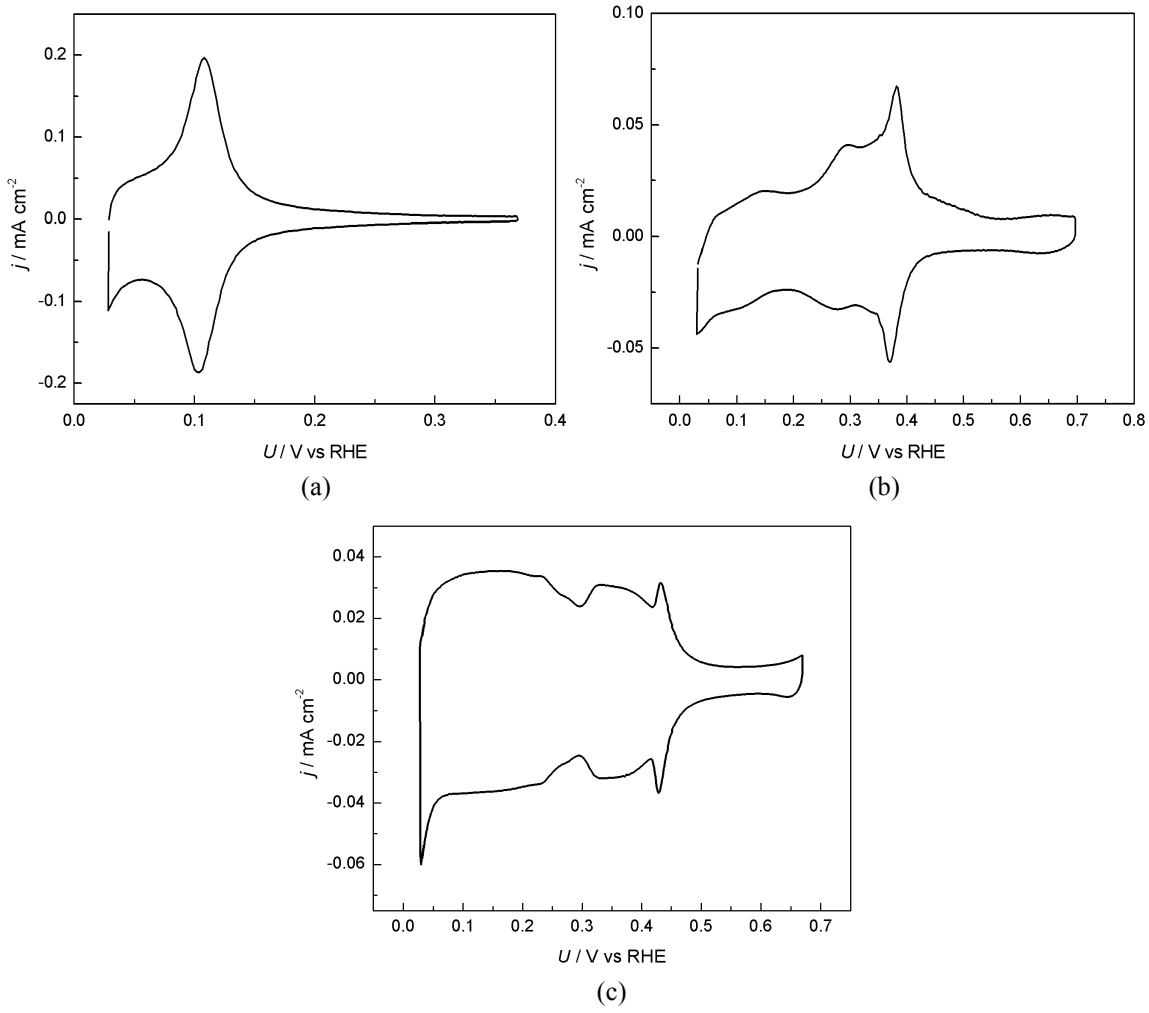

Figure 3.4: Stationary base CVs of the rotating single crystal (a) Pt(110) in 0.5 M H_2SO_4 (b) Pt(100) in 0.1 M H_2SO_4 (c) Pt(111) in 0.5 M H_2SO_4; rotation rate: 1200 rpm; scan rate: 100 mV/s.

In the CV of Pt(110), a single peak is observed, which arises from the under potential deposition (upd) of hydrogen. The CV of Pt(100) exhibits a shoulder at about 270 mV and a more pronounced current peak at about 375 mV. According to Markovic and Ross

[3], these features correspond to the coupled processes of adsorption of upd hydrogen and desorption of anions from (100)×(111) step defects (shoulder) and from (100) terrace sites, respectively. The CV of Pt(111) is comparatively complex. Owing to the higher work function of Pt(111) compared to Pt(110) and (100) and thus its higher pzc, anion adsorption occurs more positive and is separated from the hydrogen upd ad- resp. desorption region [3]. The first current plateau up to approx. 300 mV is thus related to upd hydrogen ad- or desorption, the current between 300 and 500 mV to anion (here HSO_4^-) ad- and desorption, whre the sharp 'butterfly peak' at the positive and of the region stems from a surface phase transition of the adsorbed bisulphate adlayer [135, 136]. The sharpness of these peaks is an indication for the state of the surface. A well prepared surface forms well-ordered adsorbate layers because it has only a small number of defects, consequently ad- and desorption peaks are sharp. On the other hand, the adlayers are not well ordered in the presence of numerous defects, and the peaks become flat and broad. The appearance of the characteristic fingerprints of the low index surfaces confirms that the rotating electrode system is working well. However, the peaks were not as sharp as found with a single crystal electrode in the hanging meniscus geometry [132]. We attribute this somewhat lower surface quality to two facts. First, although kept to a minimum the CO protected electrode surface was exposed to air during the assembly process, which led to a minor surface degradation. Second, it was found that the sharpness of the peaks decreases during the first few CVs when the rotation was switched on. Therefore even trace contaminations in the electrolyte, which we could not get rid of despite of extreme cleaning and the use of suprapure chemicals, also led to some degradation of the surface.

Chapter 4: Application of Derivative Control during Bulk CO Electrooxidation

4.1 Introduction

The dynamic behaviour of a system can be controlled by applying a small perturbation to a control parameter. In a pioneering work, Ott, Grebogi, and Yorke [137] presented a theoretical guideline for controlling chaos by stabilizing an unstable periodic orbit. Shortly after this prediction chaos control was successfully realized in experiments by Peng et al. [138], Rollins et al. [139], Ditto et al. [140], Hunt [141], and others [142-144]. Subsequently, Pyragas [145] proposed an alternative method for controlling unstable periodic orbits using time-delayed feedback [146], which is easier to implement under most experimental conditions. Ross et al. [147, 148] proposed a control strategy to stabilize the saddle fixed point of a bistable system. The proportional integral derivative control and other nonlinear control strategies are frequently used to manipulate the stability of a stationary state [147, 149-155]. Application of the control strategy in electrochemical systems is a subject of extensive research today. Among various works, Parmananda et al. [154] proposed a derivative controller to stabilize an unstable fixed point in an electrochemical system. In this work, we use a derivative control method to change the time scale of some variable in an electrochemical system, thereby destabilizing the stationary state and inducing oscillations.

In electrochemical systems, the double-layer capacitance C_d sets the inherent time scale for the variation of the potential drop across the double-layer. The double layer capacitance is an intrinsic property of the electrode|electrolyte interface and this cannot be varied by varying external parameters. As already discussed in chapter 2, the interfacial kinetics of many electrochemical systems lead to a current voltage curve that possesses a region with a negative differential resistance (NDR), which is either N-type

or S-type. In N-NDR systems, the double layer potential takes the role of the activator, whereas in S-NDR systems the double layer potential acts as an inhibitory variable. Typically, the ratio of the time scales of the double layer dynamics and of the dynamics of chemical species are much larger than one, and as a consequence, N-NDR systems oscillate while S-NDR systems do not exhibit limit cycle behaviour. Kiss et al. [156] point out that it is possible to vary the effective double layer capacitance by employing a recursive derivative feedback control. Consequently, the double layer capacitance becomes a controllable parameter. This opens the possibility to destroy oscillations in N-NDR systems and to induce oscillations in S-NDR systems by increasing the effective double layer capacitance.

Bulk CO electrooxidation on Pt was claimed to belong to the class of S-NDR systems [45]. This hypothesis can be tested and further insight into the dynamics of CO electrooxidation obtained with recursive derivative control. In the following an analogue device, which was designed in the framework of this thesis, is described that implements the recursive feedback control and thus allows the time scale of the double layer dynamics to be varied. Subsequently, experimental results obtained with the CO/Pt system are presented and compared to theoretical predictions.

4.2 Theoretical background

Derivative control denotes a control strategy in which the temporal changes of variables and possibly also of parameters are fed back to the system. Since at a stationary state neither any variables nor any external control parameters change with time, derivative control does not alter steady states of a system. The stability of a stationary state of a dynamical system is determined by the eigenvalues of the Jacobian matrix evaluated at the fixed point, and in contrast to the stationary state the eigenvalues change when derivative control is employed. Therefore, derivative control may alter the stability of a fixed point. Consider a system with n variables and m parameters described by a set of ordinary differential equations:

$$\frac{dX}{dt} = F(X,P) \quad \text{where } X \in \mathbb{R}^n \text{ and } P \in \mathbb{R}^m \tag{4.1}$$

Let us define the derivative control signals, which are applied to the system state variables X and parameters P as $\tilde{X}$ and $\tilde{P}$. $\tilde{X}$ and $\tilde{P}$ be such that the new system can be written as

$$\frac{dX}{dt} = F(X + \tilde{X}, P + \tilde{P}) \tag{4.2}$$

where $\tilde{X}$ and $\tilde{P}$ are

$$\tilde{X} = \left[\tilde{x}_1, \tilde{x}_2, \ldots \quad \tilde{x}_n \right] \tag{4.3}$$

$$\tilde{P} = \left[\tilde{p}_1, \tilde{p}_2, \ldots \quad \tilde{p}_m \right] \tag{4.4}$$

and

$$\tilde{x}_r = \sum_{k=1}^{i1} \alpha_{1rk} \frac{dx_k}{dt} + \sum_{k=1}^{j1} \alpha_{2rk} \frac{dp_k}{dt} \tag{4.5}$$

$$\tilde{p}_r = \sum_{k=1}^{i2} \alpha_{3rk} \frac{dx_k}{dt} + \sum_{k=1}^{j2} \alpha_{4rk} \frac{dp_k}{dt} \tag{4.6}$$

Here *i1, i2, j1,* and *j2* are determined by the number of state variables and parameters used for the control. The gain factors α_{1rk}, α_{2rk}, α_{3rk}, and α_{4rk} determine the control strategy. Note that in a practical system the state variables and parameters may not be always accessible. In case of derivative control, at the steady state the contributions of $\tilde{X}$ and $\tilde{P}$ are zero, therefore equations (4.2) and (4.1) have identical fixed points.

When applying the control strategy, the characteristic time scale of a variable can be increased or decreased by modifying the gain factors in the feedback loop. Let us start with the sth component of equation (4.2).

$$\frac{dx_s}{dt} = f_s(X + \tilde{X}, P + \tilde{P}) \tag{4.7}$$

where the function f_s be such that it can be expressed as

$$f_s(X + \tilde{X}, P + \tilde{P}) = f_s(X, P) + \eta \frac{dx_s}{dt} \tag{4.8}$$

Substituting equation (4.8) in (4.7) we can write

$$(1-\eta)\frac{dx_s}{dt} = f_s(X,P) \tag{4.9}$$

Therefore, by controlling 'η' the characteristic time of x_s can be adjusted. If η is negative, the characteristic time increases, and if η is positive, it decreases. The magnitude and the sign of η are determined by the gain factors in the feedback loop.

The mathematical trick, as shown in the above discussion, is now applied to the electrode|electrolyte interface. In electrochemical systems, the double-layer capacitance sets the time scale for the temporal variation of the potential drop across the double layer ϕ_{DL}, which follows from the charge balance equation (4.10) of the equivalent circuit of an electrochemical cell:

$$CA\frac{d\phi_{DL}}{dt} = -i_F(\phi_{DL}) + \frac{U-\phi_{DL}}{R_\Omega} \tag{4.10}$$

where i_F is the Faradaic current, U is the applied voltage, A is the surface area of the electrode, C is the specific double-layer capacitance, and R_Ω is the cell resistance. In a typical potentiostatic experiment, U is controlled externally and the current i is measured:

$$i = \frac{U-\phi_{DL}}{R_\Omega} \tag{4.11}$$

We choose the control signal to be

$$\alpha\frac{dU}{dt} - \alpha\beta\frac{di}{dt} \tag{4.12}$$

and add it to the applied base voltage U_0

$$U = U_0 + \alpha\frac{dU}{dt} - \alpha\beta\frac{di}{dt} \tag{4.13}$$

The derivative of i with respect to time can be written as

$$\frac{di}{dt} = \frac{1}{R_\Omega}\left(\frac{dU}{dt} - \frac{d\phi_{DL}}{dt}\right) \tag{4.14}$$

substituting equation (4.14) and (4.13) in equation (4.10), one obtains

$$CA\frac{d\phi_{DL}}{dt} = -i_F(\phi_{DL}) + \frac{U_0-\phi_{DL}}{R_\Omega} + \frac{dU}{dt}\left(\frac{\alpha}{R_\Omega} - \frac{\alpha\beta}{R_\Omega^2}\right) - \frac{\alpha\beta}{R_\Omega^2}\frac{d\phi_{DL}}{dt} \tag{4.15}$$

and after simplification

$$(CA+\frac{\alpha\beta}{R_\Omega^2})\frac{d\phi_{DL}}{dt}=-i_F(\phi_{DL})+\frac{U_0-\phi_{DL}}{R_\Omega}+\frac{dU}{dt}(\frac{\alpha}{R_\Omega}-\frac{\alpha\beta}{R_\Omega^2}) \tag{4.16}$$

If we set

$$\beta = R_\Omega$$

equation (4.16) becomes

$$(CA+\frac{\alpha}{R_\Omega})\frac{d\phi_{DL}}{dt}=-i_F(\phi_{DL})+\frac{U_0-\phi_{DL}}{R_\Omega} \tag{4.17}$$

$$(CA+C')\frac{d\phi_{DL}}{dt}=-i_F(\phi_{DL})+\frac{U_0-\phi_{DL}}{R_\Omega} \quad \text{with} \quad C'=\frac{\alpha}{R_\Omega} \tag{4.18}$$

It is evident from the above equation that the parameter α, which can be chosen externally, alters the characteristic time of the double layer potential. In other words, we can alter the effective double layer capacitance of the electrode|electrolyte interface, which is otherwise beyond experimental control. The usual double layer capacitance is of the order of several ten μF/cm^2.

4.3 Experiments

4.3.1 Realization of the control strategy

At first, we describe the implementation of the control strategy, which is depicted schematically in Figure 4.1. Clearly, two differentiators, variable gain amplifiers, and adders are required. The network to the right consists of two impedances and a capacitance and represents the electrochemical cell.

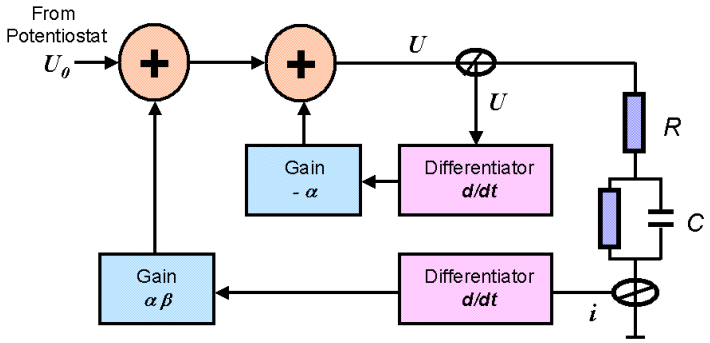

Figure 4.1: Block diagram of the implemented control strategy.

An analogue differentiator circuit as shown in Figure 4.2 generates a continuous time feedback signal proportional to the time derivative of current and voltage. The current and voltage signal could be directly taken from the output of the potentiostat and the output of the control device was fed back to an internal adder of the potentiostat used in the experiments.

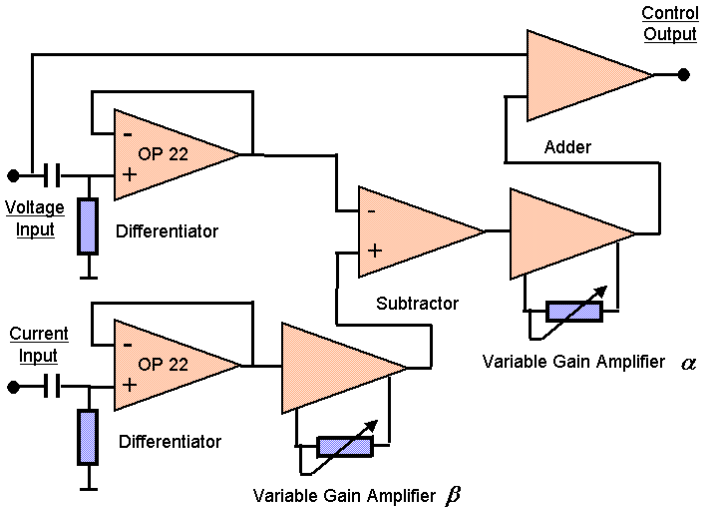

Figure 4.2: Implementation of the control strategy.

The signal was differentiated using a RC differentiator whose output for an input y is

$$RC\frac{dy}{dt} \tag{4.19}$$

The selected capacitor and resistance values were 0.47 µF and 470 Ω, respectively. Note that our potentiostat current output is a voltage signal proportional to the current. Therefore, a voltage differentiator was used for the current input. Because of this conversion, the gain parameter β is not only dependent on the gain of the amplifier behind the differentiator, but also on the conversion factor of the current to voltage converter of the potentiostat.

4.3.2 Experimental procedure

The WE was a polycrystalline platinum disk, and all measurements were carried out in a 0.5 M H_2SO_4 electrolyte. The pre-treatment of the electrode is described in chapter 3, section 3.4.1. The controller was interfaced with the potentiostat through a shielded cable. As a high concentration of strong acidic electrolyte was used during the

experiments, the ohmic contribution from the solution was small. Therefore, an external variable resistance in series with the WE was used to introduce a resistance of 1 kΩ. The electrode rotation rate during all experiments was 1200 rpm.

4.4 Experimental results

Figure 4.3a shows the CV of bulk CO electrooxidation on a rotating polycrystalline platinum electrode in 0.5 M H_2SO_4. The CV exhibits a hysteresis, which is supposed to stem from a bistability present in the system's dynamics. Since under these conditions the cell resistance is negligible, the underlying curve of stationary states is S-shaped and saddle node bifurcations occur at U_1 = 867 mV and U_2 = 905 mV.

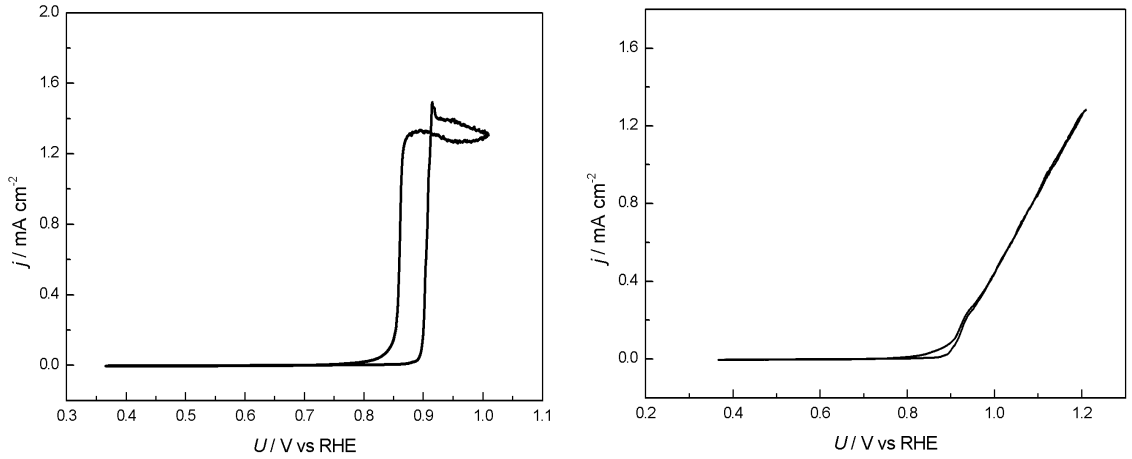

Figure 4.3: CV of a rotating polycrystalline Pt electrode in CO saturated 0.5 M H_2SO_4; rotation rate: 1200 rpm; scan rate: 5 mV/s; (a) without external series resistance (b) with 1 kΩ external series resistance.

When inserting an external series resistance, the S was unfolded and the originally unstable, sandwiched branch was stabilized. This can be seen in the CV shown in Figure 4.3b, which was obtained after a resistance of 1 kΩ was connected in series to the WE. However, on this branch the reaction kinetics still involves a positive feedback loop. According to the theory of S-NDR systems, the stabilization of the branch is due to the fast dynamics of the electrode potential, which acts in a way to suppress the self-enhancing effect of the kinetics. Hence, if this is true, lowering the characteristic time of the double layer potential by means of our control device should result in limit cycle oscillations. As can be seen in Figure 4.4, this is exactly what was observed. For

approximately the first 45 s shown, the control device was connected and the system exhibited regular oscillations. At the time marked by the arrow, the controller was disconnected and the oscillations disappeared. Figure 4.4b shows a magnification of the current time series with oscillations.

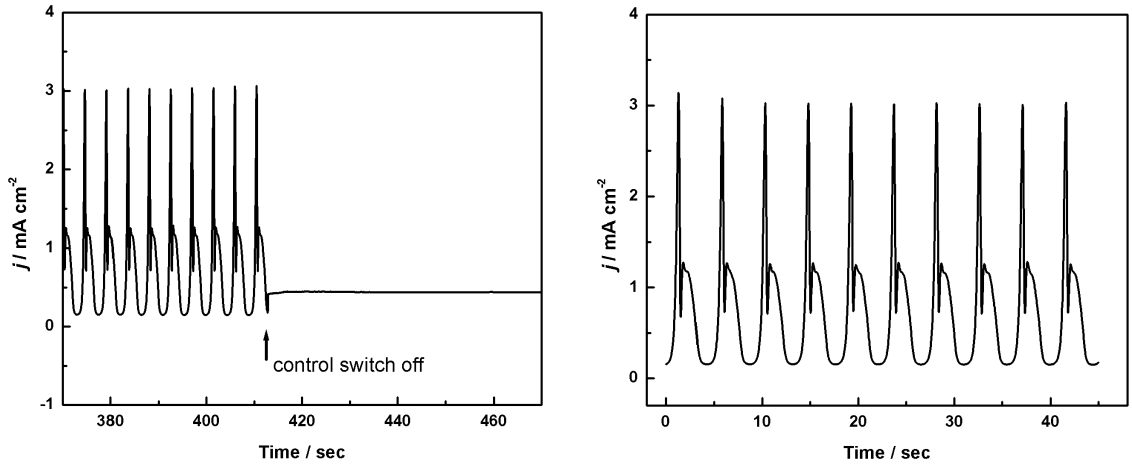

Figure 4.4: (a) Current time series with the control device connected and disconnected. The arrow indicates the time at which the device was disconnected. $\alpha = 4$; $\beta = 1000$; $C_d = 4$ mF, $U =$ 980 mV; (b) Magnification of the current time series with controller connected $\alpha = 4$; $\beta = 1000$; $C_d = 4$ mF, $U = 980$ mV; electrolyte: CO saturated 0.5 M H_2SO_4; rotation rate: 1200 rpm; external series resistance: 1 kΩ.

The oscillations exhibit an overshoot of the current, i.e. a very sharp CO electrooxidation peak, followed by an undershoot. Often, a sharp overshoot of the current is also observed during cyclic voltammetrie (see e.g. Figure 4.5), where it has been attributed to the autocatalytic electrooxidation of a monolayer of CO adsorbed on the surface.

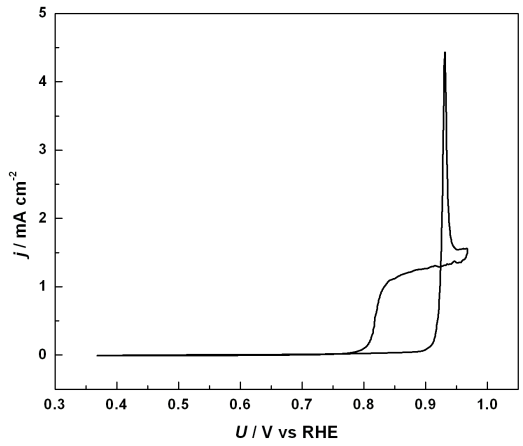

Figure 4.5: CV of a rotating polycrystalline Pt electrode in CO saturated 0.5 M H_2SO_4; rotation rate: 1200 rpm; scan rate: 50 mV/s.

The resemblance of the overshooting behavior in the two types of experiments suggests that the sharp electrooxidation peak within an oscillatory cycle is not an artefact of the electronic control unit but an intrinsic property of the system's dynamics. However, cyclic voltammograms never exhibited an undershooting, or an oscillatory approach to the diffusion limited plateau.

Thus, these features in the time series might arise from the electronic circuit of the feedback device. It contains a reactive element (capacitor) in the feedback path, which makes the gain of the system frequency dependent. Besides, the available operational amplifiers have a finite bandwidth. In a non-ideal operational amplifier a frequency dependent phase shift is introduced in the signal and the gain becomes frequency dependent in a certain parameter region. These non-ideal features of an operational amplifier in combination with the reactive feedback make the system unstable at high frequencies. Therefore, the fast oxidation of the CO monolayer might cause damped oscillations of the device which manifest themselves in the fast oscillations seen in the current time series. Hence, the oscillatory response that follows the first 'overshooting' in the oscillations in Figure 4.4 is likely to be a consequence of the electronic system rather than a property of the system's intrinsic dynamics. Further experiments were carried out with various values of α in order to obtain the minimum capacitance values that still yield oscillatory behaviour. An approximate experimental two-parameter bifurcation diagram as a function of the effective capacitance and the applied voltage U_0 is shown in Figure 4.6. In the region above the parabola, the system was oscillatory. The critical capacitance below which no oscillations could be introduced was found to be 2.3 mF. The range of oscillations was limited to the applied voltage region between 930 mV and 1090 mV, and it was within the range that corresponds to the sandwiched (potentially unstable) branch of the i-ϕ_{DL} characteristics as obtained from the CV shown in Figure 4.3a and indicated by the dashed lines in Figure 4.6.

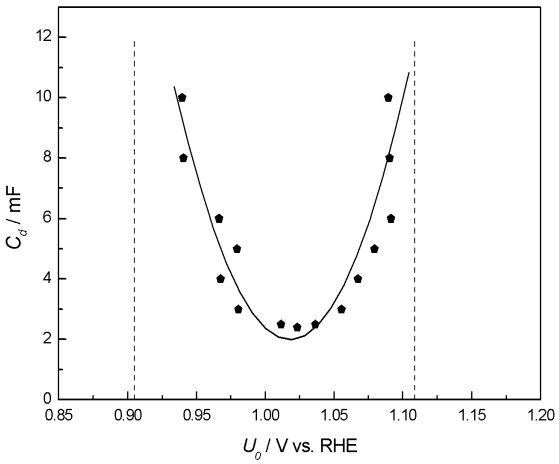

Figure 4.6: Experimentally determined existence region of the oscillations in the capacitance applied voltage parameter plane. Oscillations were found above the parabola-shaped line. The two vertical dashed lines indicate the voltage region, which corresponds to a value of ϕ_{DL} on the unstable (autocatalytic) branch.

In summary, the experimental results show that oscillations can be initiated during the CO electrooxidation on Pt by increasing the effective double layer capacitance. This provides further evidence that the reaction kinetics possesses a positive feedback loop and the system belongs indeed to the class of S-NDR systems. In the next section, simulations are described and compared with the experiments discussed here.

4.5 Modelling and simulation

The simulations were carried out with a model for CO electrooxidation on platinum that was proposed by Koper et al. [45]. The model is similar to the one suggested by Strasser et al. [157] and is based on three simple reaction steps:

$$CO_s + M \rightarrow CO_{ad} \tag{4.20}$$

$$H_2O + M \rightarrow OH_{ad} + H^+ + e^- \tag{4.21}$$

$$CO_{ad} + OH_{ad} \rightarrow CO_2 + H^+ + e^- + 2M \tag{4.22}$$

and takes the transport of CO from the bulk electrolyte to the electrode surface into account, which can formally be written as

$$CO_b \rightarrow CO_s$$

The rates of CO adsorption, OH_{ad} formation and desorption and reaction of CO and OH can be approximated by

$$\nu_{CO,a} = k_{CO,a} c_S (0.99 - \theta_{CO} - \theta_{OH}) \tag{4.23}$$

$$\nu_{OH,a} = k_{OH,a} \, (\theta_{OH}^{m} (1 - \theta_{CO}) - \theta_{OH}) \exp(\frac{\alpha F \phi_{DL}}{RT}) \tag{4.24}$$

$$\nu_{OH,d} = k_{OH,d} \, \theta_{OH} \exp(\frac{-(1-\alpha) F \phi_{DL}}{RT}) \tag{4.25}$$

$$\nu_{r} = k_{r} \, \theta_{CO} \theta_{OH} \exp(\frac{\alpha F \phi_{DL}}{RT}) \tag{4.26}$$

In the above equation θ_{CO} and θ_{OH}, denote the coverages of CO and OH on the electrode surface, and c_s the concentration of CO close to the electrode surface. The parameter θ_{OH}^{m} is the maximum OH coverage, and $k_{CO,a}$, $k_{OH,a}$, $k_{OH,d}$, and k_r denote the rate constants of CO adsorption, OH adsorption, OH desorption and the reaction rate constant between CO and OH at $\phi_{DL} = 0$, respectively. In this model CO desorption, which is known to occur on a very long time scale, is neglected. F, R and T have their usual meanings and α denotes the symmetry factor. (Note that above α denoted a control gain. Since from the respective context it should be obvious which meaning α has, we refrained from introducing different symbols for these two quantities.) As in [45], a maximum coverage of adsorbed OH, θ_{OH}^{m}, was assumed to avoid a complete blocking of CO adsorption by OH at higher potential, and the CO coverage was limited to 0.99 to allow for some OH adsorption on the CO-poisoned state at low potentials such that the reaction can ignite spontaneously. For all reaction steps involving charge transfer, a Butler-Volmer-type expression was used. With the defined reaction rates the differential equations determining the evolutions of the coverages θ_{CO} and θ_{OH} are given by:

$$\frac{d\theta_{CO}}{dt} = \nu_{CO,a} - \nu_{r} \tag{4.27}$$

$$\frac{d\theta_{OH}}{dt} = \nu_{OH,a} - \nu_{r} - \nu_{OH,d} \tag{4.28}$$

The Faradaic current i_F is obtained from the sum over all charge transfer process

$$i_F = F S_{tot} A (\nu_{OH,a} - \nu_{OH,d} + \nu_{r}) \tag{4.29}$$

where S_{tot} is the total number of active sites on the surface per unit area. The finite mass transport rate of CO from the bulk of the electrolyte to the surface was modelled by employing the simple diffusion-layer model as discussed in chapter 2, section 2.1.3.

$$\frac{dc_s}{dt} = -\frac{2S_{tot}}{\delta}\nu_{CO,a} + \frac{2D}{\delta^2}(c_b - c_s) \tag{4.30}$$

Here, δ is the thickness of the diffusion layer, c_b the bulk CO concentration, and D the diffusion coefficient of CO in the bulk solution. The parameter δ is controlled by the rotation rate of the electrode. This model was augmented by the charge balance equation as discussed above to allow a change of the double layer potential, ϕ_{DL}.

$$C_d \frac{d\phi_{DL}}{dt} = -i_F(\phi_{DL}) + \frac{U - \phi_{DL}}{R_\Omega} \tag{4.31}$$

where C_d is the double layer capacitance, U the applied voltage.

Parameters	Value	Unit
c_b	10^{-3}	$mol.l^{-1}$
D	5×10^{-5}	$cm^2.s^{-1}$
δ	0.0019	cm
S_{tot}	2.2×10^{-9}	$mol.cm^{-2}$
$k_{OH,a}$	10^{-4}	s^{-1}
$k_{OH,d}$	10^{5}	s^{-1}
$k_{CO,a}$	10^{8}	$cm^3.mol^{-1}.s^{-1}$
k_r	10^{-5}	s^{-1}
θ_{OH}^{m}	0.333	
α	0.5	
T	300	K

Table 4.1: Parameters used in the simulation

In the simulations R_Ω was set 1 kΩ to account for the series resistance employed in the experiments. All other parameters used in the simulation are given in table 4.1 except the applied voltage and the double layer capacitance C_d, which are used as control parameters. A one-parameter bifurcation diagram computed with the above described model as a function of the applied voltage U is depicted in Figure 4.7a for a double layer capacitance of 5 mF. In Figure 4.7a, the current voltage curve increases monotonically, as found in the experiments when a sufficiently high series resistance was used (*cf.* Figure 4.3b). Moreover, the steady state undergoes two Hopf bifurcations marked with 'H'. Thus, the oscillatory region is limited to a potential window on the autocatalytic

branch, again as found in the experiments. Figure 4.7b shows the bifurcation diagram as a function of the double layer capacitance for U = 1210 mV. This figure shows that the steady state loses stability when the capacitance exceeds 1.8 mF. In this figure also the maximum and minimum of the limit cycles are shown. We can deduce that the Hopf bifurcation is supercritical since the amplitude of the oscillations rises gradually from the point H.

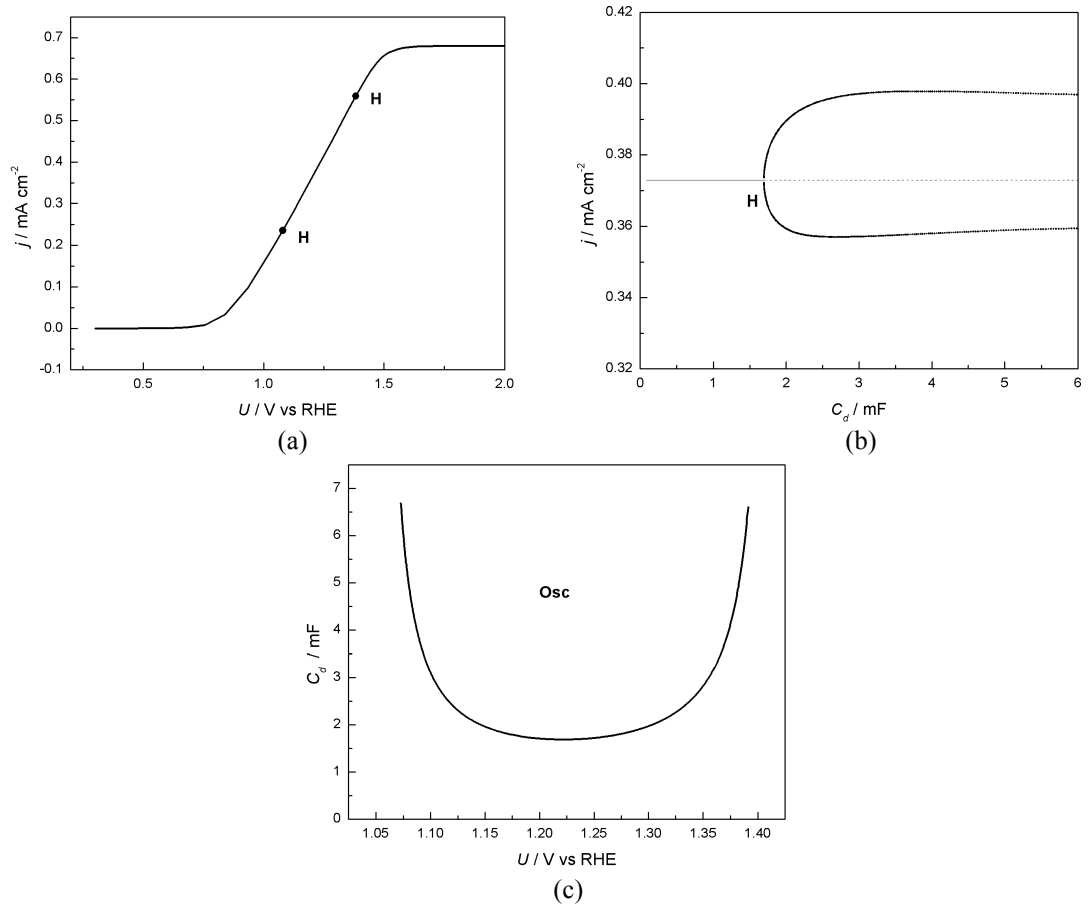

Figure 4.7: (a) One parameter bifurcation diagram showing the stationary current vs. applied voltage. The steady state is unstable between the two dots marked by an 'H', which indicates that the instability arises through a Hopf bifurcation; C_d = 5 mF; R_Ω = 1 kΩ (b) One parameter bifurcation diagram showing the stationary states (thin line) and of the maximum and minimum of oscillations (thick line) as a function of the double layer capacitance. This solid (dotted) line marks a stable (unstable) stationary state. U = 1210 mV (c) Two-parameter bifurcation diagram showing the region of oscillations in the capacitance applied voltage plane.

Figure 4.7c shows a two-parameter bifurcation diagram in the capacitance applied voltage parameter plane. The solid curve divides the C_d-U parameter plane into an oscillatory and a stationary region. This curve not only closely resembles the curve obtained in the experiments but also comes quantitatively close to the experimentally measured value. In particular, it shows the existence of a lower limit of the capacitance

necessary for a Hopf bifurcation to occur. The experimentally observed minimum value for the capacitance was 2.3 mF, whereas the simulation predicts oscillations above 1.76 mF, which is a very good agreement in view of the many simplifications made in the derivation of the model. However, as can be seen by a comparison of Figure 4.8a and b, there is a pronounced difference between the form of

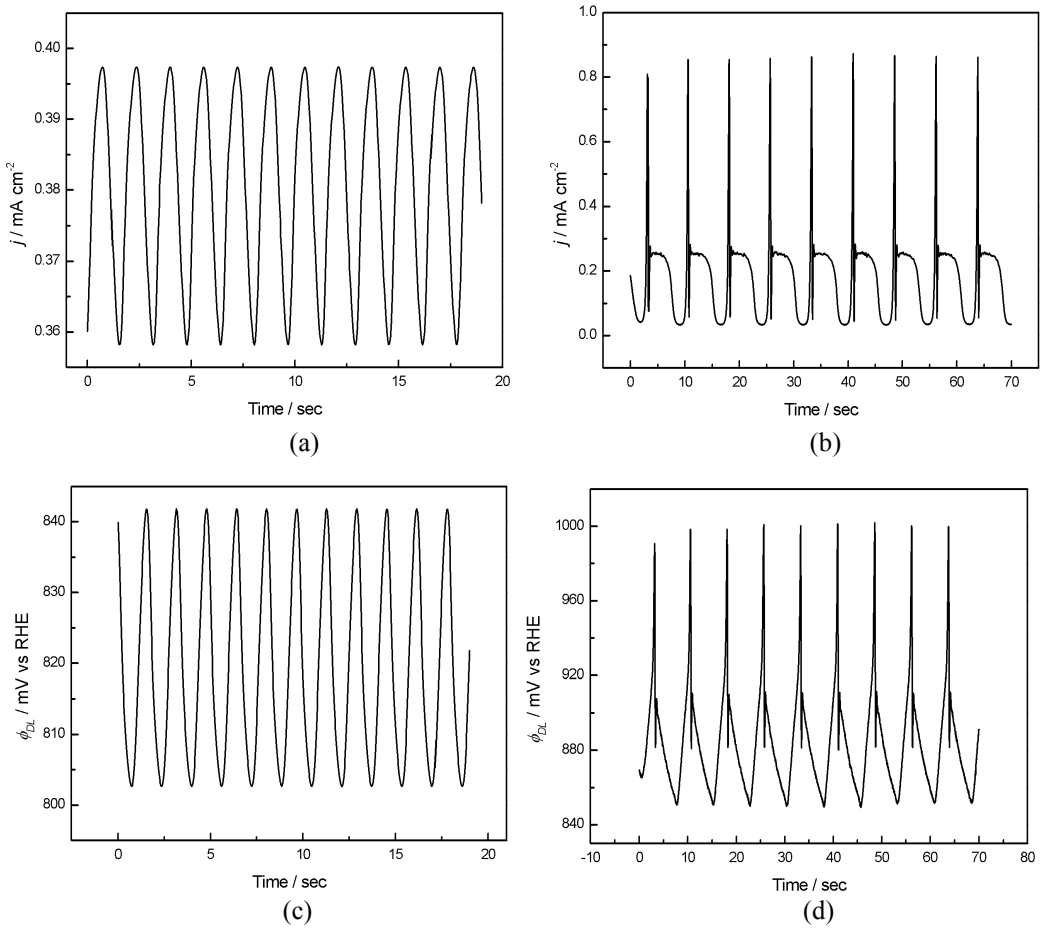

Figure 4.8: Time series of current oscillations as obtained (a) in the simulation (C_d = 4 mF, R_Ω = 1 kΩ, U = 1200 mV) and (b) in experiment (C_d = 4 mF, R_Ω = 1 kΩ, U = 1070 mV); time series of ϕ_{DL} as obtained (c) in the simulation (d) in the experiment.

the time series in experiment (Figure 4.8b) and simulation (Figure 4.8a). The period of the experimental oscillations differs by a factor of 3, and they exhibit an overshooting of the current which triggers an oscillatory approach to the 'base oscillation'. These features are absent in the simulations. As mentioned before, the overshooting is likely to stem from an autocatalytic removal of the CO monolayer, while the subsequent fast and damped oscillations are probably an artefact of the electronics. In our model, a simple mean field approximation is used to model CO electrooxidation. Hence, any mutual interaction among adsorbed CO molecules as well as between adsorbed CO molecules

and specifically adsorbed anions is neglected. In the experiments, it is however likely that interactions between adsorbed species cause the overshooting of the current. This conjecture is supported by the fact that the sharpness of the peak varies with the nature of the anions in the solution. Therefore, we cannot expect that this feature is captured in the simulations.

The simulated variation of the cell voltage with time is shown in Figure 4.8c. The cell voltage changes periodically between 803 mV and 842 mV. Figure 4.8d shows the experimental cell voltage, which has a triangular waveform with sharp spikes superimposed. Apart from the spikes (which have the same origin as those in the current), the voltage varied between 850 mV and 910 mV, which is similar in amplitude as the simulated ones. Therefore, except for the first sharp increase in current density, the simple mean field model used here reproduces the experimental findings, most importantly the critical electrode capacitance above which the system becomes oscillatory. This confirms the existence of a positive feedback loop in the kinetics of CO electrooxidation, which might be also the source for other dynamic instabilities which will be further investigated in the following chapters.

4.6 Summary

In this study, a derivative feedback control is used with an external electronic controller to change the time scale of the activator variable of a dynamical system. More precisely, we investigated the response of CO electrooxidation on platinum upon a change of the effective capacitance. When the capacitance exceeds a critical value, oscillations could be established. This confirms two basic properties of the dynamics of CO electrooxidation discussed in the literature, namely that (a) the reaction mechanism contains a positive (autocatalytic) feedback loop and (b) the double layer potential act as an inhibitory variable.

Chapter 5: Effect of Low CO Concentration and Diluted Supporting Electrolyte

In the last chapter, the existence of a chemical autocatalytic feedback during CO electrooxidation on Pt was proven. The chosen reaction conditions were typical conditions for electrochemical experiments, which includes that the supporting electrolyte has a high ionic strength. In this way, the *iR*-drop in the electrolyte is minimized. However, anions from the electrolyte also interact with the electrode surface, and thus influence the reaction kinetics and possibly also the reaction mechanism. Up to now studies on CO electrooxidation assume that the interaction between adsorbed species is through the competition of CO, OH, and possibly also anions for free surface sites while interactions among adsorbed species are neglected. Since under the considered conditions, the surface tends to be either fully CO covered (when the electrode potential is negative to the onset of OH adsorption) or quasi-free of adsorbed CO and OH (on the reactive branch) this conjecture is a good approximation. However, at lower anion and/or CO concentrations the situation might be different. In particular, a low concentration of both, CO dissolved in the electrolyte and supporting electrolyte, might favour OH adsorption and thus enhance the rate of CO electrooxidation, which constitutes a desirable situation. Furthermore, intermediate coverages might be adjustable at lower CO and anion concentrations and cooperative effects between adsorbed species that are hidden at high concentrations might become detectable. The latter might alter the feedback loops of the system. Understanding CO electrooxidation in wide concentration ranges of all the species involved in the reaction mechanism is thus especially important for understanding and predicting dynamic instabilities in this system. These considerations motivated the studies discussed in this chapter, namely investigations of the impact of the concentrations of bulk CO and the supporting

electrolyte on the mechanism of CO electrooxidation on Pt electrodes. The three low indexed single crystal orientations of polycrystalline Pt were employed as electrodes. Most studies were carried out either in diluted sulphuric acid or perchloric acid electrolytes, which are the most common electrolytes in electrocatalytic studies. In section 5.1, we focus on transient behaviour at CO concentrations lower than the one of the cusp at the respective conditions, i.e. on conditions under which the bistability does not exist anymore. As will be demonstrated, these conditions allow for more negative potentials of the onset of CO electrooxidation than reported so far. In section 5.2, the influence of the relative concentrations of the three adsorbing species on the bistable behaviour, which exists above a critical CO concentration, is discussed with special emphasis on the position of the saddle node bifurcation of the active branch. The most negative value of the latter is indicative of the most negative potentials at which reactive OH-groups that can maintain a stationary reaction rate exist on the surface.

5.1 Impact of low CO and anion concentrations on the CO electrooxidation rate on Pt single crystal surfaces

5.1.1 Experimental results

In this section, we present results on CO electrooxidation on the three low-indexed surface orientations of platinum, namely Pt (110), (100), and (111), in diluted supporting electrolytes and low CO bulk concentration. The rate of CO electrooxidation depends sensitively on the relative adsorption rates of CO, anions, and oxygenated species that may oxidize CO, i.e. OH^-, activated H_2O, or water complexes of the latter two species. For simplicity, we refer below to all species that can oxidize CO as OH^-. The main interest in studies on CO electrooxidation on Pt is to find conditions, which allow CO to be oxidized at potentials as negative as possible. Using low concentrations of anions and CO favours the adsorption of OH^- compared to the so-far nearly exclusively studied CO saturated electrolytes of high conductivity, and thus high anion concentration. Therefore, we can expect that the onset of CO electrooxidation is shifted negatively under the conditions investigated in this chapter. These conditions are also especially relevant for fuel cells since the CO contamination of the H_2 feed gas is in the ppm regime.

Let us first focus on the results obtained with Pt(110) in 1 mM H_2SO_4 and a CO concentration of 0.5%. To guarantee reproducible conditions, after flame annealing and insertion of the electrode into the electrochemical cell (*cf.* section 3.4.2), the system was allowed to establish a stable gas concentration. This needed about 20-30 minutes and during this time the electrode potential was cycled in the potential region 50 mV - 200 mV. Thereafter cyclic voltammograms were recorded at a scan rate of 20 mV/s and increasing negative turning potential while the positive turning potential was kept at about 766 mV such that the formation of irreversible oxide was excluded. In the first CV the negative turning point was thus 50 mV and the CO monolayer, which formed during cycling in the H-upd region, is oxidized around 700 mV. When increasing the negative turning point, there was a threshold potential positive of which CO was oxidized during the first or the first few cycles at astonishingly negative potentials. However, this negative CO electrooxidation wave shifted towards positive potentials in consecutive CVs until a stable CV was obtained in which the electrooxidation wave maximum was about 100 mV more positive than initially. A typical example is shown in Figure 5.1, where the negative turning point was kept at 434 mV. It can be seen that in the first CV the peak maximum is slightly negative to 600 mV, a truly low value for a Pt(110)-1×1 electrode. After a few CVs the electrooxidation wave maximum shifted positively by more than 100 mV. The same behaviour was observed when further increasing the negative turning point up to a second threshold potential positive of which the oxidation peak was from the beginning at its more positive value and the CVs were stationary from the beginning.

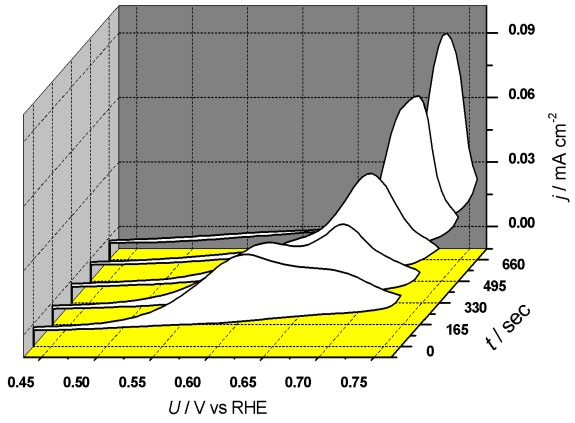

Figure 5.1: Cyclic voltammograms of a rotating Pt(110) electrode in 1 mM H_2SO_4 purged with 0.5 % CO in Ar after adjusting the negative turning point to 434 mV from an originally more negative value. Scan rate: 20 mV/s; rotation rate: 1200 rpm.

Further experiments were conducted with different CO and H_2SO_4 concentrations as well as with different supporting electrolytes. At a CO concentration of 0.3% and otherwise identical conditions the electrooxidation current was so low that an electrooxidation peak could be hardly seen and no conclusive results could be obtained. In contrast, already at a slightly higher CO concentration of 0.8%, the electrooxidation maximum was from the first CV on at the position of the final maximum that was obtained with 0.5% CO, i.e. no shift of the electrooxidation wave was observed.

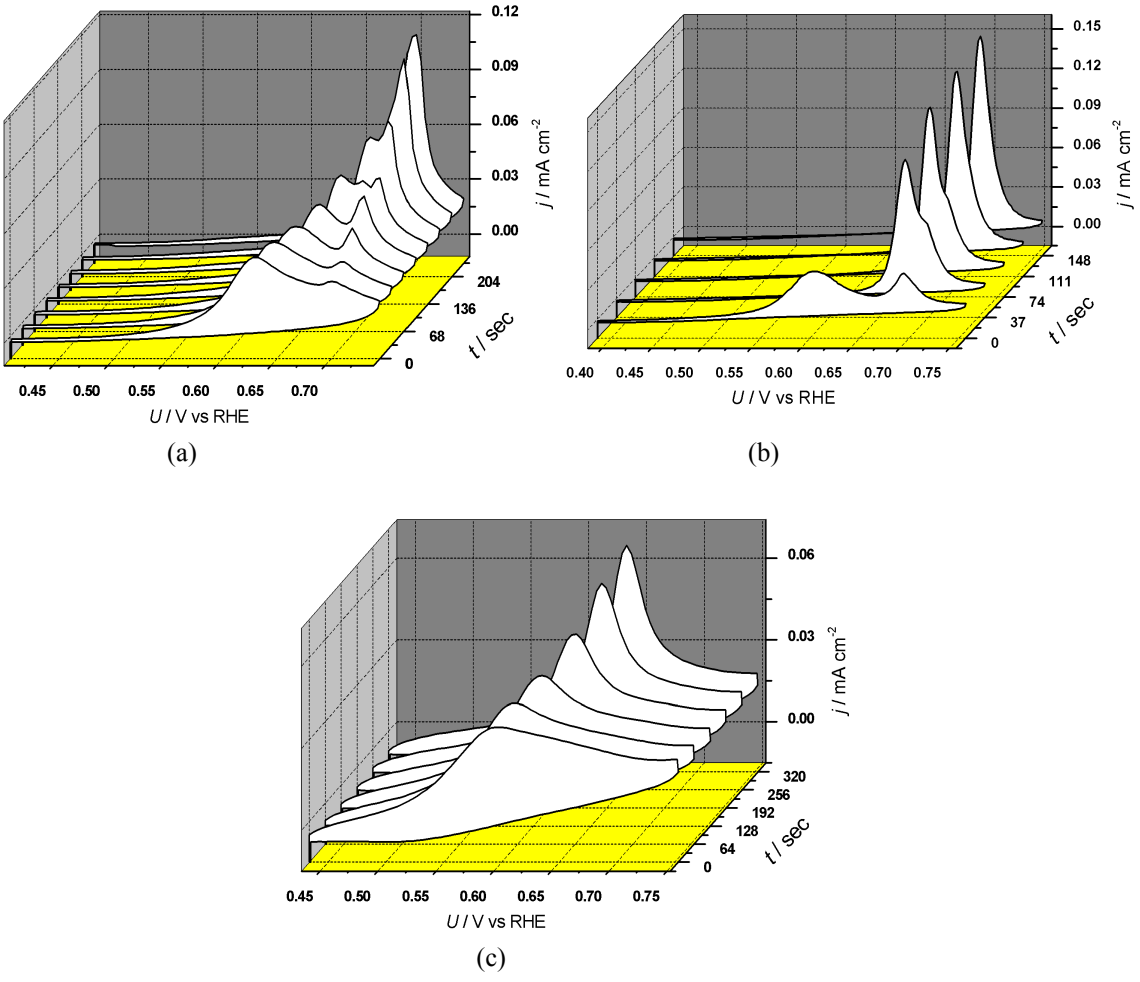

Figure 5.2: Cyclic voltammograms of a rotating Pt(110) electrode in different electrolytes, each purged with 0.5% CO in Ar: (a) 10 mM H_2SO_4; negative turning potential 400 mV; (b) 10 mM $HClO_4$; negative turning potential: 386 mV; (c) 10 mM HBF_4 negative turning potential 434 mV. In all cases, the CVs were recorded immediately after increasing the negative turning potential to the given values. Scan rate: 20 mV/s; rotation rate: 1200 rpm.

On the other hand, when increasing the H_2SO_4 concentration to 10 mM or changing the nature of the anion, the peak transition was preserved. Corresponding experiments with 10 mM H_2SO_4, 10 mM $HClO_4$, and 10 mM HBF_4 are shown in Figs. 5.2 (a) - (c). As

evident from this figure a shift of the electrooxidation wave with time occurs for all three electrolytes, though the shapes of the CVs and the time needed until stationary CVs were obtained differed in the three cases. In H_2SO_4 the main electrooxidation peak occurred initially at about 600 mV and shifted with time to about 700 mV (Figure 5.2 (a)). The evolution of the CVs, especially the double peak structure of the intermediate CVs, suggests that there are two distinct CO populations in different adsorption configurations. One of them dominates initially and is slowly replaced by the second one. A comparison with Figure 5.1 shows that in the higher supporting electrolyte concentration the stationary CV adjusts more quickly. In $HClO_4$, the situation is qualitatively similar to the one in H_2SO_4: Initially the CV shows two distinct maxima of the electrooxidation current that are even better separated than in H_2SO_4. They evolve quickly to a single humped electrooxidation wave with the maximum at approximately the position of the initially more positive maximum. The separation of the maxima is again about 100 mV and their position is about 20 mV more negative than in H_2SO_4 electrolyte. In HBF_4, only one electrooxidation peak is discernable around 600 mV. It shifts with time by about 50 mV.

In order to obtain a rough estimation of the CO coverage, the current was integrated in the region in which CO electrooxidation occurred for successive positive scans. A plot of the cumulative charge versus voltage for eight successive scans in 10 mM H_2SO_4 is shown in Figure 5.3. The entire charge during the positive scan amounts to approximately 225 $\mu C/cm^2$. This is considerably less than the integrated charge flowing during the electrooxidation of a full monolayer of CO in a stripping experiment, which was found to lie between 380 $\mu C/cm^2$ [14] and 340 $\mu C/cm^2$ [158]. Taking 360 $\mu C/cm^2$ as an intermediate value, the charge flowing in a positive scan of the experiments shown in Figure 5.3 amounts to about 60% of a ML. However, in contrast to the stripping experiments, in our case there are three contributions to the measured charge: (a) capacitive current, (b) electrooxidation current of pre-adsorbed CO and (c) bulk electrooxidation current. Thus, we can conclude that in our case 0.6 ML is an upper bound of the CO coverage. We did not make an attempt to correct for the capacitive and the bulk electrooxidation current, since the errors would remain so large that when doing so we would not obtain further insight. But we can extract more information from Figure 5.3: Above a charge of approximately 200 $\mu C/cm^2$ all curves are parallel to each other. This suggests that at the respective potentials the pre-adsorbed CO is entirely oxidized

and the additional current flowing up to the positive turning potential is exclusively due to charging of the electrode and bulk CO electrooxidation. This, in turn, means that the

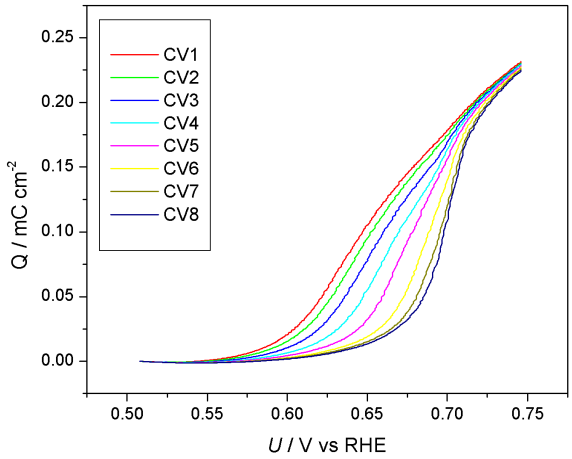

Figure 5.3: Cumulative charge during the positive scan vs. potential for successive potential scans of a Pt(110) electrode in 10 mM H_2SO_4 purged with a mixture of 0.5% CO in Ar. Scan rate: 20 mV/s; rotation rate: 1200 rpm; scan range: 406 mV–746 mV.

amount of preadsorbed CO is approximately the same in all experiments. Therefore, the shift in electrooxidation potential is not caused by different surface coverages of CO. Moreover, we can lower the upper limit of the CO coverage in these experiments to 0.5 ML. In Figure 5.3, we can also see that the overall charge at the positive turning potential decreases slightly from scan to scan. This difference reflects the fact that when the pre-adsorbed CO is oxidized at more positive potentials, also the contributions of the bulk CO electrooxidation current and the charging currents are smaller. The first one accounts on the one hand for the smaller number of surface sites available for bulk electrooxidation, and, on the other hand, for the fact that if preadsorbed CO is oxidized at a lower rate, this is also true for bulk electrooxidation. The latter results from the fact that the capacitance of a CO covered electrode is considerably smaller than of the bare electrode. Still, the difference between the total electrooxidation current in the first and last CVs is less than 10%, ensuring that the contributions of bulk CO electrooxidation and double layer charging are 'secondary effects', whose order of magnitude lies within the experimental error. In conclusion, Figure 5.3 suggests, firstly, that about the same amount of CO is oxidized during each positive scan irrespective of the position of the electrooxidation wave maximum; and, secondly, that the CO coverage in the experiments did not exceed 0.5 ML.

When increasing the anion concentration to 100 mM or 0.5 M, a stationary CV was obtained from the first cycle on. Thus, electrooxidation of CO at the remarkably low overpotentials somewhat below 600 mV is a transient phenomenon and occurs only in small concentration ranges of CO and anions.

To test whether the observed shift in CO electrooxidation potential is due to a slow relaxation of the surface after transfer of the electrode into the electrolyte subsequent to the flame annealing procedure, we conducted the same voltage scan protocol as described above twice, first in an Ar saturated electrolyte and then under purging with a Ar-CO(0.5%) gas mixture. In both cases, the voltage was first cycled for 25 minutes between 50 and 200 mV to guarantee saturation of the electrolyte with the respective purge gas. Then, the positive turning point was increased to 750 mV and the negative turning point was increased in small steps. The corresponding results for the initially Ar saturated electrolyte are shown in Figure 5.4a. Clearly, qualitatively the same trend can be seen as before: In the first CVs a considerable amount of CO is oxidized at low potentials between 600 and 700 mV, the electrooxidation wave shifting from cycle to cycle towards more positive potentials until a stationary CV with a sharp current peak around 725 mV establishes.

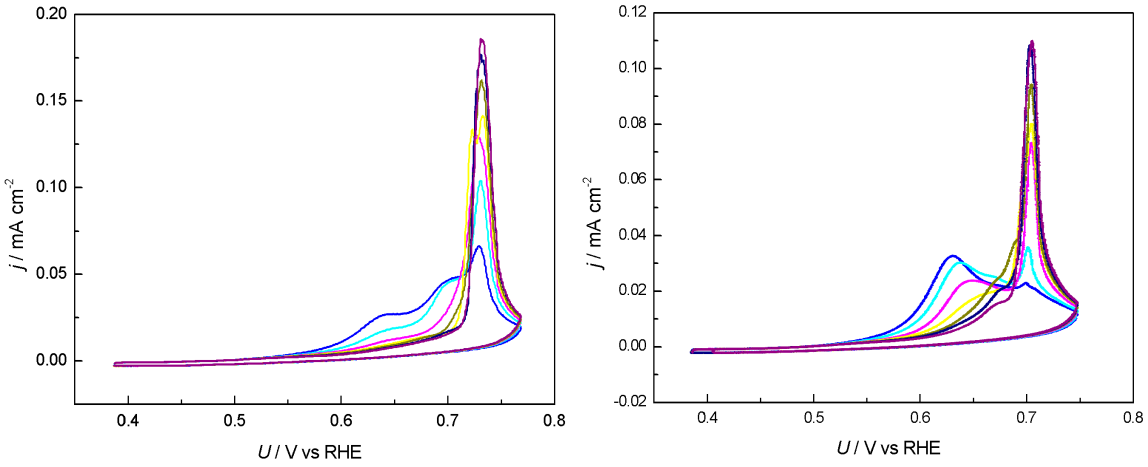

Figure 5.4: Cyclic voltammograms of Pt(110) in 10 mM H_2SO_4 purged with an 0.5% CO/Ar mixture. (a) Prior to purging with the CO/Ar-mixture, the electrolyte was saturated with Ar and the potential was cycled between the same limits as in the subsequent experiments with CO. (b) The electrode was inserted in the Ar/CO purged electrolyte and the CVs were recorded according to the standard procedure (see text). Further parameters ((a) and (b)): scan rate: 20 mV/s; rotation rate: 1200 rpm; lower turning potential: 386 mV.

For comparison, Figure 5.4b shows the corresponding experiment without first cycling in Ar saturated electrolyte. It demonstrates that both experiments exhibit quantitative differences: When first cycling the electrode in Ar-saturated electrolyte, the low-potential electrooxidation wave is less pronounced in the first scan and shifts more quickly towards positive potentials. This points to the fact that the surface is slightly changing when the electrode is cycled in the inert electrolyte. However, the experiments also show that this is a 'second order' effect rather than the primary origin of the peak shift. When starting the potential cycles in the CO-containing electrolyte, the first CVs are far from the stationary ones, the time from the insertion of the electrode in the electrolyte being more than twice as long as the time it takes the system to establish a stationary CV in a CO-containing electrolyte. Hence, a simple relaxation of the electrode with time cannot be the main reason for the peak shift.

As already mentioned, the described 'peak transition phenomenon' occurred when increasing the negative turning potential to values within a certain potential range. Also, after a stationary cyclic voltammogram had adjusted, the same scenario reoccurred when further increasing the negative turning point by a small amount up to some positive potential limit. Figure 5.5a and 5.5b illustrate this observation. The blue and the red curves are for lower turning potentials of 405 and 425 mV, respectively. First, the CVs shown in blue were recorded. On the right, the first CV recorded after the negative turning point was increased is shown and on the left the resulting stationary voltammogram. After the latter had adjusted, the negative turning potential was increased to 425 mV. Immediately afterwards the red curve in Figure 5.5a was measured. With time, it converted to the red curve shown in Figure 5.5b, which again is a stationary CV. This procedure could be repeated until a maximum value for the lower turning potential was reached.

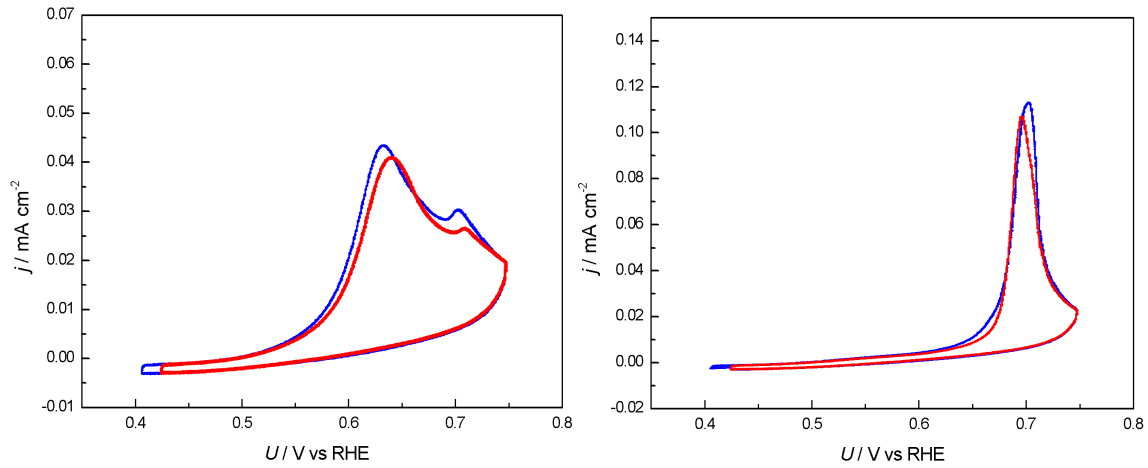

Figure 5.5: First (a) and stationary (b) cyclic voltammograms of a Pt(110) electrode in 10 mM H_2SO_4 purged with a 0.5% CO/Ar mixture. Blue curves: negative turning potential 405 mV, red curves: negative turning potential 425 mV. The red curve in (a) was recorded immediately after the blue one in (b). Scan rate: 20 mV/s; rotation rate: 1200 rpm.

This observation is highly non-trivial and will be discussed below in more depth. At this point, we just mention that it allows 'trivial' origins to be excluded, such as a drift in the CO concentration in front of the electrode due to imperfect mixing at the beginning of the experiment, or a changing pH value at the electrode due to the ongoing CO electrooxidation. In both cases, a small change of the cycled potential window would not re-establish the original concentration relations. This, however, would be required if the shift of the electrooxidation wave would just reflect a concentration change.

The maximum value of the negative turning point at which a shift of the electrooxidation peak towards positive potentials appeared was 440 mV. When choosing the negative turning point positive to 440 mV, again, from the first CV on, a stationary CV was observed with the electrooxidation wave around 700 mV, i.e. at approximately the same potential as in the stationary CVs for lower left turning points. The impact of the positive turning point on the electrocatalytic response of the electrode was explored to a much smaller extent since at higher potentials also some amount of irreversible oxide forms, whose reduction roughens the electrode surface, and, therefore, leads to a change of its electrocatalytic properties. However, we found that increasing the upper turning potential by 40 mV had no influence on the CVs, and thus also not on the peak transition phenomenon.

After a stationary CV had adjusted, there was no means by which the initial negative electrooxidation wave could be re-established for the same or a more negative left

turning point. Also keeping the electrode in the hydrogen upd region for some time did not lead to a recovery of the low electrooxidation potential. Only when the crystal was once again flame annealed, the peak transition phenomenon reappeared.

In summary, we found that in case of Pt(110) the CO electrooxidation peak shifts with time in the positive direction when the following conditions are met: (a) The CO concentration in the electrolyte is low; (b) the concentration of the supporting (weakly acidic) electrolyte did not exceed 10 mM; and (c) the left turning point was chosen somewhere between 326 and 440 mV. The phenomenon was observed in H_2SO_4, $HClO_4$ and HBF_4 acid solution, whereby the shapes of the electrooxidation waves differed in the three electrolytes slightly.

We conducted further experiments to examine whether the peak shift is restricted to the Pt(110) surface or also occurs on other surface orientations. In case of Pt(100) features very similar to those of Pt(110) were obtained. Figures 5.6a and 5.6b show the results for Pt(100) in 10 mM H_2SO_4 and 10 mM $HClO_4$, respectively.

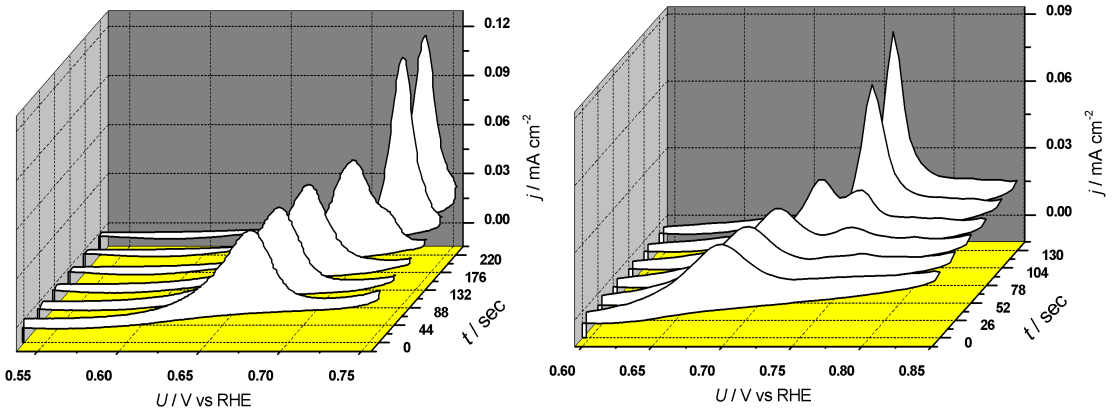

(a) (b)

Figure 5.6: Cyclic voltammograms of a rotating Pt(100) electrode in different electrolytes, each purged with 0.5% CO in Ar: (a) 10 mM $HClO_4$; negative turning potential 536 mV (b) 10 mM H_2SO_4; negative turning potential: 596 mV; scan rate: 20 mV/s; rotation rate: 1200 rpm.

Again, the potential scan rate was 20 mV/s and the CO concentration 0.5%. Clearly, in both electrolytes the CO-electrooxidation wave shifted with time towards positive potentials, as it was found for Pt(110). However, the potential range in which the peak transition occurs differs remarkably for Pt(110) and Pt(100). For Pt(100) it is smaller than for Pt(110) and shifted considerably in the positive direction: In absolute numbers,

in the case of Pt(110) the potential shift occurred when the negative turning point lay between 326 mV–440 mV, in the case of Pt(100) it appeared for turning points between 527 mV–577 mV.

Corresponding experiments were also conducted with a Pt(111) electrode. Figure 5.7 shows exemplary for all the experiments with Pt(111) the first three CVs obtained in 10 mM H_2SO_4 and a negative turning potential of 426 mV. Clearly, in this case the CVs are superimposed from the first one on with the maximum of the electrooxidation peak at about 700 mV, i.e. close to the values at which it also occurred in the stationary limit for Pt(110) and Pt(100). This reveals how intricate the interaction of CO, OH^-, and anions with the surface structures are.

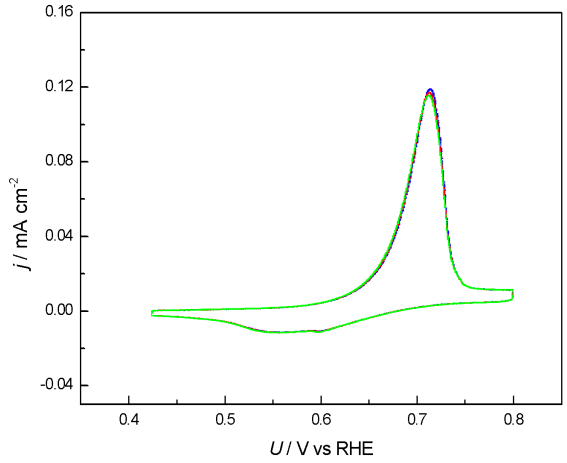

Figure 5.7: Cyclic voltammogram of Pt(111) in 10 mM H_2SO_4 electrolyte purged with a 0.5% CO/Ar gas mixture; scan rate: 20 mV/s; rotation rate: 1200 rpm; lower turning potential: 426 mV.

5.1.2 Discussion

Above, we demonstrated that the electrooxidation of CO on Pt(110) and Pt(100) electrodes from electrolytes with low concentrations of anions and dissolved CO exhibits complex time-dependent features. However, the cyclic voltammograms became stationary after some time. Let us first compare the catalytic activity of the surfaces as obtained from these stationary voltammograms with literature data obtained in electrolytes of high conductivity, and therefore high anion concentration. In the following discussion, we take the potential values at the current maxima in the CVs as a measure of the reactivity of the surface. For Pt(110)-(1×1) they are at 700 ± 20 mV in our diluted electrolytes. The Pt(110)-(1×1) surface is the least reactive of the three low-indexed Pt surfaces [17], and only two types of data are available in literature: Current

voltage characteristics in CO-saturated, 0.5 M H_2SO_4, and so-called stripping voltammograms [14]. The latter are obtained in the following way: Firstly, CO is adsorbed for some time at a given potential from a CO-containing electrolyte (in most cases CO-saturated solutions). Then, the electrolyte is purged with Ar to drive out all dissolved CO. Finally, the adsorbed CO is oxidized during a voltage scan and the corresponding electrooxidation current recorded. In case of CO-saturated H_2SO_4, the surface remains completely inactive up to a potential of 880 mV, which is about 200 mV more positive than in our case. In contrast, the stripping peak of a monolayer CO is observed at about 720 mV, which is close to the current maximum in our stationary CVs. Our working hypothesis is that CO electrooxidation proceeds through the Langmuir-Hinshelwood mechanism, but CO and OH not only compete with each other for free surface sites but also with anions. If we assume that the rate of CO adsorption is very low for CO concentrations of 0.5% and can be neglected to a first approximation compared to those of OH^- and anions, we can deduce from the similar position of the current maxima in the stripping experiments in 0.5 M H_2SO_4 and the 0.5% CO-bulk experiments in 1-10 mM H_2SO_4 that the concentration of the anions has only a minor influence. This can be rationalized by two facts: Firstly, the adsorption strength of $(H)SO_4^{-(-)}$ on Pt(110) and (100) is much lower than on Pt(111) since the anion is bound only through 1 or 2 O atoms as opposed to three in the case of Pt(111) [131, 159, 160]. Secondly, water molecules are incorporated in the adsorbate layer of $(H)SO_4^{-(-)}$, which can be oxidized. Thus, the inhibiting effect of sulphate with respect to CO electrooxidation is much lower than, for example, of halides. Thus, our experiments reveal (a) that at least for the Pt(110)-(1×1) surface the stripping experiments mimic the conditions of low CO concentration, as they might occur in a fuel cell, more closely than experiments with CO-saturated electrolytes, and (b) that the electrooxidation occurs in the same potential region for a full monolayer (as in the stripping experiment) and a partially covered surface. The main difference between the corresponding voltammograms is that the stripping peak is very sharp while for the lower CO coverage the electrooxidation peaks extend over about 70 mV, the onset of electrooxidation being at somewhat more negative potentials.

For Pt (100) the main stripping peak in 0.5 M H_2SO_4 has its maximum at 770 mV [17], which again nearly coincides with the position of the maximum in our 10 mM H_2SO_4, 0.5% CO solution at 760 mV. Thus, also here the anion concentration seems to play only

a minor role, and the low-CO concentration electrolytes behave similar to stripping experiments. Contrarily, for CO saturated electrolytes the ignition potential at which CO electrooxidation commences is at 950 mV, and thus nearly 200 mV more positive.

The situation seems to be different for Pt(111), though also more complicated and somewhat controversial. Stripping experiments showed a dependence of the main electrooxidation peak on the coverage. Feliu et al. [11] report that for full coverage the stripping peak maximum occurs at 835 mV, while at coverages below 0.5 ML it lies 85 mV lower, i.e. at 750 mV. At intermediate coverages between 0.5 and 0.8 ML voltammetric profiles with two maxima at 750 mV and 835 mV are found. They interpret the results by the presence of two different types of CO island on the surface: At high coverage wide compact CO islands form, with possibly large CO-free (111) domains in between. At low coverages, the authors postulate a dispersion of small islands and small CO-free domains. Markovic et al. [38] report a strong dependence of the position of the stripping peak on the potential at which CO is preadsorbed. For a preadsorption potential of 375 mV the main electrooxidation peak lies at 820 mV. It shifts to about 800 mV for an adsorption potential of 150 mV, and it is lowest and splits into a bimodal stripping peak when CO is preadsorbed at 0 V. Above we showed that under continuous potential cycling between 400 and 800 mV in diluted sulphuric acid and 0.5% CO in the purge gas, a stationary CV adjusts immediately with an electrooxidation peak at 700 mV. This value is 120 mV more negative than the stripping peak for these adsorption potentials, pointing to a strong influence of (bi)sulphate adsorption. Hence, for the surface at which (bi)sulphate adsorbs most strongly a lower anion concentration considerably lowers the electrooxidation potential of CO.

Next, let us discuss the shift of the electrooxidation potential with time. Above, we showed that on Pt(110) and Pt(100) the first potential profiles after adjusting the negative turning points of a cyclic voltammogram in a certain intermediate potential window (coming from more negative turning points) exhibited a much better reactivity than after some time. More precisely, the CO electrooxidation maxima were more than 100 mV more negative. To obtain further insight into this pronounced initial reactivity increase several parameters were varied. The most pronounced influence was found when varying the concentrations. The negative electrooxidation currents only occurred for both, low CO and low anion concentration. This suggests that one requirement for the low

potentials is that the adsorption rate of OH^- has to be large compared to those of CO and anions. However, the ratio of these rates stays constant with time while the electrooxidation peaks shifts negatively. Hence, other factors must be present as well. We can exclude that it is a slow relaxation of the electrode surface after insertion of the freshly flame annealed electrode into the electrolyte, since the initially negative electrooxidation rates were also observed after treating the electrode at the same potentials in an Ar purged electrolyte (*cf.* Figure 5.3). Furthermore, also a reaction induced restructuring of the surface, or healing of reactive defects, seems to be unlikely, since after a stationary current-potential profile adjusted when scanning within certain potential limits, the low potential wave reappeared when increasing the negative turning point slightly. Furthermore, for the same reason we can exclude that the shift in electrooxidation potential is due to a slow change in the concentration of CO or the pH in front of the electrode. Quite astonishingly, on Pt(110) also the nature of the anion did not qualitatively alter the behaviour. (With Pt(100) and Pt(111) the experiments were only done in sulphuric acid.) More precisely, we used perchlorate as prototypical anion that adsorbs much more weakly than $(H)SO_4^{(-)-}$, and BF_4^- as representative of a very strongly adsorbing anion. Hence, the only common property of the different electrolytes that exhibited the peak shift phenomenon seems to be the low concentration of anions, which in turn determines the structure of the double layer. Therefore, we tentatively propose that it is the double layer structure that lies at the bottom of the low electrooxidation potentials. A change of the double layer structure with time then causes the electrooxidation potential to shift positively. The slow shift might occur because of a slow formation of water clusters, bonded via H-bonds, perhaps with anions incorporated that are more resistant with regard to electrooxidation to adsorbed OH_{ad} than free double layer water. This idea is in fact not completely new. That H-bonded water clusters might present a barrier for water activation, though in a completely different environment than here, had already been suggested in [26]. To prove this conjecture one would need to be able to conduct in-situ vibrational spectroscopy, i.e. FTIR (Fourier Transform infrared spectroscopy) or SFG (sum frequency generation). If our assumption were true the bending mode of water, usually being at about 1640 cm^{-1} in an electrochemical environment, would shift with time towards higher values due to strong lateral interactions of the H_2O molecules. Unfortunately, with single crystals both techniques cannot be done under bulk electrooxidation conditions. Rather, one is restricted to a thin

layer cell. Thus, the experimental conditions used here cannot be realized, and at present, our discussion remains speculative.

We thus conclude that for both, low CO and low electrolyte concentrations the electrooxidation of adsorbed CO occurs transiently at potentials considerably more negative than reported up to now. The low electrooxidation potentials move towards the stripping potentials with time. These are still considerably lower than the potentials at the onset of CO bulk electrooxidation in CO saturated solutions.

5.2 Effect of CO and anion concentration on the negative potential limit of the reactive branch

5.2.1 Experimental results

As already mentioned, studies of bulk CO electrooxidation have focussed on CO saturated electrolytes and the onset of CO electrooxidation when sweeping the potential in the positive direction. The latter is often referred to as firing potential. However, as discussed above, bulk CO electrooxidation exhibits bistability, and thus the reaction rate can also take on high values at potentials considerably negative to the firing potential. The most negative potential at which a high reaction rate is observed is given by the SN2 potential, as defined in Figure 2.18. The SN2 potential results from a delicate interplay of the relative rates of adsorption of CO, OH, and anions. In the following, the location of the SN2 point is investigated as a function of the CO and the anion concentrations.

Different CO concentrations were adjusted by premixing CO and Ar streams using a computer controlled mass flow controller (Bronkhrost). The correct operation of the in-house built gas mixture system was verified by measurements of the diffusion limited current density of CO electrooxidation as a function of the CO concentration. The linear relationship between both (Figure 5.8) confirms the proper operation of the set-up.

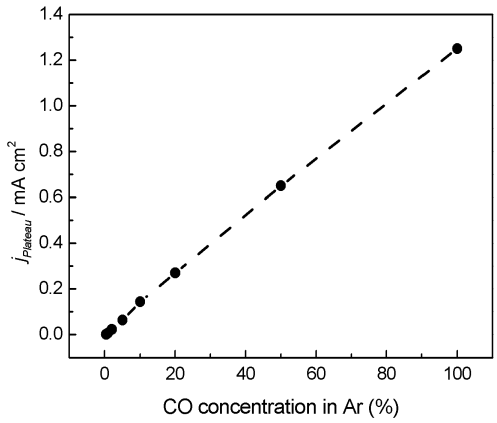

Figure 5.8: Diffusion limited current during bulk CO electrooxidation on a rotating Pt disk electrode in 0.5 M H_2SO_4 as a function of the CO concentration in the electrolyte. The linear relationship confirms that the gas-mixture set-up works properly. Rotation rate: 1200 rpm.

The SN2 potential was determined for various electrolyte compositions and CO concentrations according to the following protocol. First, the applied potential was increased starting from 440 mV (a potential value in the double layer region) at a scan rate of 20 mV/s. The positive turning potential was chosen slightly positive to the firing potential. On the reverse scan from positive to negative potentials, the scan rate was reduced to 5 mV/s. This procedure reduces kinetic effects on the backward scan, while the faster forward scan direction keeps the total time of the experiment short.

At an SN bifurcation, the system's variables undergo an abrupt transition from one state to another. Thus, ideally, the measurements would exhibit a jump in current density at the SN2 potential. At finite scan rates, in particular at low CO concentrations, the current decreased within a narrow potential interval (*cf.* Figure 5.9a) such that the determination of the SN2 potential by visual inspection of the CV was afflicted with uncertainty. To minimize the error, the SN2 potential was determined as follows. Straight lines were fitted to the diffusion limited plateau of the reactive branch and the transition region between the two current branches, respectively (section B and A in Figure 5.9a). The intersection of these two lines was taken as the SN2 potential.

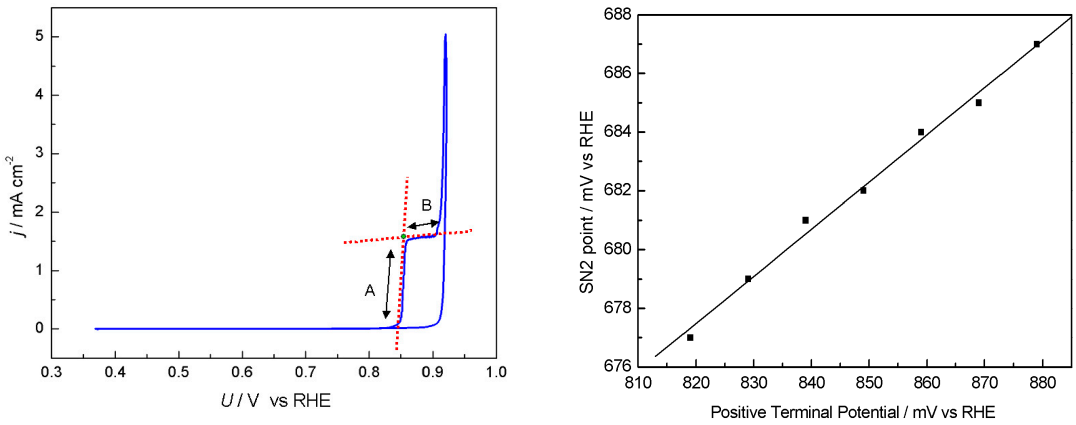

(a) (b)

Figure 5.9: (a) Illustration of how the SN2 potential was determined in experiments (see text); (b) Location of the SN2 potential as a function of the positive turning potential. Experimental conditions: (a) Electrolyte: CO saturated 0.5 M $HClO_4$; rotation rate: 1200 rpm; scan rate: 50 mV/s; (b) Electrolyte: 0.5 M H_2SO_4, 5% CO in Ar; rotation rate: 1200 rpm.

The above-mentioned experimental procedure allowed the system to undergo the transition from the poisoned to the reactive state at the SN1 bifurcation while minimizing the amount of irreversible oxide formed at high potentials. It was found that even small changes in the positive turning point affected the SN2 potential. This is demonstrated in Figure 5.9b in which the measured SN2 potential is plotted vs. the positive turning point, The SN2 point shifts linearly in the positive direction with increasing positive turning potential with a slope of approximately 1/6. This result strongly points to the fact that even though the positive terminal potential is kept well below the region in which irreversible oxide formation is known, a small amount of irreversible oxide forms nevertheless. The oxide is inreactive and is only reduced negative to the SN2 point. Thus, it occupies surface sites and therefore inhibits OH and CO adsorption. As substantiated below, this leads to a shift of the SN2 potential in positive direction.

The variation of the SN2 potential with the CO concentration for a polycrystalline platinum electrode is shown in Figure 5.10. In Figure 5.10a results in 0.5 M H_2SO_4 (dashed line) and 0.5 M $HClO_4$ (solid line) are displayed. Figure 5.10b displays corresponding measurements in 10 mM H_2SO_4 (dashed line) and 10 mM $HClO_4$ (solid line), respectively.

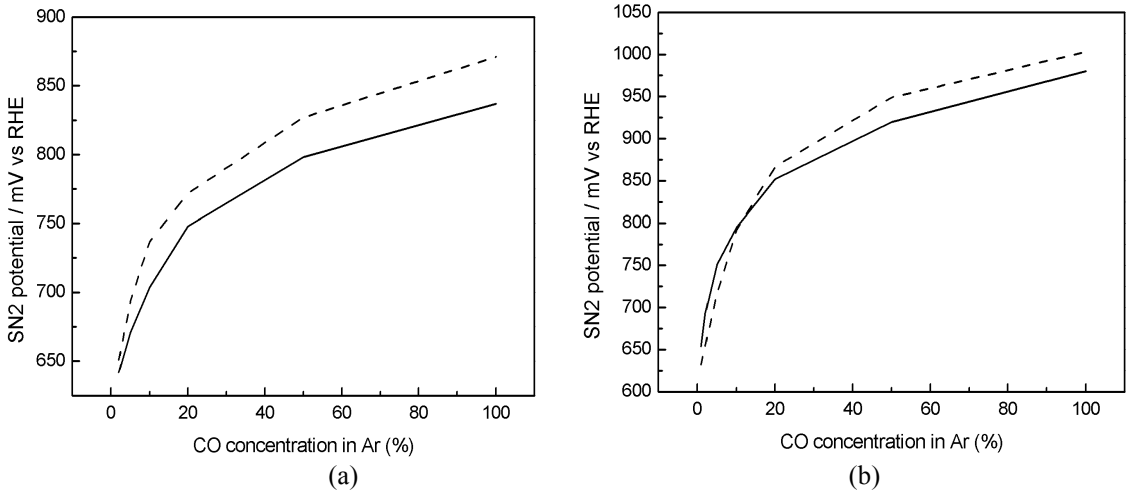

Figure 5.10: SN2 potential vs. CO partial pressure in the purging gas in concentrated (a) and diluted (b) electrolytes. (a) 0.5 M $HClO_4$ (solid line) and 0.5 M H_2SO_4 (dashed line) (b) 10 mM $HClO_4$ (solid line) and 10 mM H_2SO_4 (dashed line).

Figure 5.10 shows that the SN2 point moves in the negative direction with the reduction of the partial pressure of CO in the solution. This experimental finding supports the hypothesis that CO electrooxidation on platinum occurs through the LH mechanism and both CO and OH species compete for the active sites on the surface. As the CO concentration is lowered, OH species favourably compete with CO molecules for free surface sites at increasingly lower potentials, and the reaction continues as long as sufficient OH adsorbs on the surface. Therefore, the SN2 points move in the negative direction when reducing the CO partial pressure in solution. In sulphuric acid, the SN2 point is about 50 mV more positive than in perchloric acid, pointing to an inhibiting effect of (bi)sulphate ions.

In the case of the low acid concentration, the SN2 points are shifted towards more positive potentials compared to the higher acid concentration, its variation with the CO concentration following the same trend. It is likely that the difference in the double layer structure of concentrated and dilute electrolytes is responsible for the positive shift. According to Frumkin [65, 161, 162] the ionic strength of the electrolyte influences the effective potential difference between the electrode and the location at which a reaction takes place. CO is a neutral molecule and thus it does not experience electrostatic attraction or repulsion; therefore, its concentration in the reaction plane does not vary with the electrolyte concentration [72, 163, 164]. However, for an electron transfer occurring from the outer Helmholts plane (OHP), the energetic situation is different than

inthe bulk of the solution because of the potential drop ϕ_2 across the diffuse layer. Therefore, the rate of reaction is not controlled by the potential difference between the electrode and the bulk electrolyte, *U*, but by the amount *U*-ϕ_2, and the rate equation (equation (2.20) in chapter 2) for the forward reaction becomes

$$i = nAFk_0C_0^{''}e^{-\alpha nF(U-\phi_2-U_0)/RT} \tag{5.1}$$

The symbols in the above equation are explained in chapter 2, section 2.1.2. The above discussion is valid in the absence of specific adsorption. In the presence of specific adsorption the potential ϕ_2 is altered further, depending upon the amount of specifically adsorbed species [65], adding further ambiguity in the value of the potential in the reaction plane [165-167].

The influence of double layer effects can be avoided if the conductivity of the electrolyte is kept constant. Thus, in the following experiments the influence of adsorption of (bi)sulphate ions on bulk CO electrooxidation was investigated using supporting electrolytes that contained different amounts of H_2SO_4 and $HClO_4$ but a constant total anion concentration of 0.5 M. Figure 5.11a shows the variation of the SN2 point as a function of the ratio of sulphuric and perchloric acid (100% = 0.5 M H_2SO_4) for CO saturated electrolytes and a polycrystalline Pt electrode. The differently coloured points correspond to different sets of experiments. It is striking that the reproducibility of the experiments was quite poor, identical experimental conditions yielding an uncertainty of the SN2 potential up to 40 mV. This indicates that the SN2 point very sensitively depends on the state of the surface. Still, all of the experiments exhibited a clear trend: The SN2 point moved in the positive direction by about 70 mV when going from pure $HClO_4$ to an electrolyte containing 5% H_2SO_4, but remained approximately constant when the H_2SO_4 concentration was further increased up to 100 %.

The experiments were repeated with Pt(111) for two reasons: First, the adsorption strength of (bi)sulphate varies strongly on the three low-indexed Pt surfaces. It is much stronger on Pt(111) than on the other orientations [168]. Thus, the error observed with polycrystalline platinum might result from a different distribution of the various crystallographic surface orientations at different days. If this is true it should be smaller with Pt(111). Second, for Pt(111) adsorption isotherms of (bi) sulphate are available facilitating a quantitative interpretation. Before each individual experiment, the single

crystal was flame annealed to minimize the influence of changes in surface morphology, which occur during CO electrooxidation. The results are shown in Figure 5.11b. Clearly,

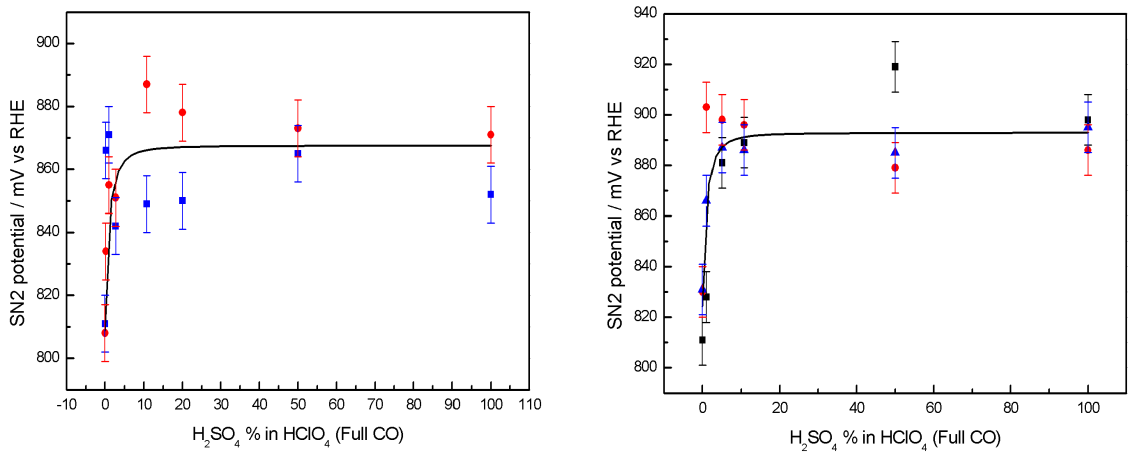

(a) (b)

Figure 5.11: Variation of the SN2 potential with the (bi)sulphate concentration in a CO saturated electrolyte (a) for polycrystalline Pt electrodes, (b) for Pt(111). The electrolytes contained different ratios of H_2SO_4 and $HClO_4$ such that the total anion concentration amounted always to 0.5 M. The different coloured points correspond to measurements of different days, the black curve is fitted.

the same trend as for polycrystalline Pt is found: the SN2 point shifts into the positive direction when adding small amounts of (bi)sulphate anions but remains nearly constant in the range between 10% and 100% (bi)sulphate anions. However, it is also apparent that even flame annealing before each single measurement cannot eliminate the large fluctuations. Despite of the poor reproducibility, the experimental findings support the hypothesis that (bi)sulphate anions block active sites. To further elucidate the results, theoretical calculations were carried out. They are discussed in the following section.

5.2.2 Modelling of CO bulk electrooxidation

In this section, we discuss in how far deterministic rate equations resulting from a mean field ansatz can reproduce the measured dependence of the SN2 potential on the concentrations of dissolved CO and adsorbing anions. First we neglect anion adsorption, and employ the mean field model as presented in chapter 4 section 4.5. Equations (4.23) to (4.30) are employed in the calculations, and the parameter values are taken from table 4.1 except the concentration of CO. A two parameters bifurcation diagram as a function of the electrode potential and the CO concentration is shown in Figure 5.12, the solid line

representing the location of the SN bifurcation at lower voltages. The location of the bifurcation was determined using the continuation program CONTENT [169].

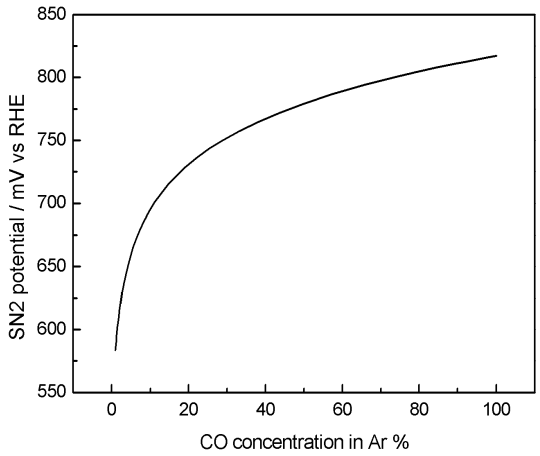

Figure 5.12: Simulated location of the SN2 potential as a function of the CO concentration for a rotation rate of 1200 rpm; all other parameters as in Table 4.1.

The theoretical calculation closely resembles the experimental findings. The SN2 potential shifts in the negative direction as the CO concentration is lowered. Although the mean field model can only be expected to reproduce qualitative trends due to the above discussed strong simplifications, the SN2 potential is recovered nearly quantitatively: When varying the CO concentration between a CO saturated solution and the lowest concentration that still supports bistability (1%) the SN2 point drops from about 810 to slightly below 600 mV, i.e. by more than 200 mV. This favourably compares with experiments in which a drop from about 850 mV to 650 mV was found in 0.5 M $HClO_4$ (*cf.* Figure 5.11). This shows that despite the reported sensitive dependence of the reaction rate on the surface morphology and the nature of anions, the drastic reduction of the SN2 potential with a decreasing CO concentration is already captured by modelling the competition between CO and OH adsorption in a simple mean field model. Furthermore, these results show that it is the SN2 potential which is the relevant potential for the determination of the most negative potential at which CO electrooxidation can proceed for a given electrode|electrolyte interface, not the potential at which the CO electrooxidation sets in when sweeping the potential positive.

To capture the effect of (bi)sulphate adsorption seems to be more difficult: First of all, we should note that there is still a controversy whether the adsorbing species is sulphate or bisulphate. The different arguments are summarized in [3] and [170]. Here, this question is of minor importance, and we continue denoting the adsorbing species as

(bi)sulphate, indicating that both forms might be adsorbed. In the potential region interesting in our context (bi)sulphate is known to form a $\sqrt{3} \times \sqrt{7}$ adlayer structure in sulphuric acid electrolytes [171, 172]. Two models were suggested to rationalize the adlayer structure; the first one implies a bi(sulphate) coverage of 0.4 ML [173] the latter one [174], which is favoured in the more recent literature, results in a coverage of 0.2 ML. The (bi)sulphate ions bind with three oxygen atoms to the Pt surface, such that one anion would occupy three Pt sites and hydronium ions are incorporated between the (bi)sulphate adsorbates and reduce the Coulomb repulsion between the anions. It seems to be plausible that the hydronium ions provide a source for 'activated water' for CO electrooxidation. If this were true, the adsorption of oxygenated species for CO electrooxidation would not independently compete for free surface sites with sulphate species, but sulphate would promote their adsorption. In addition, chronocoulometric measurements of the Gibbs excess of (bi)sulphate indicate that the anion coverage increases slightly in the potential range between 600 and 800 mV from a coverage of 0.33 ML to about 0.4 ML [175].

Against this background, it does not seem to be justified to model the behaviour with a mean field ansatz and differential equations. Nevertheless, we discuss in the following simulation predictions of the above discussed differential equations augmented by an equation describing the adsorption of anions according to

$$\mathrm{X}^{-2} + \mathrm{M} \rightarrow \mathrm{X}_a^{-2+n_x} + n_x \mathrm{e} \tag{5.2}$$

In above reaction X denotes an anion in solution, M a free surface site and X_a an adsorbed anion. Although lateral interactions between sulphate ions are believed to be minor [170], we assume here repulsive interactions among the anions to allow for a rather flat increase of anion coverage with potential. Thus, the rate of change of anion coverage was modelled by

$$\frac{d\theta_x}{dt} = k_{X,a} c_X (0.99 - \theta_X - \theta_{CO} - \theta_{OH}) e^{\frac{n_x \alpha FU}{RT} - g\theta_X} - k_{X,d} \theta_X e^{\frac{n_x (\alpha - 1) FU}{RT} + g\theta_X} \tag{5.3}$$

The parameters $k_{X,a}$, $k_{X,d}$, n_x, and g denote the anion adsorption and desorption rate constants, the (formal) number of electrons transferred during adsoption of one anion, and an interaction parameter describing repulsion between adsorbed species, respectively. The values of the parameters used in the simulations are given in table 5.1.

The rate equations for the CO and OH coverages and the equation for the current densities are modified to incorporate the anion coverage and currents associated with their ad- and desorption:

$$\frac{d\theta_{CO}}{dt} = k_{CO,a} c_s (0.99 - \theta_{CO} - \theta_{OH} - \theta_X) - k_r \theta_{OH} \theta_{CO} e^{\frac{\alpha FU}{RT}} \tag{5.4}$$

$$\frac{d\theta_{OH}}{dt} = k_{OH,a} (\theta_{OH}^m (1 - \theta_{CO} - \theta_X) - \theta_{OH}) e^{\frac{\alpha FU}{RT}} - k_{OH,d} \theta_{OH} \, e^{\frac{-(1-\alpha)FU}{RT}} - k_r \theta_{OH} \theta_{CO} \, e^{\frac{\alpha FU}{RT}} \tag{5.5}$$

$$\begin{aligned} i_F(x) = FS_{tot} [& k_{OH,a} (\theta_{OH}^m (1 - \theta_{CO} - \theta_X) - \theta_{OH}) e^{\frac{\alpha FU}{RT}} - k_{OH,d} \theta_{OH} \, e^{\frac{-(1-\alpha)FU}{RT}} \\ & + k_{X,a} n_X c_X (0.99 - \theta_X - \theta_{CO} - \theta_{OH}) e^{\frac{n_x \alpha FU}{RT} - g\theta_X} - k_{X,d} n_X \theta_X \, e^{\frac{n_x(\alpha-1)FU}{RT} + g\theta_X} \\ & + k_r \theta_{OH} \theta_{CO} e^{\frac{\alpha FU}{RT}}] \end{aligned} \tag{5.6}$$

Equation (4.30) in the section 4.5 describing the temporal change of the CO concentration in front of the electrode remains unaltered. The parameters used are given in tables 4.1 and 5.1. The results of the simulation are shown in Figure 5.13. The dashed curve in Figure 5.13a shows the predicted location of the SN2 potential in the presence of anions, the solid one the corresponding results without anions for comparison.

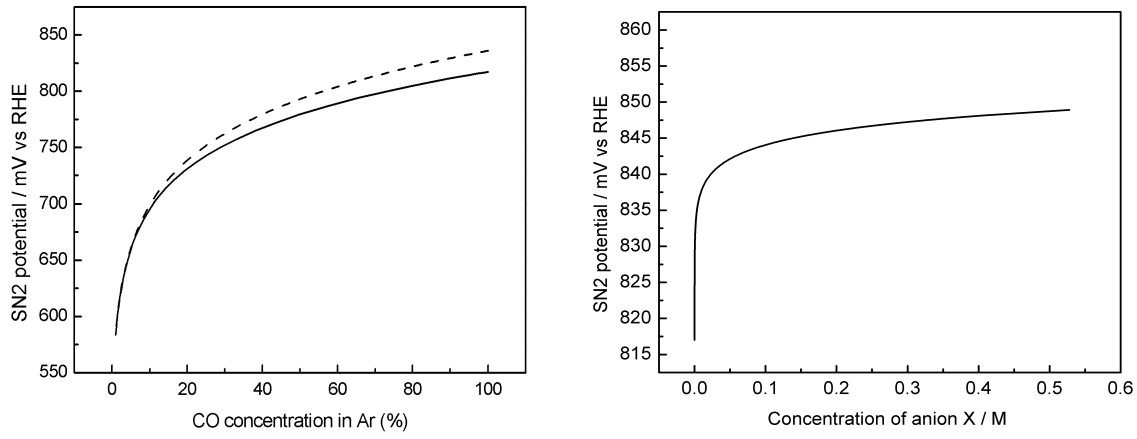

Figure 5.13: (a) Simulated location of the SN2 potential as a function of the CO concentration. Solid curve without inhibiting anions and dashed curve with 0.5 M inhibiting anions. (b) Simulated location of the SN2 potential as a function of the anion concentration in a CO saturated electrolyte.

Parameters	Value	Unit
$k_{X,a}$	10^6	$cm^3.mol^{-1}.s^{-1}$
$k_{X,d}$	$9x10^{10}$	s^{-1}
n_x	1.6	
g	20	

Table 5.1: Parameters of Eq. (5.3) used in the simulation

Thus, the model predicts that the presence of the inhibiting anions shifts the SN2 potential by about 20 mV in the positive direction in case of a CO saturated electrolyte, and as the CO concentration is lowered, the displacement decreases somewhat. The same trend was also found in the experiments (*cf.* Figure 5.11). Quantitatively, the experimental shift of the SN2 potential in the presence of inhibiting anions was about twice as large as in the simulations, which is, in view of the very rough model an astonishingly good agreement. In Figure 5.13b, the calculated variation of the SN2 potential with the concentration of the anions is depicted for a CO saturated electrolyte. Again, the qualitative behaviour found in the experiments is recovered (*cf.* Figure 5.12): With a decreasing anion concentration, the SN2 potential shifts negatively, and the shift with the concentration is small in a concentration range between about 10 and 100 %, but becomes steep for smaller anion concentrations. In other words, also in the model the presence of small amounts of anions shifts the SN2 potential already significantly. Thus, the essential points of the experimental findings are already captured using a mean field model, which allows for repulsive interaction of anions that otherwise compete for free surface sites with CO and OH.

In summary, both experimental and theoretical results confirm that the presence of the inhibiting anions influences the lowest potential at which CO can be oxidized; the presence of the inhibiting anions shifts the minimal potential in the positive direction. This underlines that the nature of the anions in the electrolyte has to be incorporated in any picture of CO electrooxidation, and has also to be considered in studies aiming at an improved CO tolerance of anodes in low temperature fuel cells.

Chapter 6: Strictly Potentiostatic Oscillations during Bulk CO Electrooxidation

6.1 Introduction

In the double layer, ionic species with a strongly bound solvation shell interact with the electrode surface primarily because of their electric charge, i.e. through Coulomb attraction or repulsion [170]. Consequently, the excess ion concentration at the surface at a given electrode potential is independent of the chemical nature of the ionic species. In contrast, weakly solvated ions can strip part of their solvation shell and form a direct chemical bond with the metal surface resulting in an ionic surface concentration that exceeds the one resulting from pure electrostatic interactions [176]. This phenomenon is known as specific adsorption. Specifically adsorbed anions can influence the electrochemical reactivity of a metal electrode in several ways:

(a) They may take part in the electrode reaction.

(b) They can block a reaction site, and consequently, reduce the reaction rate.

(c) They can alter the potential distribution in the double layer affecting the kinetics of electrochemical reactions [161].

The impact of weakly adsorbed anions, such as sulphate, on CO bulk electrooxidation was already discussed in the previous chapter. In this chapter, the influence of strongly adsorbing anions is investigated.

The influence of different anions on electrooxidation rates of small organic molecules is an active field of research. In the course of such studies, an unusual anion effect was reported by Schell and coworkers [177-179]. These authors observed a remarkable enhancement in the electrooxidation rate of formic acid [177, 178] and of methanol [179] when replacing a small amount of a $HClO_4$ base electrolyte with HBF_4. They offer

an intriguing explanation for the enhancement effect, which could be described as the anionic counterpart to the metal-promoted oxide formation at low potentials. In aqueous solutions, BF_4^- is in equilibrium with BF_3OH^- ions, which in turn can, directly or indirectly be adsorbed on the electrode negative to the onset of electrooxidation of chemisorbed water. Schell et al. suggest that the OH-group of adsorbed BF_3OH^- reacts with adsorbed CO, keeping thus the electrode reactive for the direct electrooxidation of formic acid or methanol at potentials at which it is poisoned by CO in a BF_4^- free electrolyte. Motivated by these experiments, we conducted investigations on CO electrooxidation on Pt in the presence of BF_4^-, which are described in this chapter. As will be shown, BF_4^- induces oscillations during CO electrooxidation. In the course of these studies, evidence was obtained that the current oscillations are induced by the adsorption of BF_4^- onto free surface sites, which are then not available anymore for CO electrooxidation. If this active site blocking hypothesis is true, CO electrooxidation should also exhibit oscillations in the presence of other inhibiting anions, such as halide ions.

Markovic et al. [180] found a strong inhibiting effect of Cl^- on the rate of methanol electrooxidation on both Pt(111) and Pt(100). Zolfaghari et al. [181, 182] reported that chloride and bromide ions are adsorbed competitively with hydroxide (or other oxygenated species stemming from water oxidation) on Pt in H_2SO_4. The competitive adsorption of halides and oxygenated species during oxide formation on Pt was reported by Conway and coworkers [112, 183-185]. Perez et al. [186] report that chloride inhibits CO electrooxidation on Pt and Hall et al. [187] found that hydrogen peroxide electrooxidation on Pt was inhibited by chloride ions. In a study of CO electrooxidation on Pt by Lopez Cudero et al. [188] the possibility of the formation of a mixed CO-chloride adlayer was discarded.

We thus also studied the effect of Cl^- and Br^- on the dynamics of CO electrooxidation, and, as described below, we found wide parameter ranges in which again the current was oscillatory. The results of the experiments with tetrafluoroborate and halide anions are described in section 6.3. In section 6.4, a model is presented that reproduces the experimental findings and thus allows to identify those steps of the reaction dynamics that are essential for the oscillatory instability. In section 6.5, the results are summarized. The following section gives a brief description of the experiments.

6.2 Experiments

The WE was a polycrystalline or single crystalline platinum disk electrode. Prior to the measurements with CO, the cleanliness of the WE was checked by recording a CV in Ar saturated electrolyte; the electrolyte was purged with Ar for at least 30 minutes before the CV was measured, and during this time the potential was scanned between 10 mV and 1270 mV for the polycrystalline electrode and between 100 mV and 200 mV for single crystal electrodes. The first reading of the CO electrooxidation current was taken approximately 25 minutes after switching to CO bubbling to guarantee the saturation of the electrolyte with CO. The pre-treatment for the polycrystalline and single crystalline electrodes is described in chapter 2.

6.3 Experimental Results

Here, we describe first the results obtained with a polycrystalline Pt electrode in the presence of BF_4^-, Cl^-, Br^-, and I^- ions. For each type of anion, the dynamics obtained in H_2SO_4 and $HClO_4$ base electrolyte is compared. Subsequently, results of experiments using three different single crystal orientations in a chloride containing H_2SO_4 electrolyte are presented.

6.3.1 Inhibiting effect of BF_4^- anions

Figure 6.1 shows cyclic voltammograms of Pt in CO-saturated 0.5 M H_2SO_4 containing different amounts of BF_4^- ions. The cyclic voltammograms were obtained at a scan rate of 50 mV/s. The solid curve was obtained in a pure supporting electrolyte. The dashed, dotted and dot-dashed curves in electrolytes containing 5, 10, and 20 mM HBF_4, respectively. The CVs exhibit a hysteresis between a reactive and a poisoned state in a certain potential interval negative to the ignition peak, which stems from the bistability that was already discussed in the previous chapters. The quantitative potential value, at which the transition from the reactive to the CO-covered low-current state occurs, depends on the BF_4^- concentration: the higher the BF_4^- concentration, the more positive is the transition from the reactive branch to the poisoned branch on the negative scan. In other words, the hysteresis becomes smaller and is shifted towards more positive potentials with increasing HBF_4 concentration.

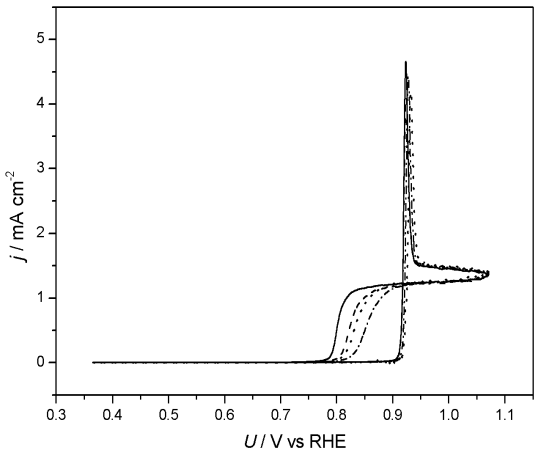

Figure 6.1: Cyclic voltammograms of a rotating Pt disk electrode in CO saturated 0.5 M H_2SO_4 solution containing 0 (solid curve), 5 mM (dashed curve), 10 mM (dotted curve) and 20 mM (dash-dotted curve) HBF_4; scan rate: 50 mV/s; rotation rate: 1200 rpm.

6.3.2 Current oscillations with BF_4^- anions

When reducing the scan rate, the CVs showed a most remarkable difference to the CVs at higher scan rate; the current exhibited oscillatory behaviour in a small potential region around the ignition potential. The oscillations sustained when fixing the applied voltage within a potential window of a few mV positive to the ignition potential. An example of the onset of oscillations in 0.5 M H_2SO_4 supporting electrolyte is shown in Figure 6.2a. Figure 6.2b displays a portion of the current time series after transients decayed. The oscillations were fairly regular and periodic. They disappeared when the rotation of the electrode was stopped.

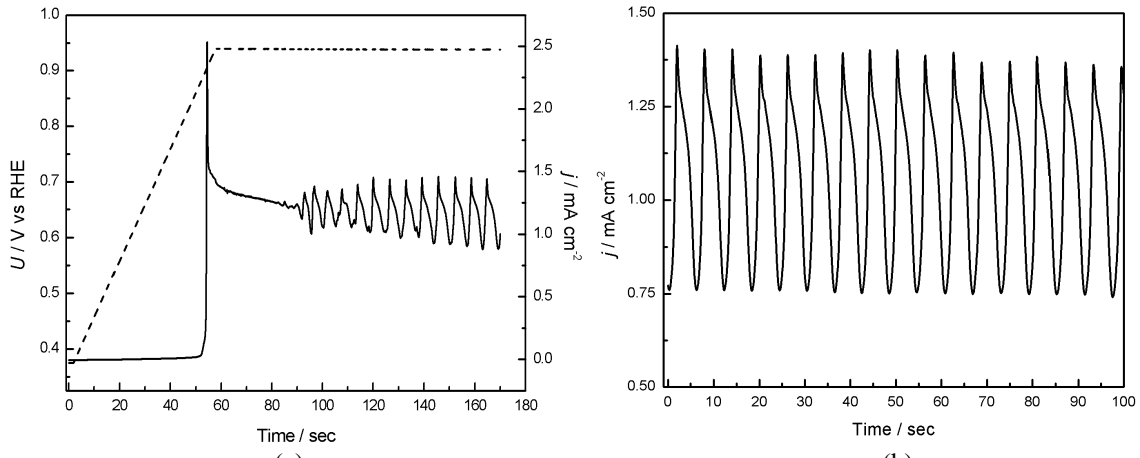

Figure 6.2: Current oscillations in CO saturated 0.5 M H_2SO_4 + 10 mM HBF_4. (a) Current-time (solid curve) and applied voltage time (dashed curve) plots showing the onset of oscillations after sweeping the applied voltage to 940 mV with 10 mV/s. (b) Current time series at U = 940 mV after the decay of transients. Rotation rate: 1200 rpm.

Also in a 0.5 M $HClO_4$ supporting electrolyte, current oscillations developed in a small potential window just positive to the ignition potential. However, in this case, the oscillations were never regular. Instead, they had a characteristic base period but apparently, randomly varying amplitudes and a higher frequency noise-like signal superimposed (Figure 6.3). These irregularities occurred only in the oscillatory region, strongly suggesting that they were intrinsic to the dynamics rather than caused by instrumental or other types of 'external' noise.

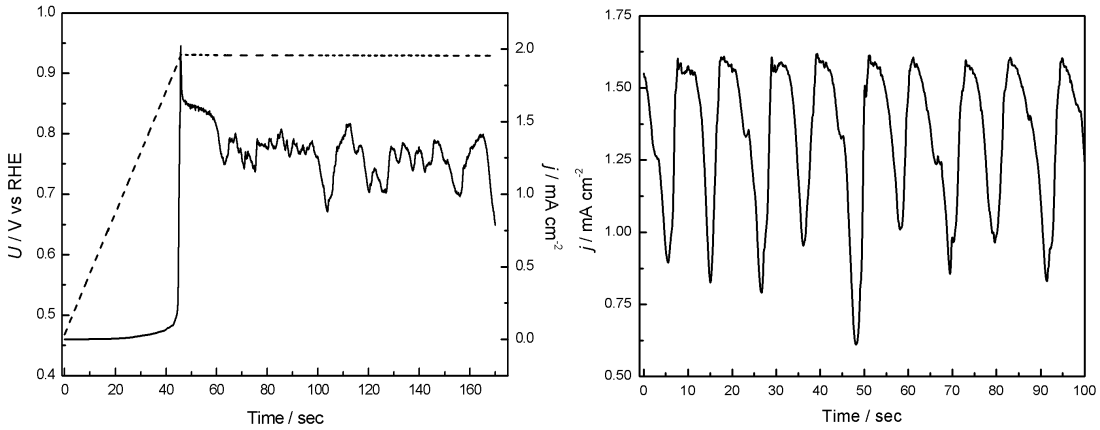

Figure 6.3: Current oscillations in CO saturated 0.5 M $HClO_4$ + 10 mM HBF_4. (a) Current-time (solid curve) and voltage time (dashed curve) plots showing the onset of oscillations after sweeping the voltage to 931 mV with 10 mV/s. (b) Current time series at U = 931 mV after the decay of transients. Rotation rate: 1200 rpm.

When repeating the experiments in 0.5 M HBF_4, sustained oscillations could not be obtained. Instead, a series of 'ignition peaks' with strongly decreasing amplitude was found, as can be seen in Figure 6.4.

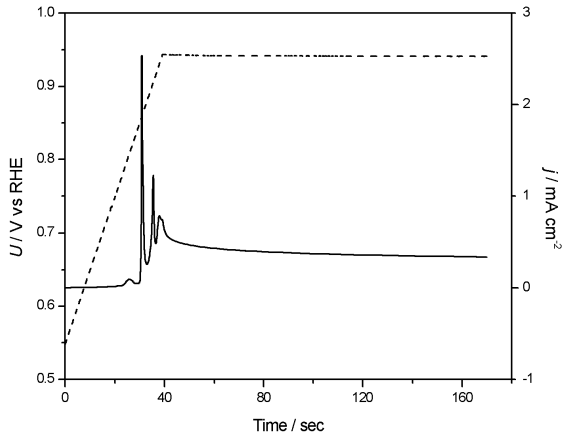

Figure 6.4: Current-time (solid curve) and voltage time (dashed curve) plots of CO electrooxidation on a rotating Pt electrode in CO saturated 0.5 M HBF_4 after sweeping the voltage to 941 mV with 10 mV/s. Rotation rate: 1200 rpm.

6.3.3 Current oscillations with chloride

Since the CVs shown above in Figure 6.1 strongly suggest that BF_4^- anions inhibit CO electrooxidation, it appeared worthwhile to test whether strong anion adsorption is sufficient to induce oscillations. If this is the case, oscillations should be independent of the chemical nature of the anions and also observable with different strongly adsorbing anions. Therefore, chloride was used in place of HBF_4. Figure 6.5a and Figure 6.5b show that also Cl^- can induce current oscillations during bulk CO electrooxidation. In this example, the Cl^- concentration was 10^{-6} M.

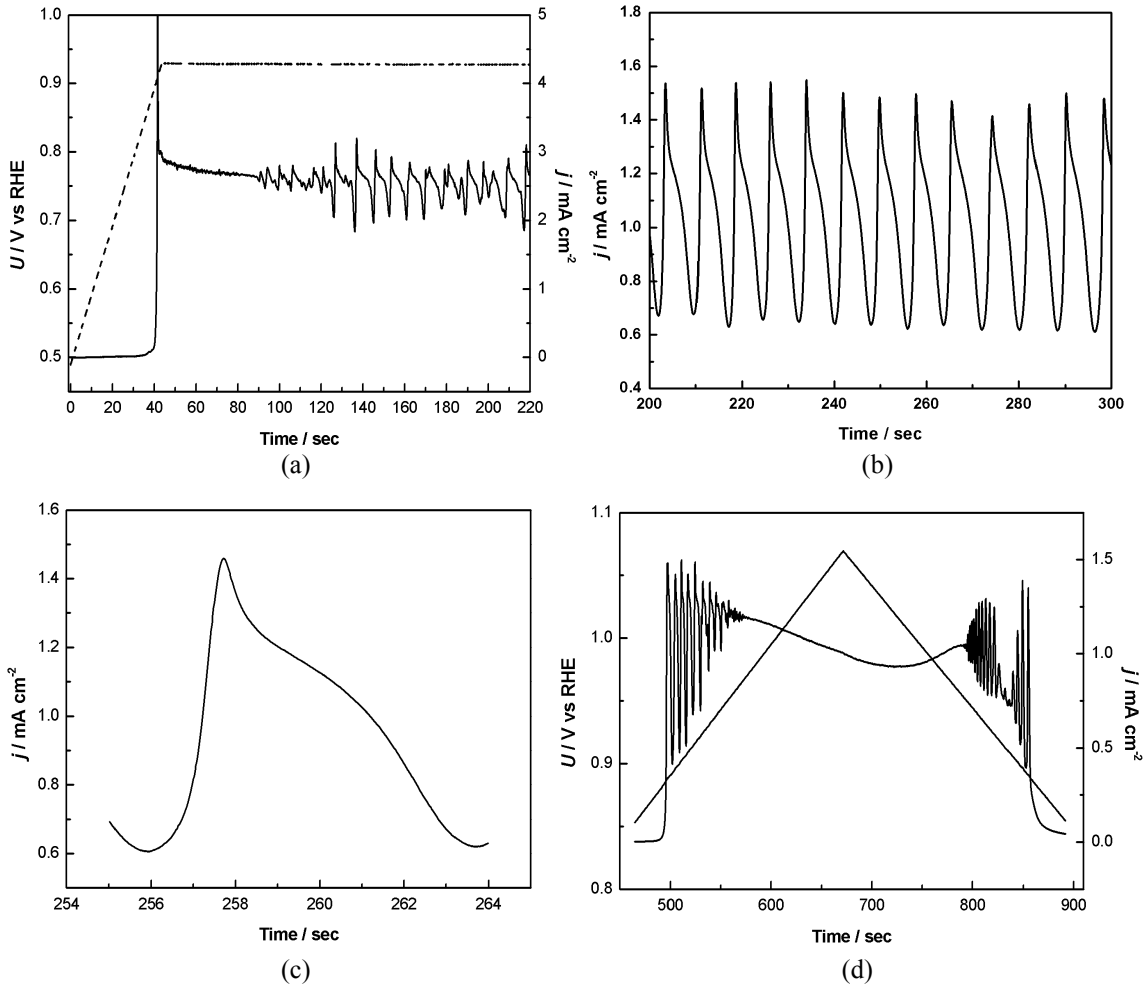

Figure 6.5: Current oscillations in CO saturated 0.5 M H_2SO_4 + 10^{-6} M HCl; (a) Current-time (solid curve) and voltage time (dashed curve) plots showing the onset of oscillations; (b) Current time series at U = 940 mV (c) Magnification of one oscillation cycle (d) Current and voltage time trace. The voltage was scanned with 1 mV/s, the current exhibits oscillatory behaviour within a voltage range of about 130 mV. Rotation rate: 1200 rpm.

The form of the oscillations is depicted on an enlarged time scale in Figure 6.5c. Just as in the case of BF_4^-, an oscillation is characterized by a short rise time and a long decay

time. The period of the oscillations in 10^{-6} M HCl was about 9 sec. The oscillations were fairly regular and the lower value of the current was much above zero, which indicates that the electrooxidation rate of CO remains significant even in the current minimum of the oscillations. Figure 6.5d shows the current time trace during a slow voltage scan (1 mV/s). The oscillations appeared during the forward as well as the reverse scan in a potential window of about 130 mV.

With concentrated H_2SO_4 as base electrolyte regular current oscillations were found in the presence of both HBF_4 and HCl. But, as reported above with a BF_4^-, the oscillations were always irregular when using perchloric acid as supporting electrolyte. Therefore, also experiments with Cl^- as inhibiting anions and $HClO_4$ as base electrolyte were conducted and again, only irregular oscillations were obtained (Figure 6.6). This strongly suggests that the irregularity of the oscillations found with $HClO_4$ is independent of the chemical nature of the inhibiting anions but is linked to properties of the perchlorate anions.

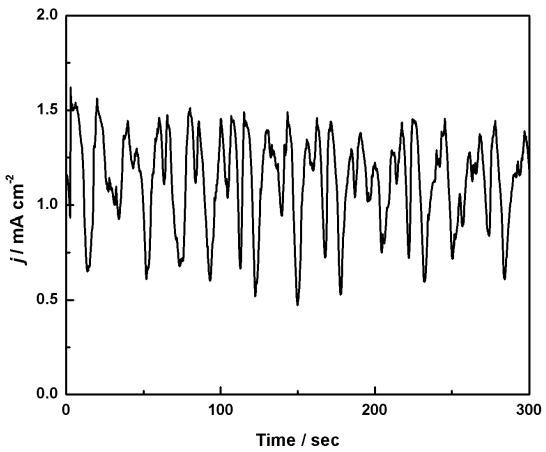

Figure 6.6: Current time series of a Pt disk electrode in CO saturated 0.5 M $HClO_4$ + 10^{-6} M HCl solution at U = 931 mV. Rotation rate: 1200 rpm.

In the next set of experiments, the influence of the Cl^- concentration on the dynamic behaviour was investigated. When increasing the Cl^- concentration the oscillations remained simple periodic in a certain voltage interval but the oscillation period decreased and the amplitude increased. Typical oscillations found with 10^{-5} M Cl^- are depicted in Figure 6.7a. The oscillations have now similar small rise and decay times. The shorter decay time is a direct consequence of the increased chloride concentration, since the time to reach the same level of total coverage is shorter at higher anion concentration. The decrease of the average CO electrooxidation current indicates higher

mean chloride coverage, as chloride blocks active sites. As above, the current does not go down to zero. At this higher Cl^- concentration the voltage interval, at which regular oscillations occur, was proceeded by a voltage range in which irregular transient oscillations with spike like bursts occurred (Figure 6.7(b)). Here the mean current was low in comparison to the mean current during the regular oscillations. However, during a spike the current sometimes attained a value that was much larger than the maximum value of the regular oscillations. The spikes appeared in random time intervals.

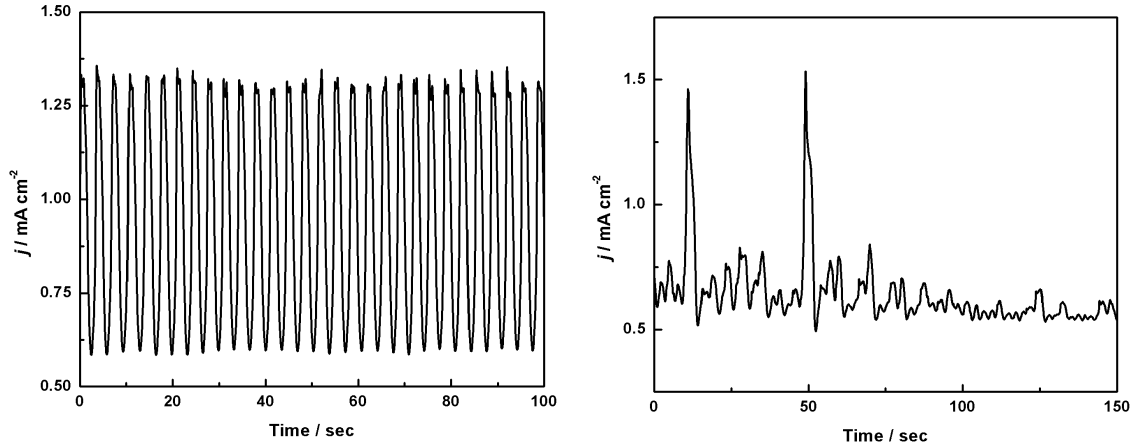

Figure 6.7: Current time series of a Pt disk electrode in CO saturated 10^{-5} M HCl + 0.5 M H_2SO_4 solution at (a) U = 955 mV (b) U = 936 mV. Rotation rate: 1200 rpm.

When increasing the Cl^- concentration further to 10^{-4} M, no sustained oscillations could be obtained anymore. Rather the CO electrooxidation current remained most of the time low but exhibited spike like burst as depicted in Figure 6.8. Again, the current spikes appeared randomly.

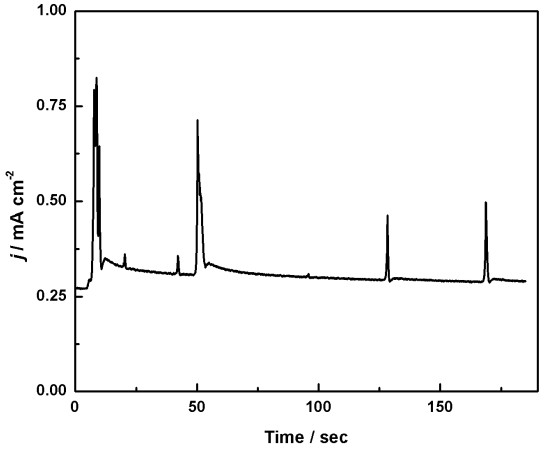

Figure 6.8: Current time series of a Pt disk electrode in CO saturated 10^{-4} M HCl + 0.5 M H_2SO_4 solution at U = 955 mV. Rotation rate: 1200 rpm.

This behaviour is similar to the one found in high concentrated HBF_4 (*cf.* Figure 6.4). At the low concentration limit, oscillations were still observed with 10^{-7} M HCl in 0.5 M H_2SO_4. An example is shown in Figure 6.9.

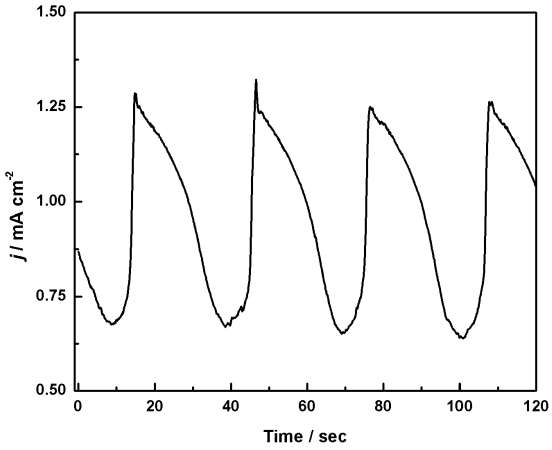

Figure 6.9: Current time series of a Pt disk electrode in CO saturated 0.5 M H_2SO_4 + 10^{-7} M HCl solution at U = 911 mV. Rotation rate: 1200 rpm.

The period of the oscillations was 30 sec and thus much larger than with the higher Cl^- concentrations. Otherwise, the oscillations were, as in the case of 10^{-6} M HCl asymmetric, i.e. they exhibited a short rise time, a slow current decrease; and the amplitude did not go down to zero. The slow current decrease supports the conjecture that its time is determined by the rate of anion adsorption. The occurrence of the oscillations at this low Cl^- concentration opens a new possibility to determine any trace of chloride in an electrolyte.

At lower as well as higher voltages the regular oscillations were encompassed by irregular ones. In general, at lower potentials, the mean current was lower, but the time series exhibited spike like bursts in irregular intervals to current densities that often exceeded the maximum current densities observed at higher voltages as depicted in Figure 6.10a. Leaving the voltage interval in which regular oscillations appeared at the positive end first irregular behaviour with a beat like character appeared (Figure 6.10b), then the mean amplitude decreased and the current exhibited apparently random variations, which look more like small fluctuations (Figure 6.10c). At still higher potential, a stationary current was observed again.

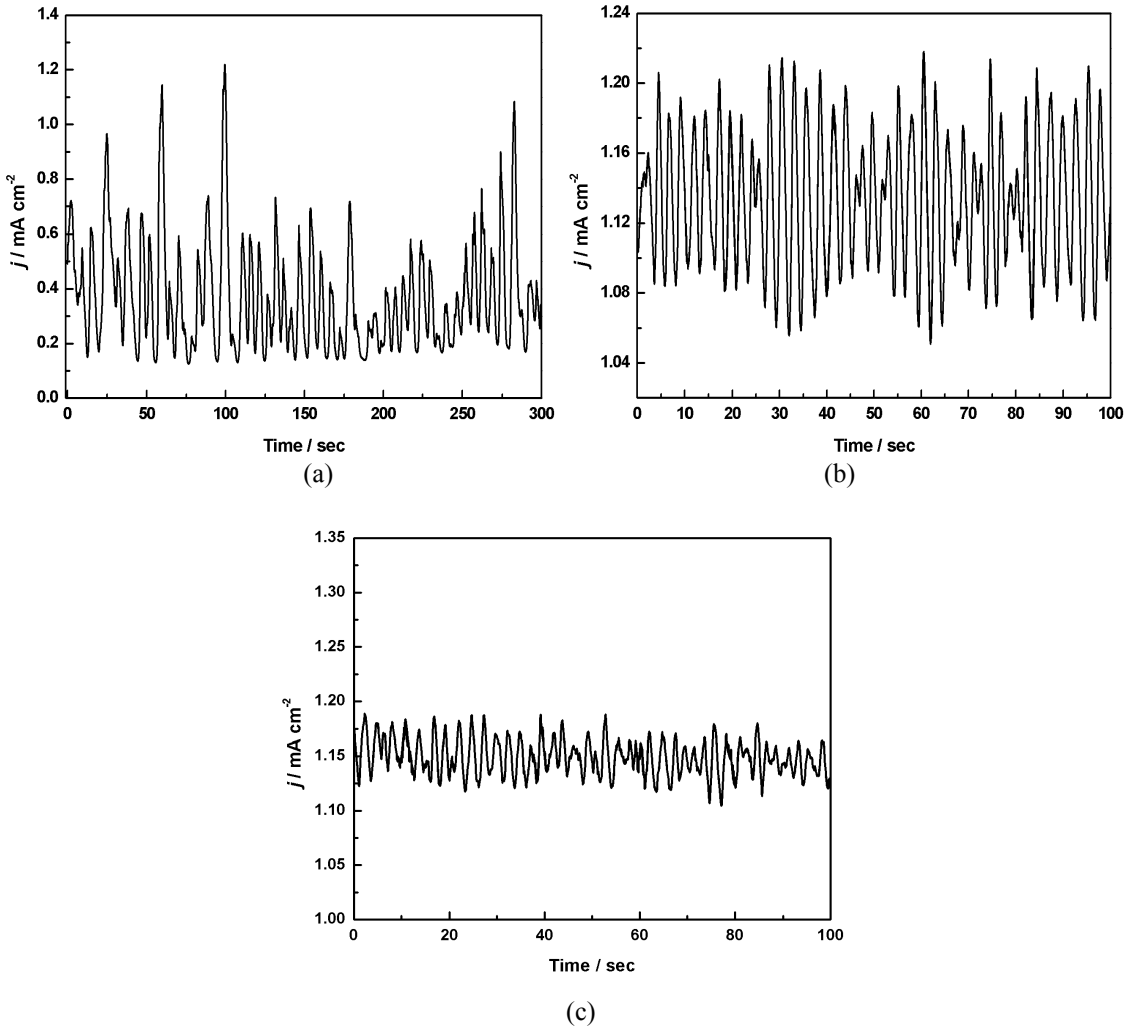

Figure 6.10: Current time series of a platinum disk electrode in CO saturated 0.5 M H_2SO_4 solution with various concentration of HCl, (a) with 10^{-5} M HCl, U = 890 mV (b) with 10^{-5} M HCl, U = 910 mV (c) 10^{-6} M HCl, U = 920 mV. Rotation rate: 1200 rpm.

The results of the effect of the chloride concentration on the oscillatory behaviour are summarized in Figure 6.11, which shows an experimental two-parameter phase diagram in the Cl^- concentration - applied voltage parameter plane. Each experimental point in the figure is marked by a dot. The region shaded in red indicates the region in which irregular long term dynamics was found; the blue colour region depicts the parameter range in which regular oscillations were observed, and the green shaded region denotes parameter values at which long transients with spike like bursts were found. In the white region, finally the current density was always stationary. An oscillatory current density was found for Cl^- concentrations varying by four orders of magnitude; and the potential range in which the oscillations were found was broadest at a Cl^- concentration of 10^{-6} M. It reduces to about 10 mV for a concentration of 10^{-7} M. At concentrations of 10^{-5}

and 10^{-4} M the current exhibited transients of spike like burst at irregular time intervals in a potential interval positive to the one in which sustained oscillations were obtained. With increasing Cl^- concentration, this potential range increased while the one in which sustained non-stationary behaviour occurred decreased. The average period of the regular oscillations increased with decreasing Cl^- concentration, as can be seen in Figure 6.12.

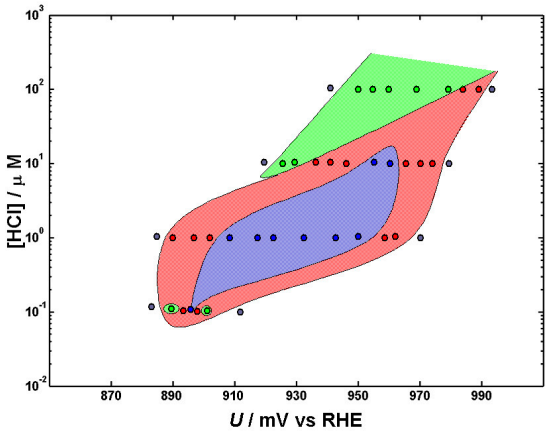

Figure 6.11: Region of regular oscillations (blue), irregular oscillations (red) and transient, burst oscillations (green) in the chloride concentration - applied voltage parameter plane; Base electrolyte: CO saturated 0.5 M H_2SO_4; rotation rate: 1200 rpm.

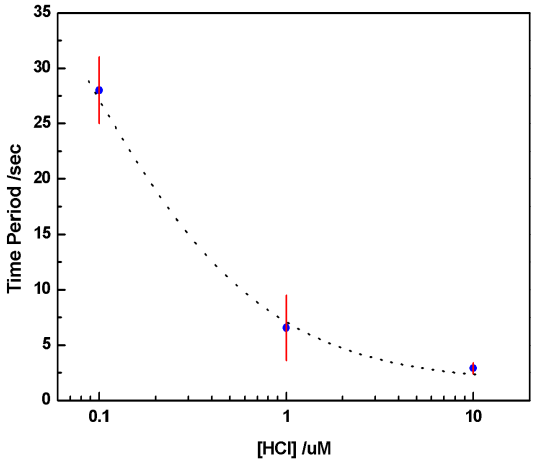

Figure 6.12: Period of the oscillations as a function of the chloride concentration. The dots represent the average value of the regular oscillations at the respective Cl^- concentration, the vertical lines indicate their variation with potential.

6.3.4 Effect of the rotation rate on the oscillatory behaviour

Also the rotation rate affected the oscillatory behaviour, as shown in Figures 6.13 and 6.14 for 10^{-5} M and 10^{-6} M Cl^-, respectively, and three different rotation values in each case.

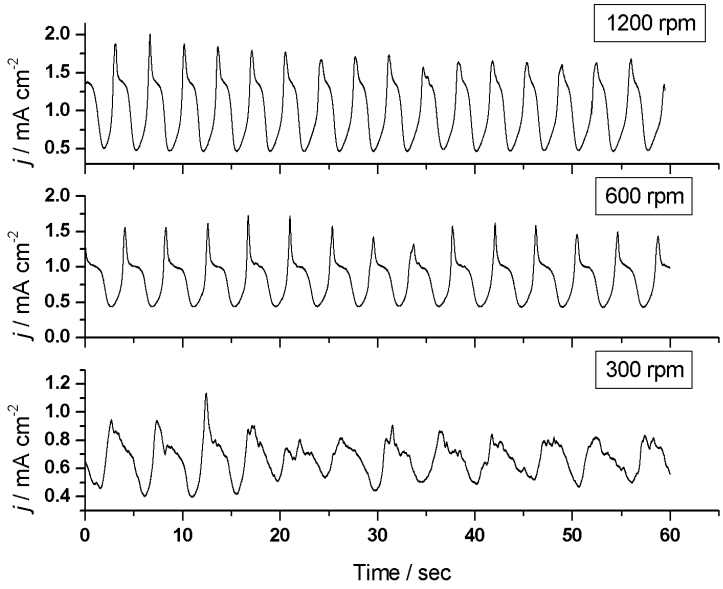

Figure 6.13: Current time series of a platinum disk electrode at different rotation rates in CO saturated 10^{-5} M HCl + 0.5 M H_2SO_4 solution at 940 mV.

As evident from the two figures, a decrease of the rotation rate leads to an increasing loss of synchronization of the oscillations as well as decreasing amplitude and increasing period. The last two trends seem to be a direct consequence of the reduced mass transfer rate of CO and Cl^- to the electrode; a reduced mass transfer leads, on the one hand to a slower poisoning of the electrode through CO and Cl^-, which in turn causes a longer period of the oscillations. On the other hand, it leads to a smaller diffusion limited current, which suggests that also the oscillation amplitudes become smaller. In contrast, there is no intuitive explanation for loss of correlation in time when lowering the rotation rate. The scenario does not follow one of the known routes to low dimensional chaos. Rather the strongly irregular temporal evolution of the current at 300 rpm, especially with 10^{-6} M Cl^-, resembles time series of systems exhibiting higher dimensional spatio-temporal chaos. This conjecture can, however only be proven with spatially resolved measurements, which would require a method with which the local concentration of CO, OH or Cl^- could be probed in-situ without interfering with the dynamics. Such a method is hitherto not available.

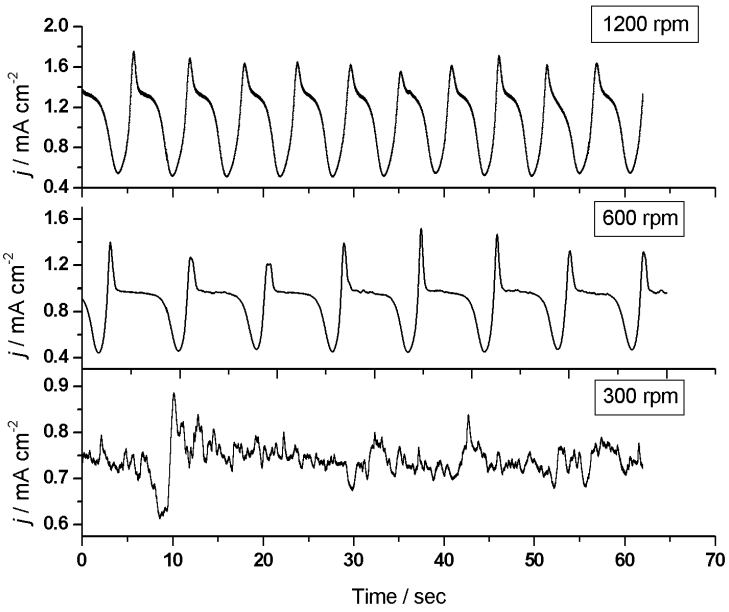

Figure 6.14: Current time series of a platinum disk electrode at different rotation rates in CO saturated 10^{-6} M HCl + 0.5 M H_2SO_4 solution at U = 910 mV.

The existence regions of regular and irregular oscillations in the rotation rate - applied voltage parameter plane are summarized in Figure 6.15. Again, the region, in which regular oscillations occurred, was surrounded by irregular oscillations. The existence region of oscillatory behaviour moved slightly towards negative potentials while the potential width in which unsteady behaviour was found remained approximately constant; the potential range for regular oscillations decreased with a decreasing rotation rate and disappeared at low rotation rates.

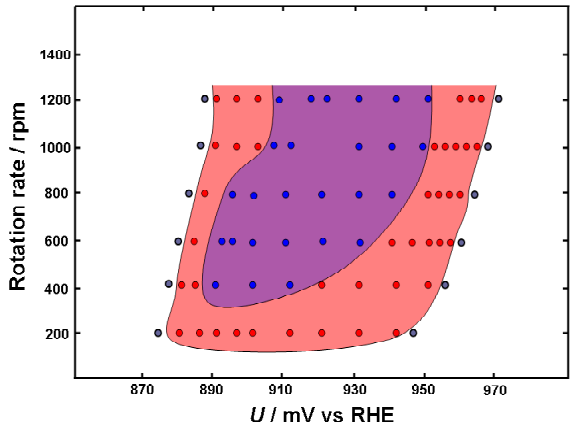

Figure 6.15: Region of regular (blue) and irregular (red) oscillations in the rotation rate - applied voltage parameter plane. Experimental condition: Base electrolyte: CO saturated 0.5 M H_2SO_4 + 10^{-6} M HCl.

6.3.5 Effect of the base electrolyte concentration on the oscillatory behaviour

The concentration of the supporting electrolyte is an important parameter for the dynamics of the electrochemical system since it determines the characteristic rate of spatial coupling through the electrolyte [90]. Hence, a change in the electrolyte concentration affects primarily the ratio of the characteristic rates of the local dynamics and the spatial coupling, which in turn is decisive for pattern formation. Roughly spoken, the larger the ratio, the more likely it is that patterns will form. Note that a change of the conductivity also alters the local dynamics somewhat. In this section, the impact of the H_2SO_4 concentration on the oscillations in presence of 10^{-6} M HCl is investigated. At low base electrolyte concentration, more precisely at H_2SO_4 concentration of 1, 5, and 10 mM, the oscillations were always irregular and had small amplitude. Typical time series are shown in Figure 6.16.

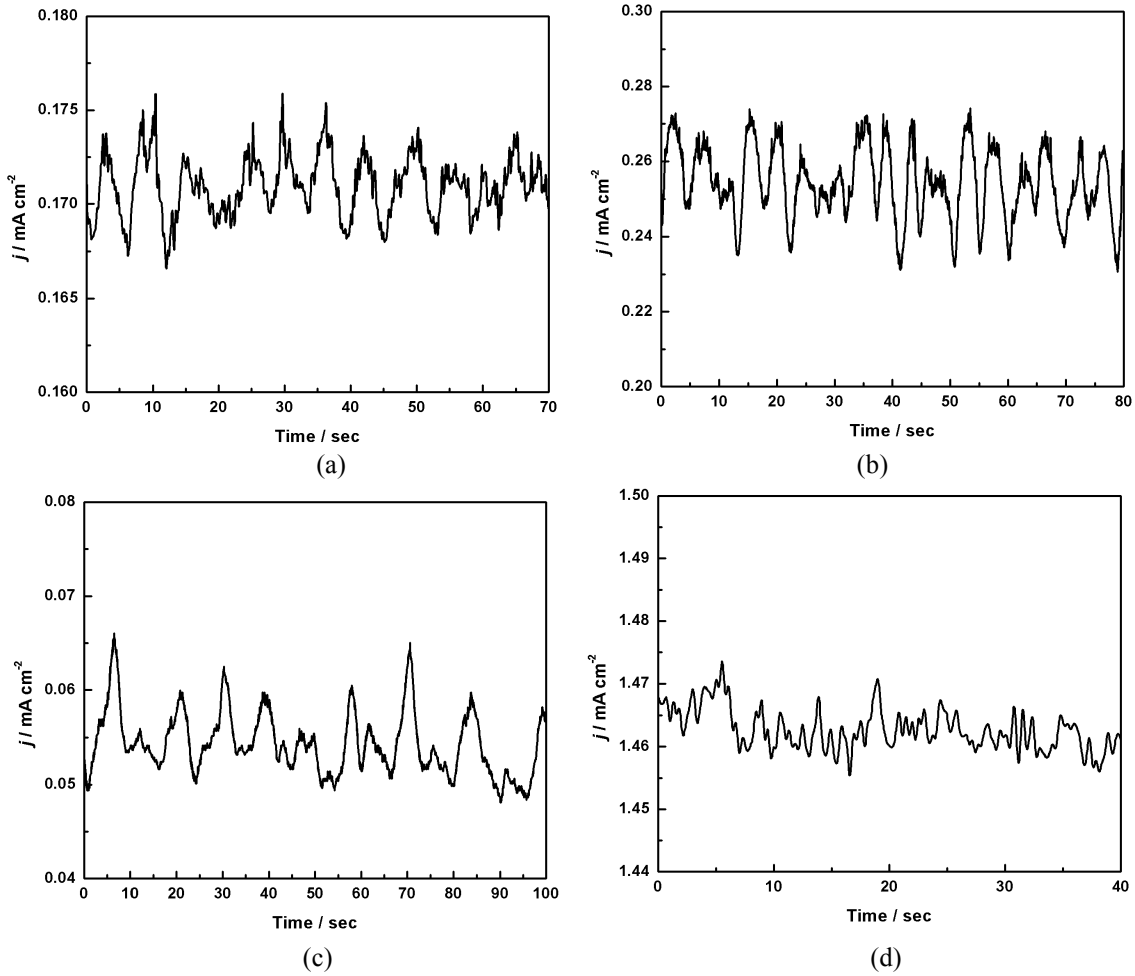

Figure 6.16: Current time series of a platinum disk electrode in CO saturated H_2SO_4 of different concentrations. (a) 1 mM H_2SO_4 (b) 5 mM H_2SO_4 (c) and (d) 10 mM H_2SO_4 Other parameters: rotation rate: 1200 rpm; HCl concentration: 10^{-6} M; (a) U = 978 mV (b) U = 917 mV (c) U = 890 mV (d) U = 1019 mV.

The mean amplitudes lay between 5 and 50 μA/cm^2 with a slight tendency to increase with increasing H_2SO_4 concentration. Moreover, at these low base electrolyte concentrations the potential window in which oscillations appeared was considerably larger at higher concentrations. This appears plausible since at low base electrolyte concentration the ohmic resistance and thus ohmic potential across the electrolyte is high. Using 50 mM H_2SO_4 as a base electrolyte, a variety of irregular oscillations appeared. At the lower end of the potential window i.e. at a potential of 901 mV, burst like current spikes occurred on a low current base level that exhibited small fluctuations. A corresponding time series is shown in Figure 6.17a. At somewhat higher potential these intermittently occurring spikes were replaced by sustained irregular oscillations of an amplitude of about 100 μA/cm^2 and an average period of 3 sec. Figure 6.17b depicts this oscillation type. When further increasing the potential, the irregular oscillations were interrupted by large amplitude current bursts, as shown in Figure 6.17c. Around a potential of 932 mV, though still irregular, the oscillations became more coherent; the oscillation minimum was split in a double peak structure while the maximum had small amplitude damped oscillations superimposed (see Figure 6.17d and 6.17e). Figure 6.17f shows a time series with a beat like structure. This behaviour persisted up to the high potential end of the oscillatory region, but the average amplitude decreased with increasing applied voltage (Figure 6.17g).

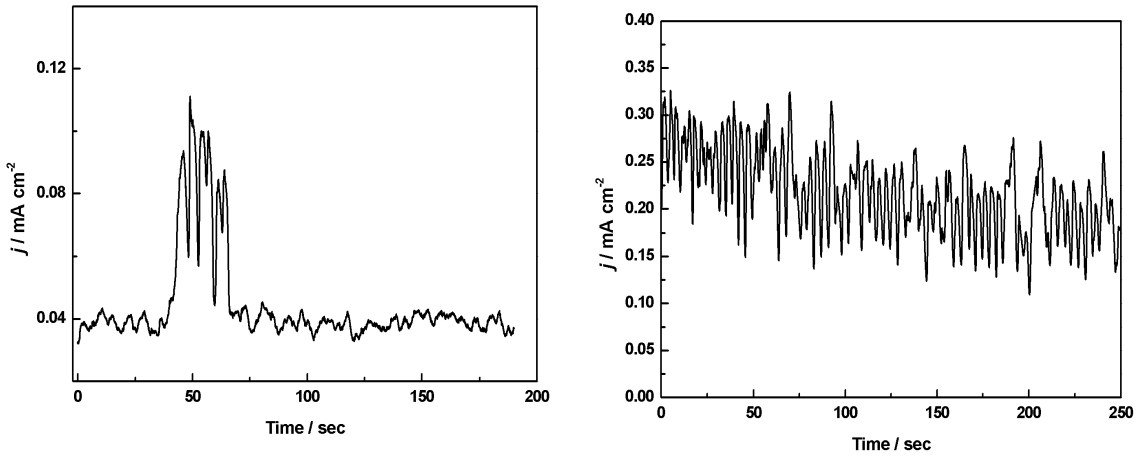

(a) (b)

Figure 6.17: Current time series of a platinum disk electrode in CO saturated 50 mM H_2SO_4 solution at various applied voltage. HCl concentration: 10^{-6} M HCl; rotation rate: 1200 rpm (a) U = 901 mV (b) U = 907 mV.

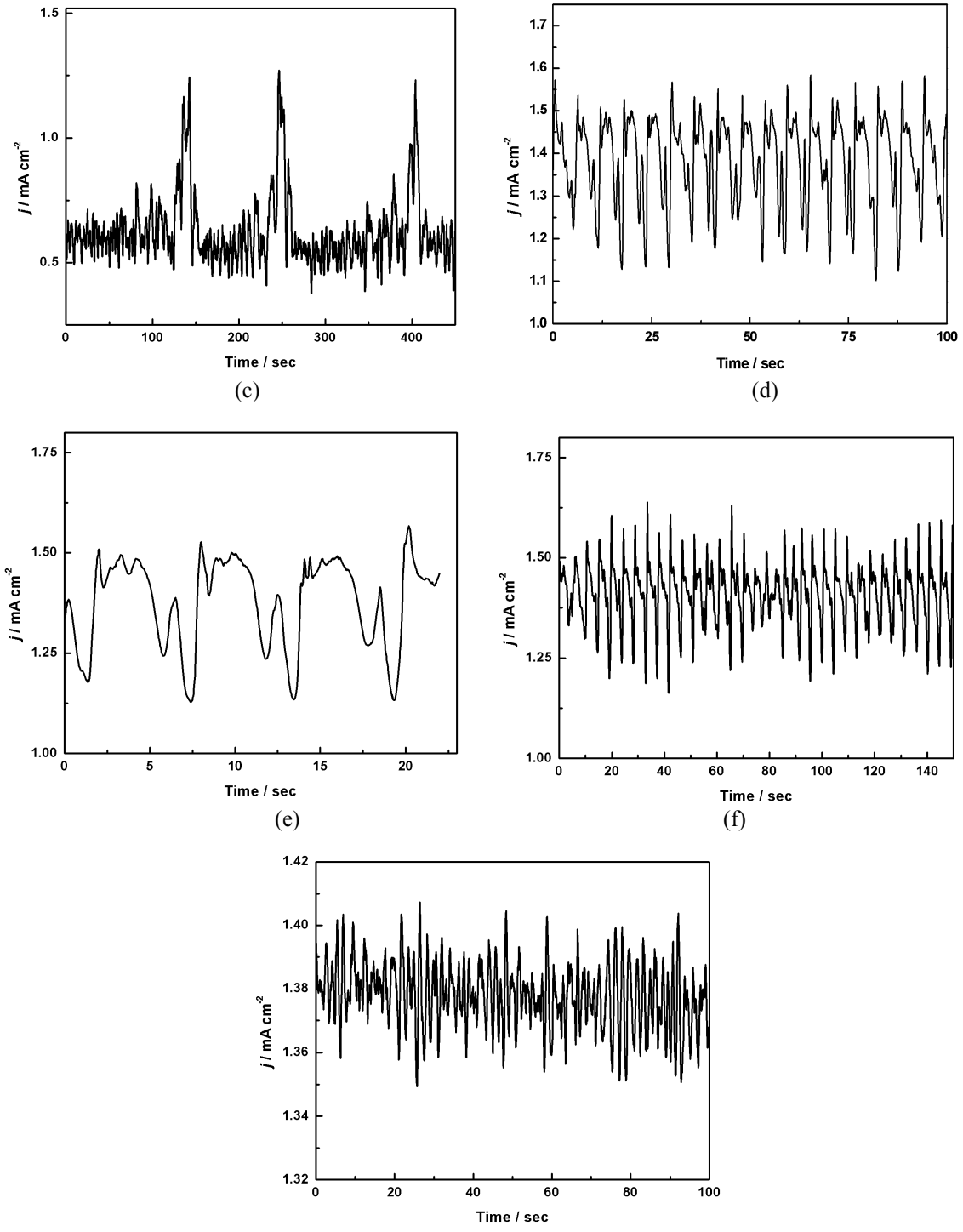

Figure 6.17(continued): Current time series of a platinum disk electrode in CO saturated 50 mM H_2SO_4 solution at various applied voltage; HCl concentration: 10^{-6} M HCl. Rotation rate: 1200 rpm (c) $U = 912$ mV (d) $U = 932$ mV (e) $U = 932$ mV (f) $U = 952$ mV (g) $U = 976$ mV.

With a sulphuric acid concentration of 100 mM regular oscillations appeared in a small potential window, which was surrounded by irregular oscillations on both sides. Figure 6.18 shows the irregular oscillations found at the low potential end. Again, when

entering the oscillatory interval from the low potential region, irregular, small amplitude oscillations were interrupted by current bursts (Figure 6.18a). An increase in potential first led to multiple bursts before more coherent oscillations with complex base patterns appeared (Figure 6.18c).

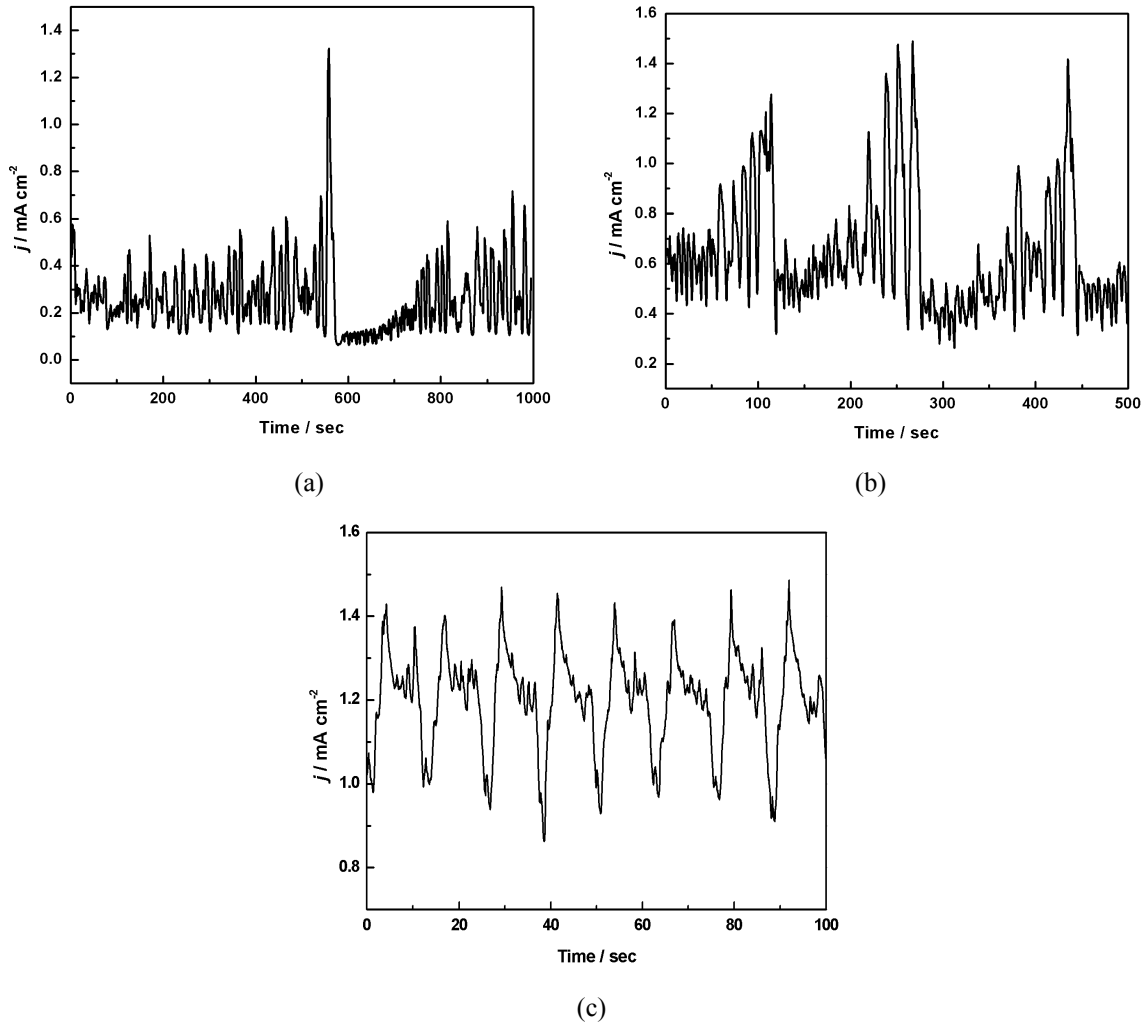

Figure 6.18: Current time series of a platinum disk electrode in CO saturated 0.1 M H_2SO_4 solution at various applied voltages; (a) U = 897 mV (b) U = 900 mV (c) U = 907 mV. HCl concentration: 10^{-6} M; rotation rate: 1200 rpm.

Figure 6.19 shows oscillations as found in the middle and at the high potential end of the oscillatory region. In 6.19a regular oscillations with a peculiar double hump structure, which were recorded at 917 mV, are shown. Figure 6.19b depicts fairly regular oscillations of simpler shape. As can be seen in Figure 6.19c their amplitude became modulated at higher potential, before at the upper end of the potential window the oscillations became again much less coherent and had a smaller mean amplitude.

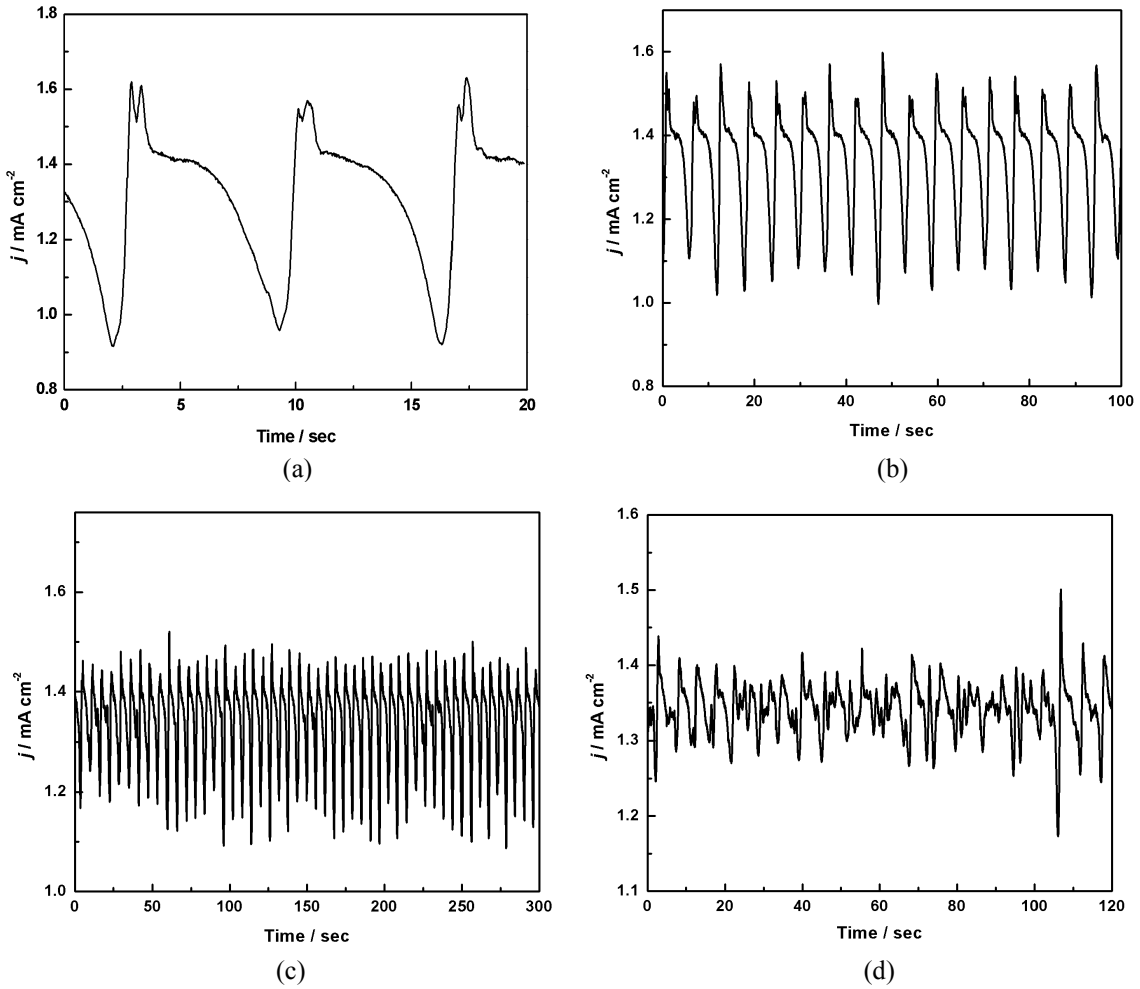

Figure 6.19: Current time series of a platinum disk electrode in CO saturated 0.1 M H_2SO_4 solution at various applied voltage; (a) U = 917 mV (b) U = 927 mV (c) U = 937 mV (d) U = 945 mV. HCl concentration: 10^{-6} M; rotation rate: 1200 rpm.

Figure 6.20 shows the regions in which (nearly) periodic and irregular oscillations were found in the H_2SO_4 concentration - applied voltage parameter plane. The region expands towards larger voltages for decreasing sulphuric acid concentration and for H_2SO_4 concentrations below 0.1 M only irregular oscillations were found. While the increasing width in potential with decreasing concentration of supporting electrolyte originates from the larger potential drop through the electrolyte with decreasing electrolyte concentration, we can only speculate about the origin of the second trend, namely the lack of regular oscillations at low sulphuric acid concentrations.

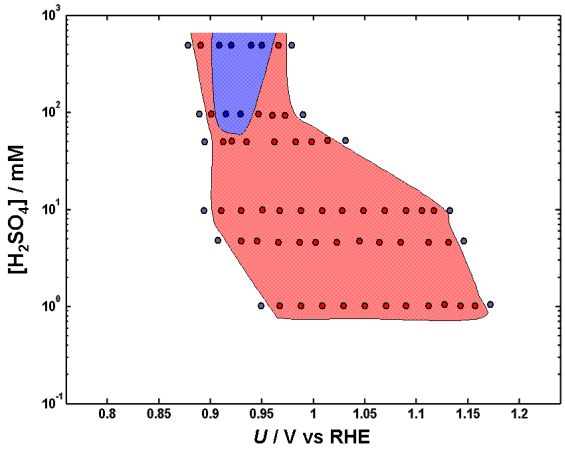

Figure 6.20: Oscillatory region in the H_2SO_4 concentration - applied voltage parameter plane. Blue region: regular oscillations. Red region: irregular oscillations. Remaining parameters: HCl concentration: 10^{-6} M; rotation rate: 1200 rpm.

At a low H_2SO_4 concentration the coverage of (bi)sulphate at a given double layer potential is smaller. Experiments with HBF_4 on the one hand and in $HClO_4$ electrolytes on the other hand showed a similar trend: regular oscillations were observed with BF_4^-, and thus strongly adsorbing anions, while in the weakly adsorbing perchlorate electrolyte regular oscillations were never observed. Thus, a possible hypothesis is that strongly adsorbing anions synchronize the oscillations. However, at the low electrolyte concentration also the spatial coupling between adjacent locations on the electrode surface becomes weaker, which promotes pattern formation and might induce spatio-temporally chaotic states. The best way to corroborate this hypothesis would be to perform spatially resolved measurements. However, as already mentioned above while the experiments for this thesis were done, there was no method available that would allow the in-situ imaging of potential or CO coverage patterns on the Pt electrode with a spatial resolution of a few 10 μm, which seems to be an upper bound of the necessary resolution considering the size of the used disk electrode of 5 mm diameter. In contrast, a simple test can be made that allows to discriminate between spatial coupling and anion adsorption induced changes in the dynamics, on the one side, and changes that are caused by a change of the local dynamics of the double layer potential, on the other side. The latter depends only on the total series resistance, irrespective of whether the resistance is due to an external resistor or it is due to low electrolyte conductivity. Hence, when working in a 0.5 M H_2SO_4 and inserting a series resistance, effects that are caused by migration coupling or by a changed anion adsorption should not occur. Corresponding experiments are described in the next section.

6.3.6 Impact of a series resistance

When increasing the ohmic resistance in series to the working electrode by inserting a resistor in the external circuit (between the working electrode and the potentiostat) instead of lowering the electrolyte resistance, the current time series at similar total resistance exhibited clear differences. An overview of the oscillatory behaviour for different values of the series resistance and two values of the applied voltage each is shown in Figures 6.21 and 6.22. Clearly, also for large series resistances nearly regular oscillations can be found. This is an important difference to the behaviour found at the low electrolyte concentration. However, the voltage interval in which regular oscillations existed was considerably smaller at high resistance than at low resistance.

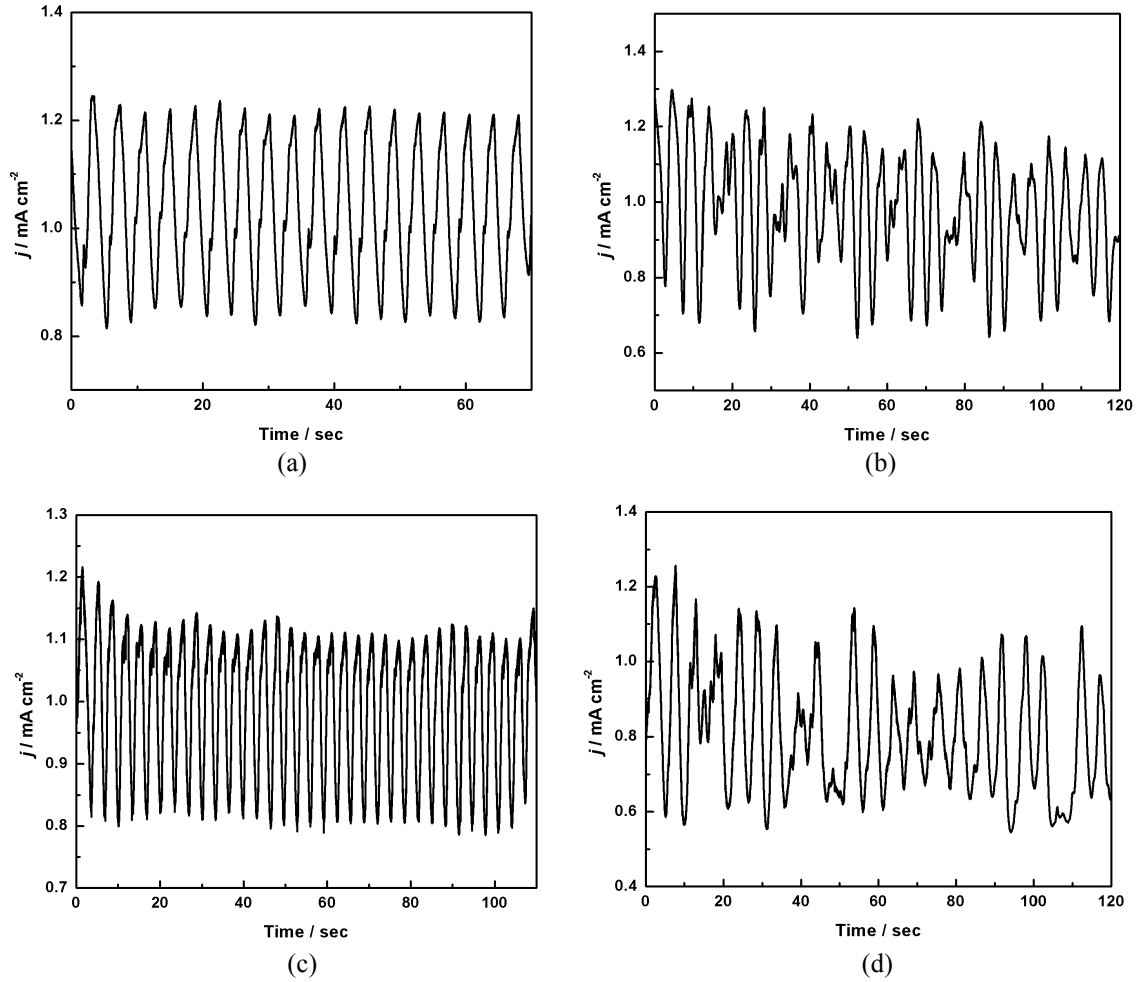

Figure 6.21: Current time series of a Pt disk electrode in CO saturated 0.5 M H_2SO_4 electrolyte for different series resistances and external voltages; Series resistance (a) and (b) R = 50 Ω; (c) and (d) R = 70 Ω. Applied voltage (a) U = 950 mV; (b) U = 930 mV; (c) U = 960 mV; (d) U = 920 mV; HCl concentration: 10^{-6} M; rotation rate: 1200 rpm.

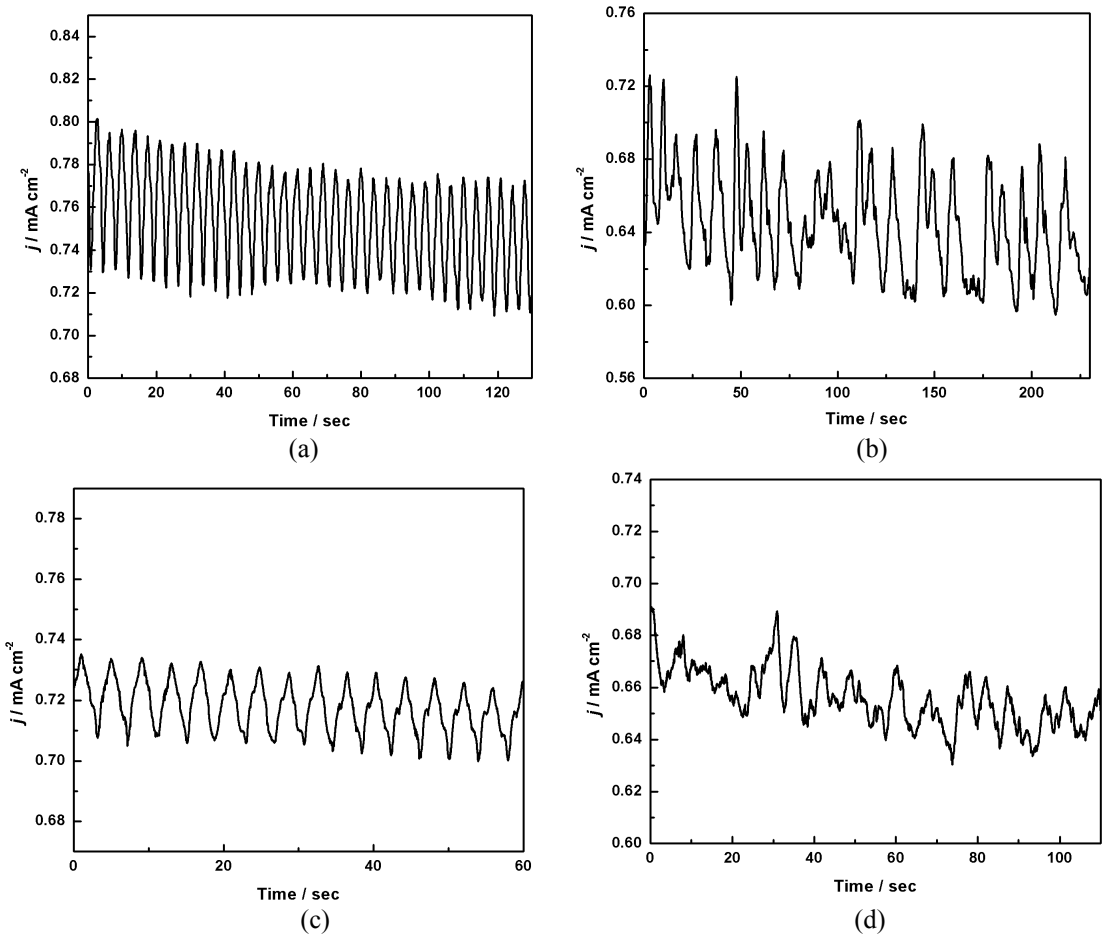

Figure 6.22: Current time series of a Pt disk electrode in CO saturated 0.5 M H_2SO_4 electrolyte for different series resistances and external voltages; At (a) and (b) R = 350 Ω; (c) and (d) R = 700 Ω; At (a) U = 1000 mV; (b) U = 970 mV; (c) U = 1050 mV; (d) U = 1030 mV; HCl concentration: 10^{-6} M; rotation rate: 1200 rpm.

A comparison of the total oscillatory region and the region of regular oscillations in the series resistance–external voltage parameter plane is shown in Figure 6.23.

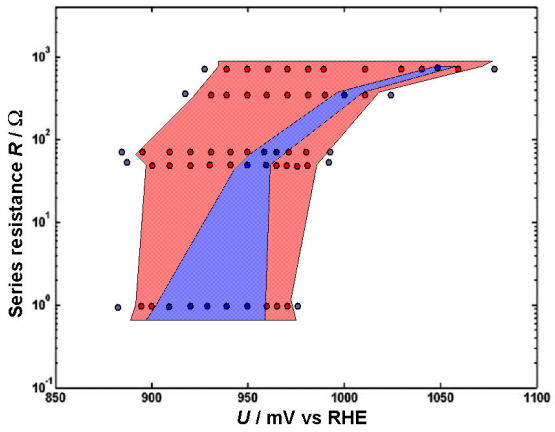

Figure 6.23: Oscillatory region in the series resistance - external voltage parameter plane. Blue region: regular oscillations. Red region: irregular oscillations. Remaining parameters: Base electrolyte: 0.5 M H_2SO_4; HCl concentration: 10^{-6} M; rotation rate: 1200 rpm.

6.3.7 Current oscillations with bromide and iodide

To further substantiate that CO electrooxidation on Pt in the presence of strongly adsorbing anions exhibits non-stationary oscillations further experiments were carried out with Br^- and I^-. Typical time series observed with 0.5 M H_2SO_4 and low Br^- concentrations are displayed in Figure 6.24.

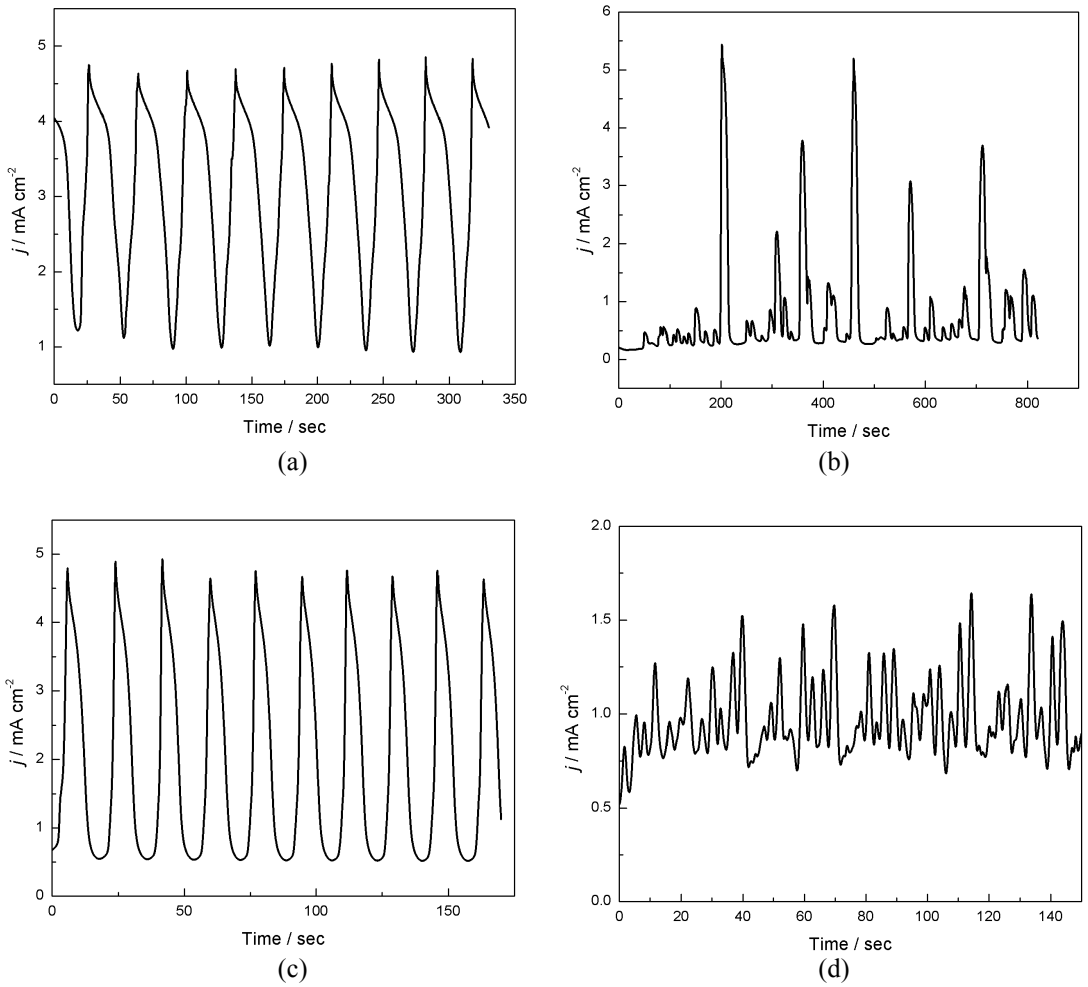

Figure 6.24: Current time series of a platinum disk electrode in CO saturated 0.5 M H_2SO_4 solution with various Br^- concentrations and applied voltages; (a) and (b) 10^{-7} M KBr; (c) and (d) 10^{-6} M KBr; At (a) U = 950 mV (b) U = 890 mV; (c) U = 960 mV (b) U = 990 mV. Rotation rate: 1200 rpm.

The upper row shows the dynamic behaviour for 10^{-7} M Br^-, the lower row for 10^{-6} M Br^-. Clearly, for both cases regular oscillations with amplitudes that were even larger than in the case of Cl^- were found as well as irregular ones. For the regular oscillations, the oscillation period exhibited the same trend as a function of the Br^- concentration that was already found for chloride. The lower the anion concentration the larger the period

indicating that the time scale of the falling flank was determined by the bromide adsorption rate. Contrary, the lengthening of the period arose from a slower decrease of the current density while the increasing current flank was nearly independent of the halide concentration. Furthermore, the potential range of the regular oscillations was again proceeded by a voltage interval in which aperiodic time series were observed, and as in the case of Cl^- irregular spike like current peaks appeared on a low current background (Figure 6.24b). At a higher Br^- concentration, irregular oscillations occurred also positive to the voltage interval of the regular oscillations (Figure 6.24d).

We have seen that with Cl^- or BF_4^- as inhibiting anions only irregular oscillations were observed with $HClO_4$ as a base electrolyte. Therefore, corresponding experiments were done with bromide and also here we did not succeed in establishing regular oscillations when using $HClO_4$ as a supporting electrolyte. Typical time series in two different Br^- concentrations are displayed in Figure 6.25.

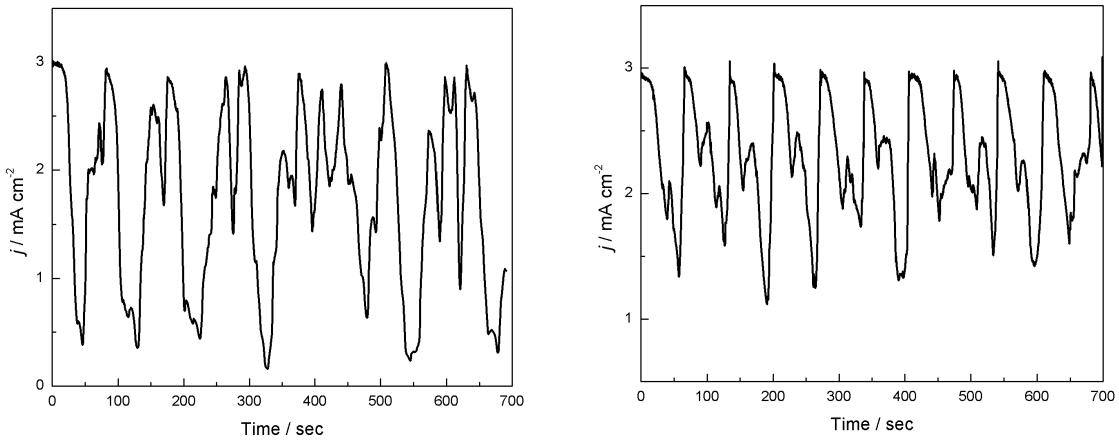

(a) (b)

Figure 6.25: Current time series of a platinum disk electrode in CO saturated 0.5 M $HClO_4$ solution with various Br^- concentration at U = 960 mV (a) 10^{-6} M KBr (b) 10^{-7} M KBr. Rotation rate: 1200 rpm.

When replacing Br^- by I^- oscillatory behaviour could not be established anymore (for I^- concentration between 10^{-7} M and 10^{-6} M). Instead, the ignition of the reaction was always followed by a gradually decrease of oxidation current to a minimal value where it remained. An example of a typical current trace in 10^{-7} M KI is shown in Figure 6.26.

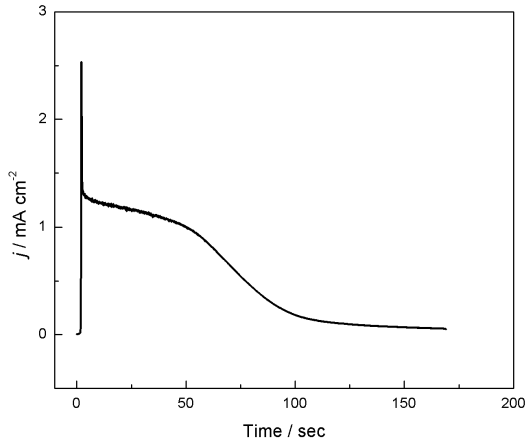

Figure 6.26: Current time series of a platinum disk electrode in CO saturated 0.5 M H_2SO_4 solution with 10^{-7} M KI at U = 920 mV. Rotation rate: 1200 rpm.

6.3.8 Current oscillations with Pt single crystal electrodes

As already discussed in chapter 5, anion adsorption depends strongly on the crystallographic orientation of the WE, suggesting that also the oscillatory behaviour should exhibit differences for different surface orientations. Therefore, experiments on the CO electrooxidation on the three low index Pt surfaces Pt(110), Pt(100), and Pt(111) were carried out under condition under which oscillations were found with polycrystalline Pt. More precisely the experiments were done in CO saturated 0.5 M H_2SO_4 base electrolyte to which 10^{-7} M HCl, 10^{-6} M HCl or 10^{-5} M HCl was added. The electrode rotation rate was 1200 rpm in all experiments.

6.3.8.1 Pt(110)

In the case of Pt(110) oscillations were found for 10^{-6} M and 10^{-5} M HCl while for 10^{-7} M HCl sustained oscillations could not be established. Figures 6.27a and 6.27b show typical current time series for 10^{-6} M and 10^{-5} M HCl. For both chloride concentrations only irregular oscillations occurred, the amplitudes taking on values up to 700 $\mu A/cm^2$, which is considerably smaller than the maximum amplitudes observed on a polycrystalline Pt electrode. Also the potential range in which the current exhibited non-stationary behaviour was smaller than for polycrystalline Pt, and for 10^{-5} M HCl it was larger than for 10^{-6} M HCl. This seemed to be correlated with the fact that the cyclic voltammogram (recorded with a scan rate of 5 mV/s) still showed a hysteresis for 10^{-6} M HCl with a low current and high current branch (Figure 6.27c). At stationary conditions, the oscillations occurred in the immediate neighbourhood of the ignition peak and were

centred around the high current state. For 10^{-5} M Cl^- the hysteresis with the two current levels was replaced by a potential region in which the current was oscillatory also in the cyclic voltammogram and the mean current density increased with increasing potential (Figure 6.27d).

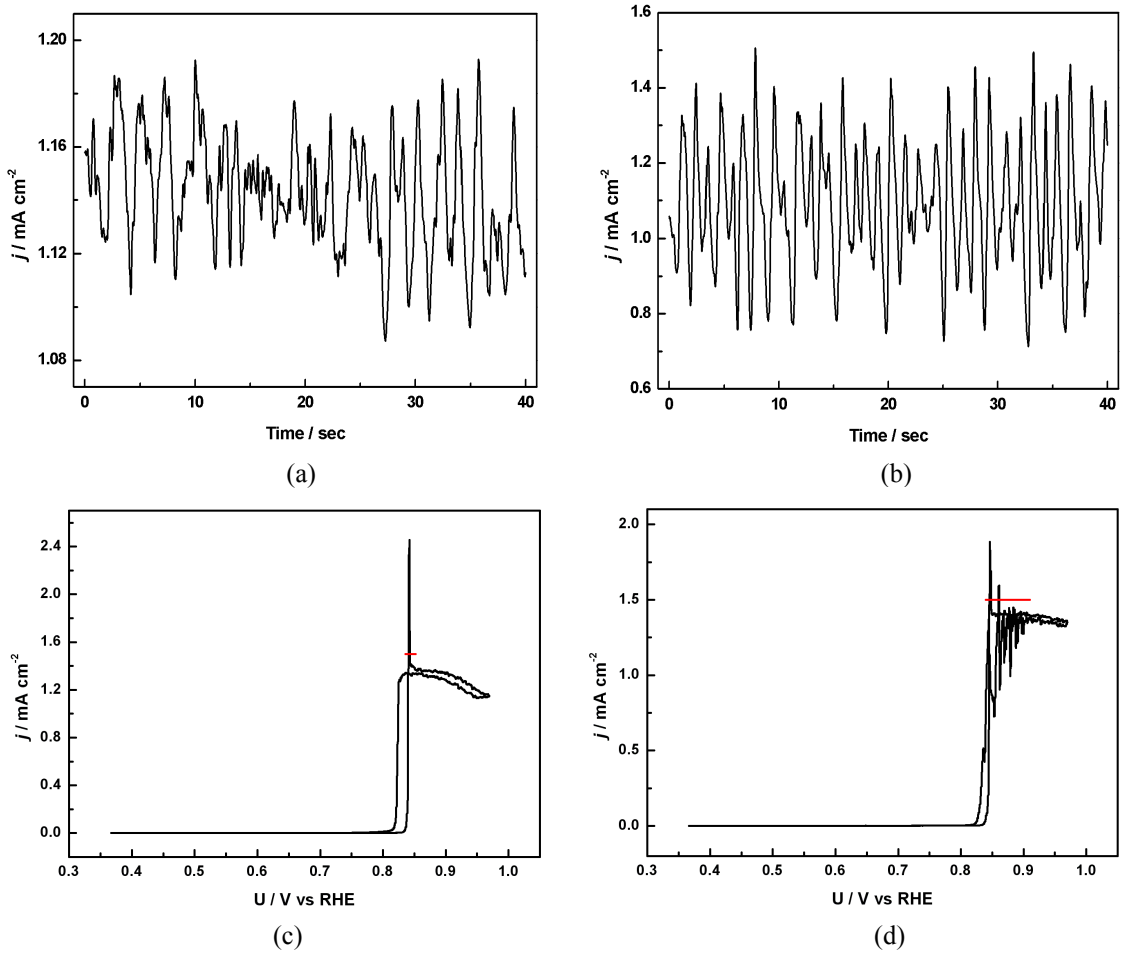

Figure 6.27: Current time series and cyclic voltammograms during CO electrooxidation on Pt(110) for different HCl concentrations; (a) and (c) 10^{-6} M HCl (b) and (d) 10^{-5} M HCl. Remaining parameters: base electrolyte: CO saturated 0.5 M H_2SO_4; rotation rate: 1200 rpm; (a) U = 850 mV (b) U = 840 mV; (c) and (d) scan rate: 5 mV/s; The red bar in (c) and (d) marks the potential window in which under stationary conditions oscillations were observed.

6.3.8.2 Pt(100)

In contrast to Pt(110), on Pt(100) oscillations appeared with all three tested Cl^- concentrations, i.e. with 10^{-7} M HCl, 10^{-6} M HCl, and 10^{-5} M HCl. Typical time series for the three concentrations are shown in Figure 6.28. Clearly, at low Cl^- concentration the oscillations differ from the previously described oscillations: Here, spike like current bursts occurred from a high current level towards low current density. On polycrystalline Pt, current spikes always occurred towards large current densities from a

low base current. While at 10^{-7} M HCl only such inverse spikes were observed (Figure 6.28a), at 10^{-6} M HCl these inverse spikes were preceded by irregular oscillations around on intermediate current density at low potentials (Figure 6.28b and Figure 6.28c). At 10^{-5} M HCl only the latter type irregular oscillations occurred (Figure 6.28d). Similarly to polycrystalline platinum, as the chloride concentration was increased the mean time period of the oscillations decreased.

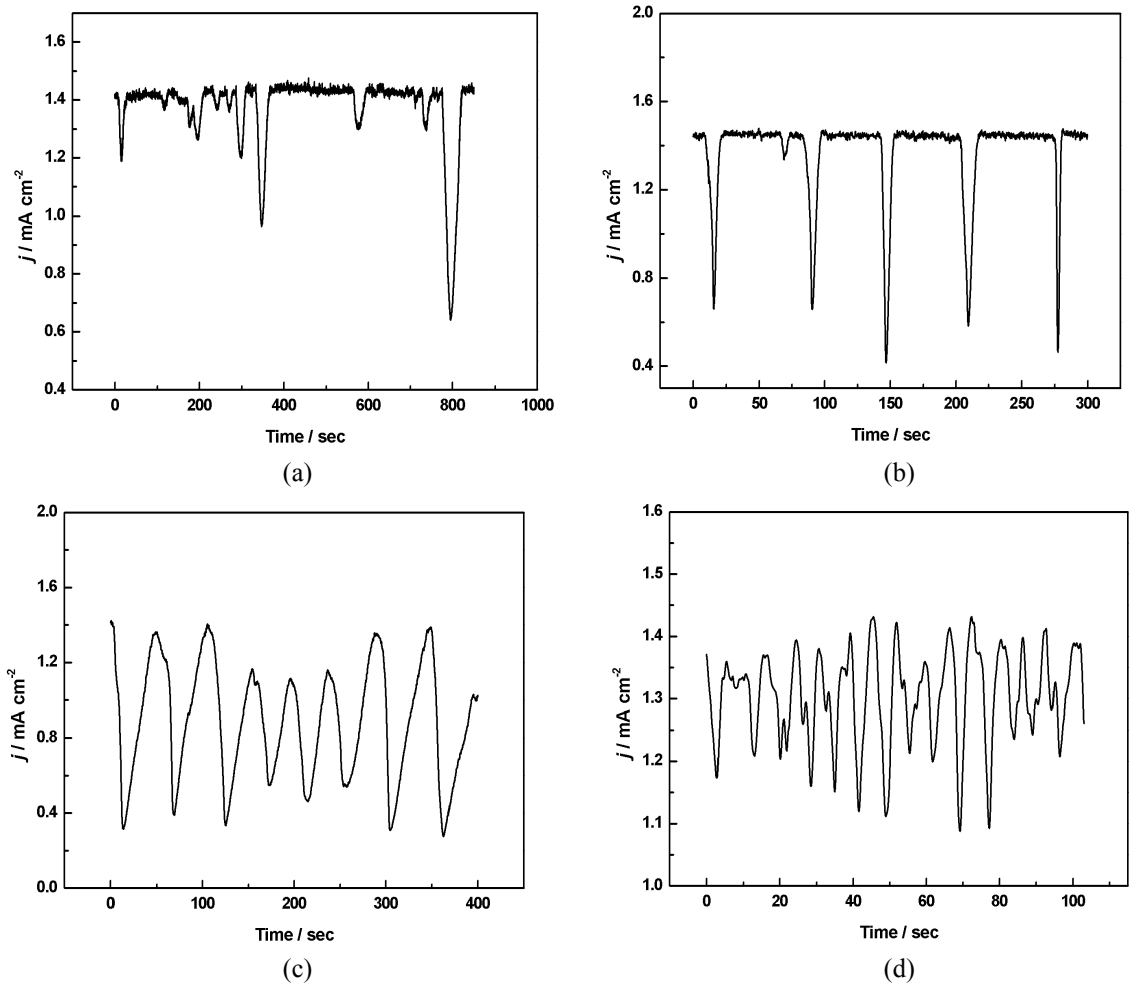

Figure 6.28: Current time series during CO electrooxidation on Pt(100) for different HCl concentrations; (a) 10^{-7} M HCl, (b) and (c) 10^{-6} M HCl, (d) 10^{-5} M HCl. Remaining parameters: base electrolyte: CO saturated 0.5 M H_2SO_4; rotation rate: 1200 rpm; (a) U = 900 mV, (b) U = 920 mV, (c) U = 900 mV, (d) U = 930 mV.

As can be seen in Figure 6.29 the different oscillatory character for the three different Cl^- concentrations is reflected in different cyclic voltammograms. The cyclic voltammograms exhibited a pronounced hysteresis between a poisoned and reactive state in the case of the two CVs with the lower Cl^- concentration, the hysteresis being somewhat narrower for 10^{-6} M HCl than for 10^{-7} M HCl. For the chosen sweep rate

oscillations cannot be discerned in the two CVs but a comparison with the time series obtained under the stationary condition (*cf.* Figure 6.28c, d) suggest that the high current branch was oscillatory and the oscillations coexist with a stable poisoned state. At 10^{-5} M HCl, the hysteresis was considerably smaller and oscillations were discernible on the high current branch, which did not exhibit a constant level but a falling average value.

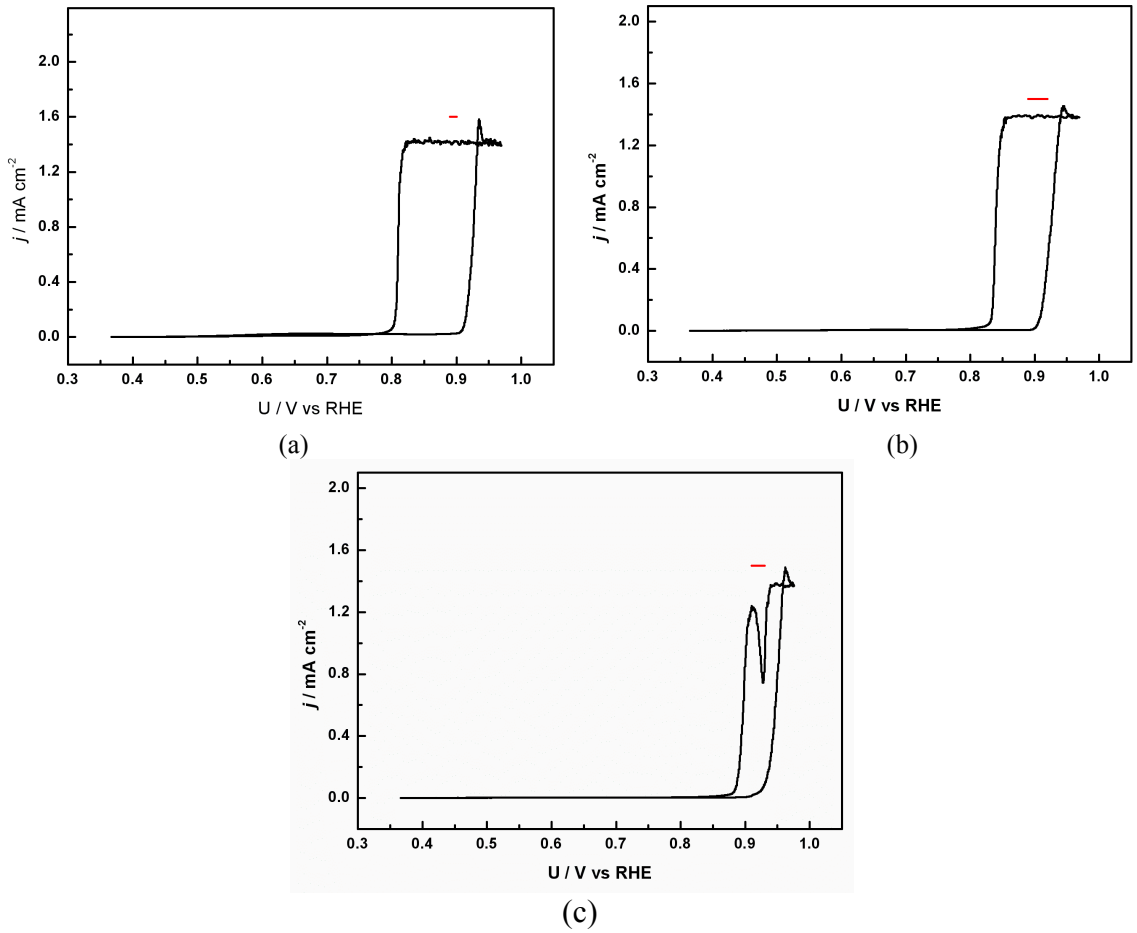

Figure 6.29: Cyclic voltammogram during CO electrooxidation on Pt(100) for different HCl concentration; (a) 10^{-7} M HCl, (b) 10^{-6} M HCl, (c) 10^{-5} M HCl. Remaining parameters: base electrolyte: CO saturated 0.5 M H_2SO_4; rotation rate: 1200 rpm; scan rate: 5 mV/s; The red bar in figure marks the potential window in which under stationary condition oscillations were observed.

6.3.8.3 Pt(111)

In the case of Pt(111), current time series recorded at a constant voltage exhibited always a strong decrease of the mean current density, even at Cl^- concentration as low as 10^{-7} M, and the long-term behaviour exhibited a vanishing current density. Yet, in a small potential window, this decay in the mean current was superimposed by fast, low

amplitude aperiodic oscillations for all three Cl^- concentrations (see the left column of 6.30).

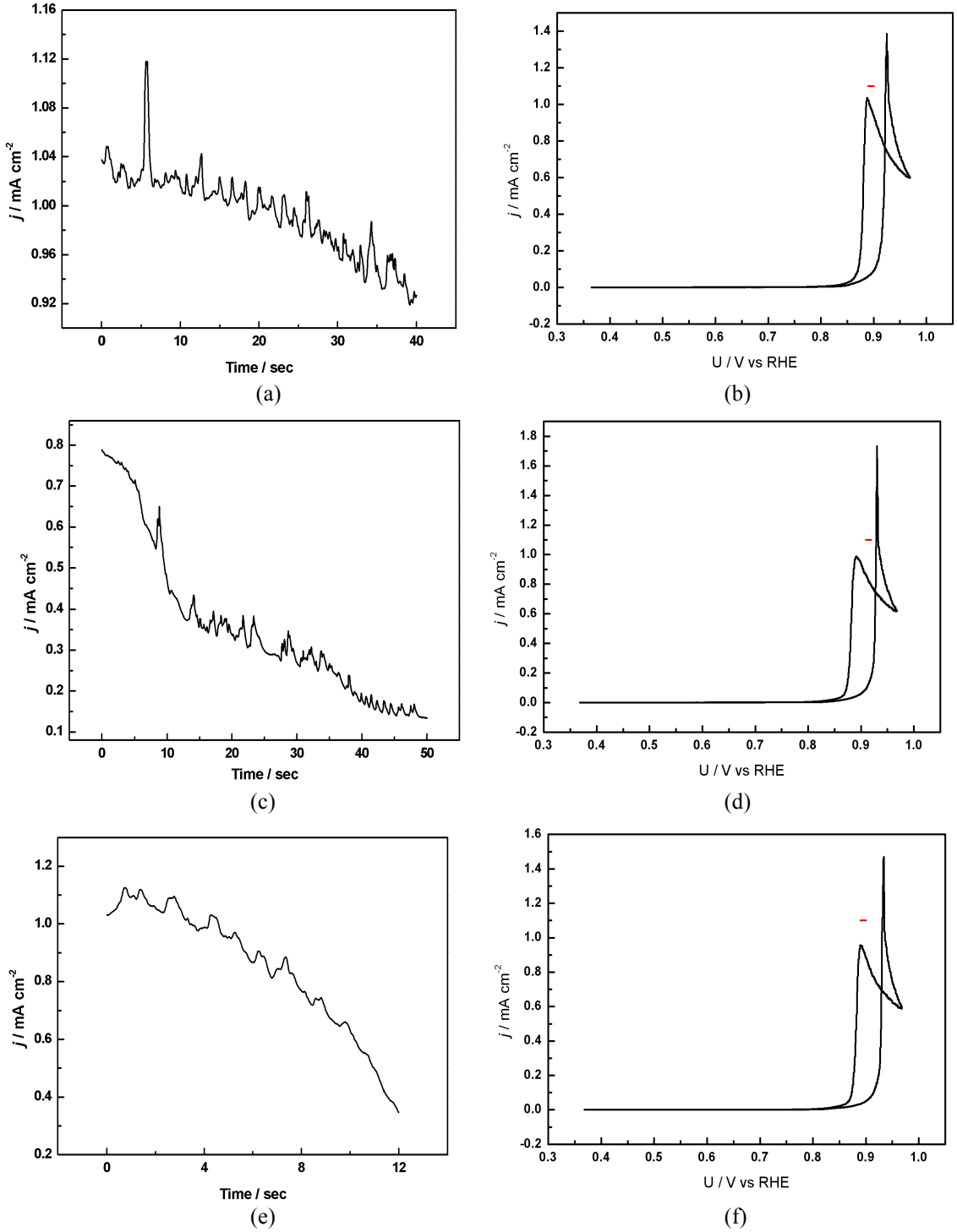

Figure 6.30: Current time series and cyclic voltammogram during CO electrooxidation on Pt(111) for different HCl concentration; (a) and (b) 10^{-7} M HCl, (c) and (d) 10^{-6} M HCl, and (e) and (f) 10^{-5} M HCl. Remaining parameters: base electrolyte: CO saturated 0.5 M H_2SO_4; rotation rate: 1200 rpm; (a) U = 900 mV, (c) U = 910 mV, (e) U = 895 mV; (b), (d) and (f) scan rate: 5 mV/s; The red bar in (b), (d) and (f) marks the potential window in which under stationary condition oscillations were observed.

The corresponding cyclic voltammograms, again recorded at a sweep rate of 5 mV/s, also exhibited a remarkable difference to those of the other two low indexed orientations: In the reactive state, the current density strongly decreased with increasing potential on the forward as well as on the backward sweep with a small hysteresis in the two scan directions. The difference of the cyclic voltammograms obtained for different Cl^- concentrations was marginal. This indicates that the potential dependence of the current density on the reactive branch stems from sulphate adsorption.

6.4 Model and simulation

In this section, we discuss a mean field model, which explains some of the experimental results.

6.4.1 Strictly potentiostatic oscillator

The simplest way to adopt the model for CO electrooxidation introduced in chapter 4 to the experimental conditions under which oscillations were found is to augment the reaction steps by the ad- and desorption of anions [45], whereby the only interaction among the anions and between anion and CO or OH is through the competition for free surface sites. Thus, we consider the following reaction steps.

$$CO_b \rightarrow CO_s \tag{6.1}$$

$$CO_s + M \rightarrow CO_{ad} \tag{6.2}$$

$$H_2O + M \leftrightarrow OH_{ad} + H^+ + e^- \tag{6.3}$$

$$CO_{ad} + OH_{ad} \rightarrow CO_2 + H^+ + e^- + 2\,M \tag{6.4}$$

$$X + M \leftrightarrow X_{ad} \tag{6.5}$$

Equation (6.1) describes the transport of CO from the bulk solution to the electrode surface, (6.2) describes the adsorption of CO on a free site of the electrode, denoted by M, (6.3) describes the oxidative chemisorption of water on the electrode, (6.4) describes the reaction between adsorbed CO and adsorbed OH species and (6.5) describes the ad- and desorption of anions X on free surface sites. This reaction mechanism can be cast into a set of four ordinary differential equations determining the temporal evolutions of the CO concentration in front of the electrode c_s, and the coverage of CO (θ_{CO}), OH

(θ_{OH}), and anions (θ_X). The evolution equations of c_s, θ_{CO}, θ_{OH} have already been discussed above and are given by equations 6.6, 6.7, and 6.8, respectively.

$$\frac{dc_s}{dt} = -\frac{2S_{tot}}{\delta}\nu_{CO,a} + \frac{2D}{\delta^2}(c_b - c_s) \tag{6.6}$$

$$\frac{d\theta_{CO}}{dt} = k_{CO,a}c_s(0.99 - \theta_{CO} - \theta_{OH} - \theta_X) - k_r\theta_{OH}\theta_{CO}e^{\frac{\alpha FU}{RT}} \tag{6.7}$$

$$\frac{d\theta_{OH}}{dt} = k_{OH,a}(\theta_{OH}^m(1 - \theta_{CO} - \theta_X) - \theta_{OH})e^{\frac{\alpha FU}{RT}} - k_{OH,d}\theta_{OH}\, e^{\frac{-(1-\alpha)FU}{RT}} - k_r\theta_{OH}\theta_{CO}\, e^{\frac{\alpha FU}{RT}} \tag{6.8}$$

The equation describing the temporal evolution of the coverage of anions, which is similar to equation (5.3) except the term for repulsive interaction, reads

$$\frac{d\theta_x}{dt} = k_{X,a}c_x(0.99 - \theta_X - \theta_{CO} - \theta_{OH})\, e^{\frac{n_x\alpha FU}{RT}} - k_{X,d}\theta_X\, e^{\frac{n_x(\alpha-1)FU}{RT}} \tag{6.9}$$

Here, $k_{X,a}$ and $k_{X,d}$ denote the rate constants of adsorption and desorption of anions, respectively. U, R, F, α, and T have their usual meanings, c_x is the anion bulk concentration, and n_x the number of electrons transferred upon ad- and desorption of anions. Since the oscillations appeared also in 0.5 M H_2SO_4, i.e. for a negligible cell resistance, we can equate the double layer potential with the externally applied potential U. In other words, ϕ_{DL} is treated as a parameter, and unlike all other models describing electrochemical oscillations, the model is a strictly potentiostatic model. The expression for the total current density becomes

$$\begin{aligned} i_F = FS_{tot}[&k_{OH,a}(\theta_{OH}^m(1 - \theta_{CO} - \theta_X) - \theta_{OH})e^{\frac{\alpha FU}{RT}} - k_{OH,d}\theta_{OH}\, e^{\frac{-(1-\alpha)FU}{RT}} \\ &+ k_{X,a}\, n_x c_x(0.99 - \theta_X - \theta_{CO} - \theta_{OH})\, e^{\frac{n_x\alpha FU}{RT}} - k_{X,d}\, n_x\theta_X\, e^{\frac{n_x(\alpha-1)FU}{RT}} \\ &+ k_r\theta_{OH}\theta_{CO}e^{\frac{\alpha FU}{RT}}] \end{aligned} \tag{6.10}$$

All parameter values used in the calculations except of those appearing in equation (6.9) are given in table 4.1. The parameters related to the anion dynamics (equation 6.9) are given in table 6.1.

Parameters	Value	Unit
$k_{X,a}$	500	$cm^3.mol^{-1}.s^{-1}$
$k_{X,d}$	5	s^{-1}
n_x	0.2	

Table 6.1: Anion parameters used in the simulations.

Calculated cyclic voltammograms for four different concentrations of anions are presented in Figure 6.31. They exhibit a hysteresis between a CO-poisoned and a reactive state.

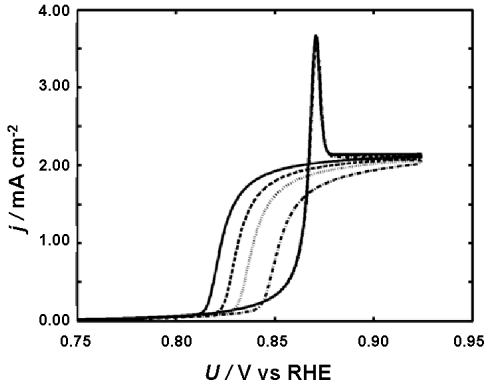

Figure 6.31: Calculated cyclic voltammograms for different anion concentrations c_x. c_x = 0 mM (solid line), 5 mM (dashed line), 10 mM (dotted line), 20 mM (dot-dashed line). Scan rate: 50 mV/s; rotation rate: 1200 rpm. The remaining parameters are given in tables 6.1 and 4.1).

As discussed above, this is typical of bulk CO electrooxidation. Moreover, the transition from the reactive to the poisoned state during a negative scan occurs more positive with increasing anion concentration while the onset potential of CO electrooxidation during the positive scan is independent of the anion concentration. This is exactly what was also observed in experiments (Figure 6.1). Thus, the experimental observations at high scan rate can be explained assuming that BF_4^- ions competitively adsorb on the electrode, thereby blocking free surface sites for OH and CO adsorption. Also, experiments at fixed applied voltage are well reproduced by the model and for an outer voltage just positive to the transition from the poisoned to the reactive state, the calculated current density exhibits sustained oscillations (Figure 6.32). Thus, already the simplest possible description of anion ad- and desorption gives rise to oscillatory behaviour. Moreover, the simulated oscillations are strictly potentiostatic oscillations. The qualitative agreement with the experimental results suggests that CO

electrooxidation in the presence of inhibiting anions represents the first electrochemical system with strictly potentiostatic oscillations.

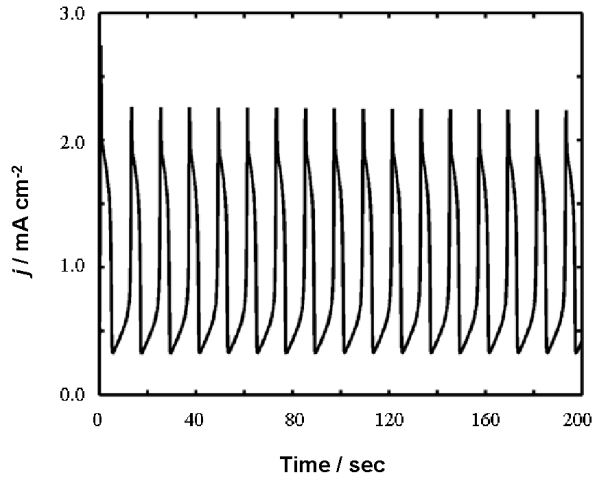

Figure 6.32: Calculated current time series for U = 858 mV and c_x = 20 mM; rotation rate: 1200 rpm (Parameters are given in the table 6.1 and table 4.1).

Since in reaction step (6.5) the chemical nature of the adsorbing anions is not taken into account, any anion, which competes with the oxide species for free surface sites, may induce oscillations in some concentration window, which is in agreement with the observation of oscillations upon addition of different anions namely BF_4^-, Cl^- or Br^-.

6.4.2 Comparison between simulations and experimental results

To shed more light on the oscillation mechanism the temporal evolution of all three coverages and of the free surface sites are plotted in Figure 6.33. As discussed above, the Langmuir Hinshelwood mechanism creates a positive feedback loop. The reaction of adsorbed OH with adsorbed CO produces CO_2, which desorbs immediately from the surface creating two active sites. This makes more free sites available for further adsorption of OH.

The adsorption of CO is mass transport limited, whereas the one of OH^- is not. As soon as the autocatalytic process starts, the CO coverage goes down and the OH coverage goes up as shown in region A of Figure 6.33b by the red and blue lines, respectively. This process also increases the number of free active sites as indicated by the black line in Figure 6.33b and the active site can be interpreted as the activator. The generation of the activator induces the production of the inhibitor, here this leads to the accumulation of anions on the surface, as shown by the green curve in the segment B in Figure 6.33c.

As the inhibitor starts to accumulate on the surface, the numbers of free surface sites reduce, corresponding to the activator, which is evident from the black curve in segment B of Figure 6.33c.

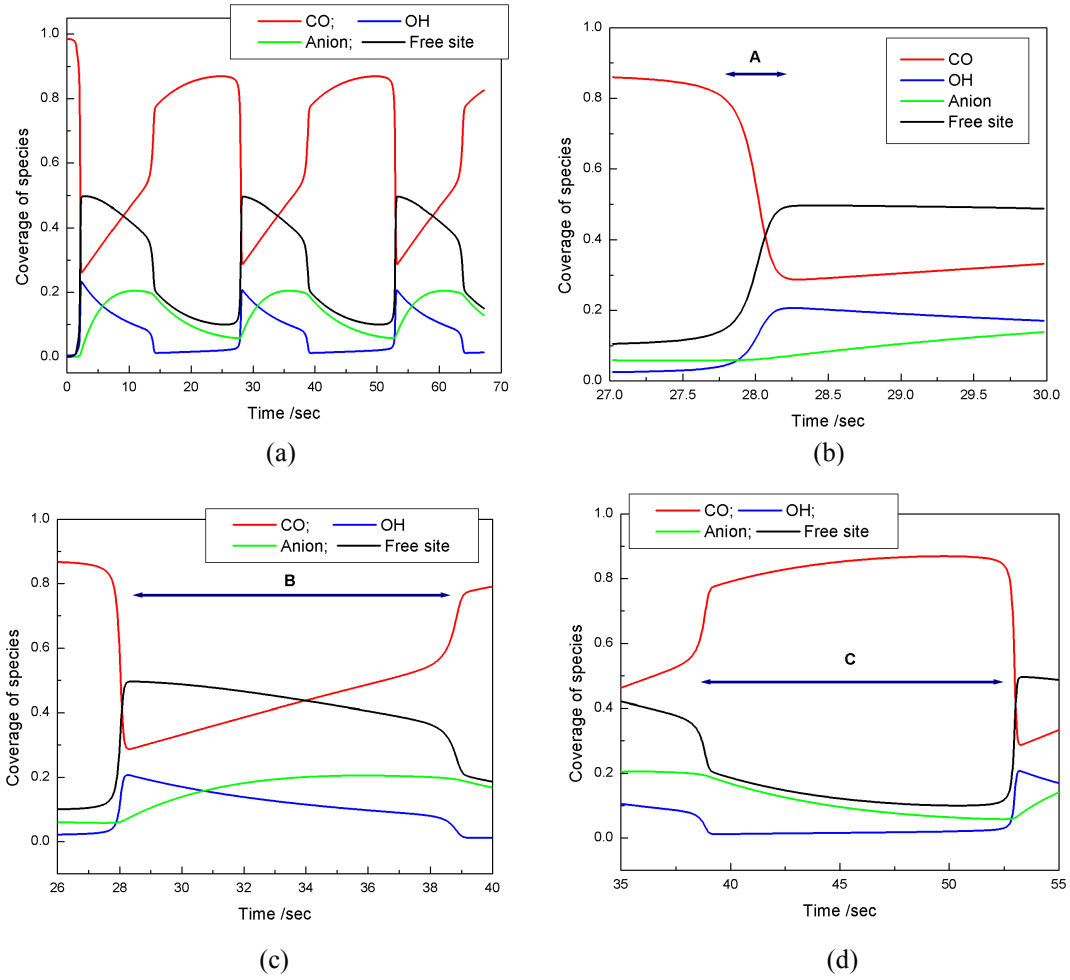

Figure 6.33: (a) Time series of the coverages of various species during an oscillation. (b) The autocatalytic process is active in segment A (c) Accumulation of anions or inhibitor species occurs in segment B. (d) Reverse autocatalytic process and consecutive slow decrease of anions or inhibitor species (segment C). The parameters used in the simulation are given in tables 6.1 and 4.1.

When the anions coverage has exceeded a critical value, the autocatalytic reaction cannot be maintained anymore, and thus CO and OH coverages decrease sharply. This also decreases the number of free surface sites, which is seen at the end of segment B (Figure 6.33c). This in turn reduces the inhibitor, which is reflected here by the desorption of the anions as indicated in the segment C of Figure 6.33d. As the inhibitor disappears from the system, at some point of time, the original conditions are re-established and the cycle starts again. In an activator-inhibitor system, oscillations arise if the characteristic changes of the activator occur on a faster time-scale than the ones of

the inhibitor. In other words, the inhibitor must respond to a variation of the activator variable with some delay. This is evident from figure 6.33 in the proposed case, where the time scale of the autocatalytic step is faster than the time scale of anion adsorption.
It seems to be obvious that this simple mean field model cannot reproduce all of the experimental observations. To identify the weak points and to get insight in which directions the model should be augmented, we next compare simulated bifurcation diagrams with the experimental ones. Let us first, however, compare typical shapes of simulated and experimental current oscillations. Both are characterized by an overshooting of the current density and a shoulder at approximately the level of the high current state for the bistable condition and otherwise identical parameters followed by a faster decay. The rising flank of the current exhibits, however, a pronounced difference: While in the experiments a nearly linear increase in current density was observed, in the simulated time series the current increase takes first place on a slow time scale that is followed by a fast one.

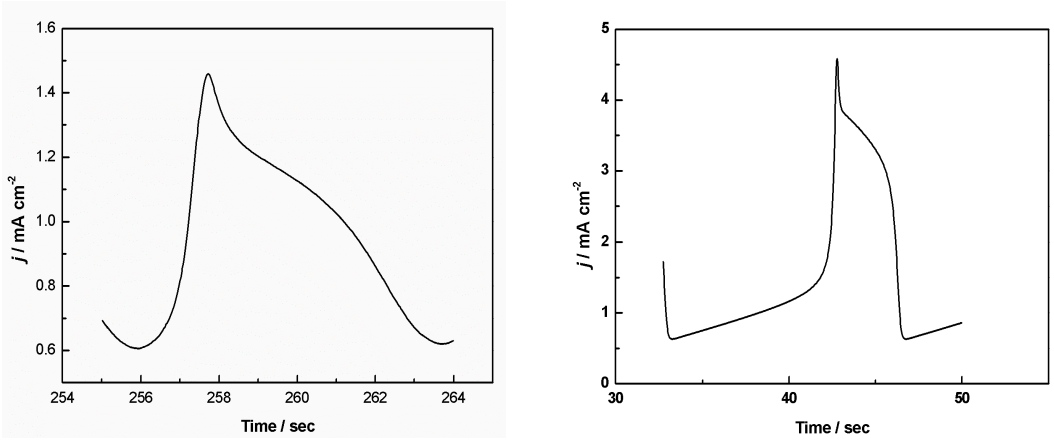

(a) (b)

Figure 6.34: Shape of a typical current oscillation in time. (a) experimental and (b) simulated waveform (Parameters are given in the table 6.1 and table 4.1).

6.4.2.1 Electrode rotation rate

Figure 6.35 shows the location of Hopf bifurcations as predicted in the model as a function of the electrode rotation rate and the applied voltage. The oscillatory region exceeds the experimentally accessible rotation range and the experiments and simulations exhibit identical trends. In the experiments, the potential window for regular oscillations shifted slightly negative when the rotation rate was lowered from 1200 rpm to 200 rpm, as it is found in the corresponding rotation rate interval in the simulations. Thus, the effect of the rotation rate is almost quantitatively captured by the simulation.

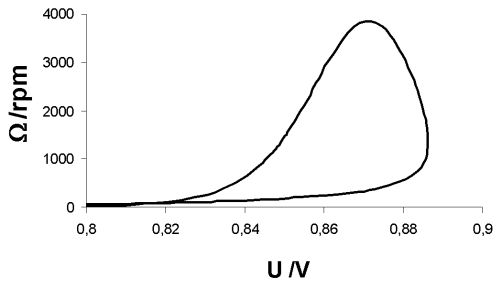

Figure 6.35: Simulated location of the Hopf bifurcation as a function of electrode rotation rate and external voltage parameter plane. $c_x = 5$ μM; $n_x = 0.3$; (All other parameters are mentioned in the table 6.1 and table 4.1).

6.4.2.2 Anion concentration

Figure 6.36 shows the location of the Hopf bifurcation in a two-parameter bifurcation diagram spanned by the anion concentration and the external voltage. The model shows oscillations roughly in the concentration range from 10^{-6} M Cl^- to 10^{-5} M Cl^-; contrary, in the experiments the anion concentration can be varied by three orders of magnitude. Therefore, though the qualitative feature of the experiments is captured, there is a large quantitative discrepancy. Furthermore, the model predicts only simple periodic oscillations. In the experiments, in wide parameter regions, solely irregular oscillations were found. The model was derived assuming homogeneous dynamics, i.e. spatial effects are not captured. Irregular oscillations might arise from a spatial instability: therefore, a logical step is to expand the model by the spatial dimension. However, it is less likely that the spatially extended model resolves also the discrepancy in the anion concentration range. Rather a more refined description of anion ad- and desorption including possibly attractive or repulsive interactions among the anions and perhaps also between anions and other adsorbing species seems to be necessary.

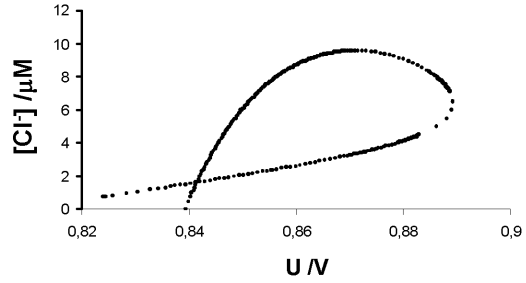

Figure 6.36: Simulated location of the Hopf bifurcation in the Cl^- concentration and external voltage parameter plane. $n_x = 0.3$; (All other parameters are given in the table 6.1 and table 4.1).

6.4.2.3 Electrolyte resistance

In the experiments, we have seen that the oscillations prevail up to low electrolyte concentrations or high values of an external series resistance, though they are irregular in wide resistance ranges. In order to investigate the effect of increasing resistance on the dynamics, the set of equations (6.6), (6.7), (6.8), and (6.9) has to be augmented by the evolution equation for the electrode potential:

$$C\frac{d\phi_{DL}}{dt} = -i_F + \frac{U-\phi_{DL}}{R} \tag{6.11}$$

where C is the double layer capacitance and R is the total cell resistance. The Faradaic current i_F is given by equation 6.10. Figure 6.37 shows the simulated location of the Hopf bifurcation as a function of series resistance and applied voltage. It shows that as the solution resistance is increased, the voltage range of oscillations decreases and vanishes for a cell resistance as low as 10 Ω. In the experiments, the regular oscillations were observed even for a series resistance of 700 Ω, and irregular oscillations appeared positive and negative to the voltage interval of regular oscillations.

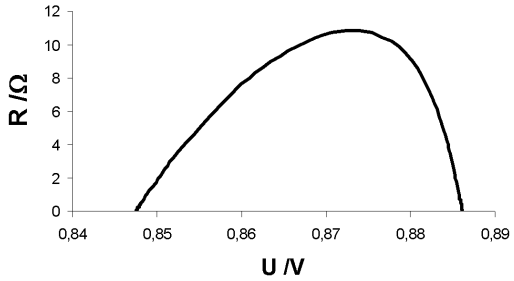

Figure 6.37: Simulated location of the Hopf bifurcation as a function of series resistance and applied voltage c_x = 5 μM; n_x = 0.3; C = 20 μF (All other parameters are given in the table 6.1 and table 4.1).

In contrast, in the simulations again only regular oscillations were observed. Concerning the range of all parameters in which unstable behaviour develops the agreement between simulations and experiments are certainly the poorest for the resistance. Again, a spatial instability is likely to be the reason. Therefore, first simulations with a spatially extended model were carried out in collaboration with A. Bonnefont. The results give much insight into the complex dynamics of CO electrooxidation. They are discussed in the next paragraph. The parameters for these simulations are mentioned in the table 6.1.

6.4.3 Spatial structure and irregular oscillations

In the spatially extended system three possible spatial couplings are present.

(a) Coupling by diffusion of CO in front of the electrode (surface diffusion of adsorbed CO and OH^- are much slower and therefore neglected).

(b) Migration coupling through the electrolyte.

(c) Global coupling when a series resistance is included in the experiment.

To incorporate the spatial coupling into the model a quasi one dimensional ring electrode was considered. We call *x* the direction along the ring and *z* the direction perpendicular to the ring. The spatio-temporal behaviour of the double layer potential results from a local charge balance and reads (for the derivation see [51])

$$C\frac{\partial\phi}{\partial t} = -i_F - \sigma\frac{\partial\phi_{DL}}{\partial z}\bigg|_{z=WE} \tag{6.12}$$

Here σ denotes the conductivity of the electrolyte and ϕ the electric potential in the electrolyte. *z* = WE is a position at the WE. Thus, the last term of equation (6.12) describes the local migration current density entering the electrochemical double layer and the equation means that the charging of the double layer is equal to the difference between local migration and Faradaic current densities. The electric potential in the electrolyte, ϕ, obeys Laplace's equation

$$\Delta\phi = 0 \tag{6.13}$$

from which $\frac{\partial\phi}{\partial z}$ can be calculated. Laplace's equation is solved on a two dimensional cylindrical surface, i.e. for periodic boundary conditions in the *x* direction and, a homogeneous potential distribution at one end of the cylinder, where it is assumed that the CE is located, and some potential distribution at the WE $\phi|_{Z=WE}$, which results from an initial distribution of ϕ_{DL}. At the CE, the potential was set to zero: $\phi|_{Z=0} = 0$. ϕ_{DL} and ϕ are linked by the potentiostatic control condition $U = \phi_{DL} + iR_{ex} + iR_u$. Here R_{ex} is an external series resistance and R_u is the uncompensated resistance of the electrochemical cell, i.e. the resistance between the WE and RE. Equation (6.12) can be reformulated in such a way that migration and global coupling appear in separate terms:

$$C\frac{\partial\phi}{\partial t} = -i_F - \frac{u-\phi_{DL}}{AR_\Omega(1+\gamma)} + \frac{1}{AR_\Omega}\frac{\gamma}{1+\gamma}(\langle\phi_{DL}\rangle - \phi_{DL}) - \sigma(\frac{\partial\phi}{\partial z} - \phi)\bigg|_{z=WE} \tag{6.14}$$

Here the first two terms on the L.H.S. comprise the homogeneous dynamics. R_Ω is the cell resistance, i.e. the total resistance between the working and the counter electrodes, and γ is defined as

$$\gamma = \frac{R_{ex} - R_c}{R_\Omega} \tag{6.15}$$

with

$$R_\Omega = R_c + R_u \tag{6.16}$$

The third term describes the global coupling. In the experiments, the RE was located behind the CE to avoid negative global coupling such that R_c = 0. Thus, the global coupling term is non zero only when an external resistor is placed in series to the WE. The last term, finally, describes the migration coupling, whose strength is proportional to the conductivity of the electrolyte. The first simulations conducted with the system are shown in Figure 6.38 and Figure 6.39.

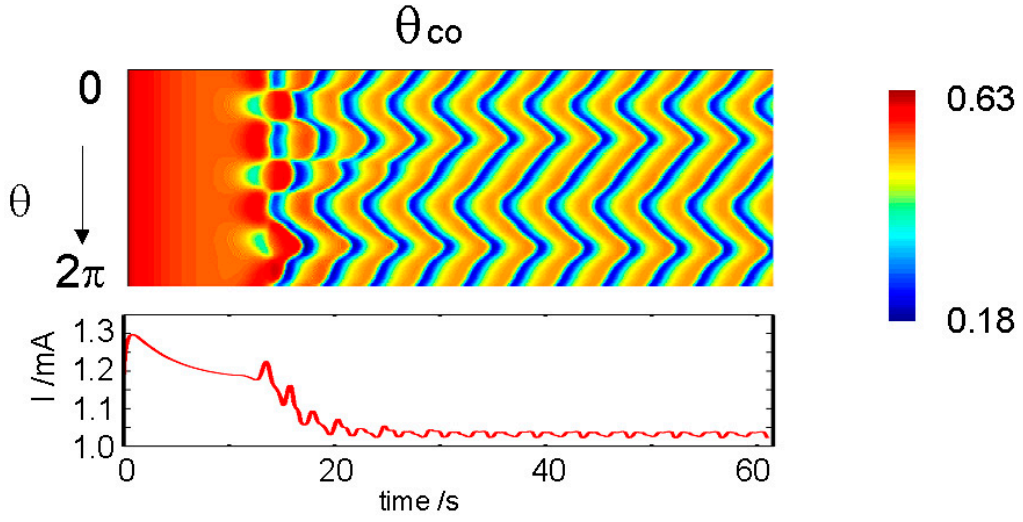

Figure 6.38: Simulated spatial pattern during CO electrooxidation. The top figure shows the spatial distribution of CO coverage on the electrode with time and the bottom figure shows the corresponding global current time series. R = 100 Ω. σ=100 ohm^{-1} cm^{-1}.

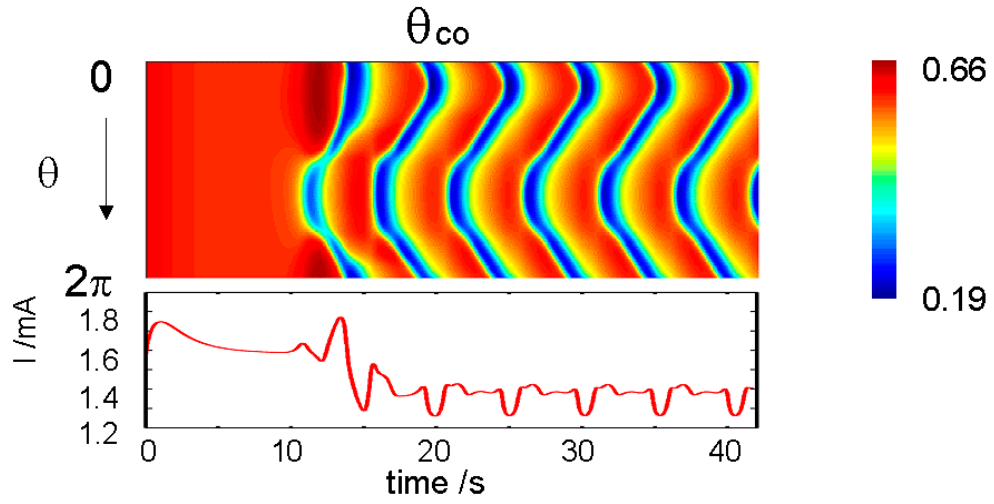

Figure 6.39: Simulated spatial pattern during CO electrooxidation. The top figure describes the spatial distribution of the CO coverage on the electrode with time and the bottom figure shows the corresponding global current time series. R = 30 Ω. σ=100 ohm^{-1} cm^{-1}.

In each figure, the top diagram displays the spatial distribution of the CO coverage on the electrode surface. The angular position of the ring electrode is plotted along the *y* axis and time along the *x* axis. The bar graph next to the figure marks the weight of the colour, and blue indicates a low and red a high CO coverage. The corresponding bottom curves show a time series of the global current. In both cases, the homogeneous system did not exhibit oscillatory solutions and the calculations were done with an external resistance, i.e. in the presence of a global coupling. Clearly, the spatial coupling destabilizes the homogeneous state and patterns develop. The patterns are composed of source points that periodically send out pulses, which propagate across the ring electrode and annihilated upon collision. With the smaller external resistance, there is one source point while with the larger resistance two source points that emit the pulses at different time exist. In our context the most important feature, however, is that the oscillations of the global current are complex periodic and have an amplitude, which is by far smaller than the amplitude of the simple periodic oscillations of the homogeneous model. In the experiments, in corresponding parameter regions small amplitude irregular oscillations were observed. However, the irregularity could also be the result of noise superimposed on complex, periodic small amplitude oscillations. Therefore, the initial simulations support the hypothesis made above that in large parameter intervals the oscillations do not occur homogeneously but are accompanied by spatial pattern formation. It is an experimental challenge of future work to measure these patterns. Currently, there seems

to be just one experimental method that is suitable for the in-situ observation of spatial structures, which is spatially resolved FTIR spectroscopy, where direct information on the spatial distribution of CO can be obtained. However, this method was only demonstrated to work very recently [189] and corresponding experiments were thus not yet available when this thesis was done.

6.4.4 Discussion

In the experiments, oscillations were found in concentrated supporting electrolytes, such as 0.5 M H_2SO_4, under potential control, i.e. under conditions, under which the ohmic potential drop through the electrolyte is minimal. This points to a purely chemical origin of the Hopf instability, and in fact, in simulations the oscillations were also obtained when treating the electrode potential as a parameter. An analysis of the reaction mechanism (6.1)-(6.5) reveals that the anions coverage acts like an inhibitor, and the oscillations arise owing to the interplay of the positive feedback loop stemming from the Langmuir-Hinshelwood mechanism coupled to the mass transfer limited step and the negative feedback loop generated by anion ad- and desorption. Thus, the system can be characterized as an 'S-NDR system with chemical inhibition' or as a strictly potentiostatic oscillator, in which the electrolyte resistance does not play an essential role for the oscillatory instability. This class of electrochemical oscillator had been speculated to exist; however, so far an unambiguous identification was missing. There are two other reports of oscillations during CO electrooxidation on Pt. Azevedo et al. [63] observed current oscillations in 0.1 M $HClO_4$ on Pt. This occurred in a small potential window positive to the ignition peak, which coincides with the voltage range in which the above described oscillations occurred. Thus, the simplest interpretation of the origin of the oscillations reported in [63] seems to be that there were traces of the foreign anions in the $HClO_4$ electrolyte. Koper et al. [45] observed potential oscillations under galvanostatic conditions in $HClO_4$ and in H_2SO_4 on Pt single crystal electrodes, again without addition of inhibiting anions. The above described homogeneous model does not possess oscillatory solutions under galvanostatic conditions, so that the origin of these oscillations appears different from the present ones, and it remains unclear whether there is any relation between the oscillations observed here and in [45]. However, it is striking that in our work as well as in their work the oscillations are

irregular in $HClO_4$ while regular oscillations have been reported for Pt(111) electrodes in H_2SO_4 solutions [45].

6.5 Summary

We demonstrated that CO electrooxidation on platinum in the presence of strongly adsorbing anions exhibits oscillations in wide parameter ranges. Evidence was provided that the autocatalytic loop stems from the LH mechanism of CO electrooxidation and the negative or inhibiting feedback is due to the specific adsorption of anions. Thus, this electrochemical oscillator is strictly potentiostatic in nature. This result is important not only because it presents the first experimental example of this class of electrochemical oscillators but it also indicates that an understanding of the CO electrooxidation is impossible without considering the influence of anions. The oscillations were found with tetrafluoroborate, chloride, and bromide anions. Furthermore, no oscillations could be induced in the presence of iodide ions. This order indicates that the rate of adsorption, which is proportional to the product of the rate constant of the anion adsorption k_{ads}, and the concentration, is decisive for the oscillatory instability to occur, not the chemical nature of the anion. Thus, the interaction of anions with adsorbed CO and OH is only due to the competition for free surface sites, while repulsive or attractive interactions between the adsorbed species apparently do not play a role for the oscillatory instability. With chloride and bromide ions oscillations establish with the concentration as low as 10^{-7} M, and it can be varied by at least two orders of magnitude. The low concentrations, which induce oscillations, suggest that the oscillations can be exploited to determine traces of chloride or bromide in H_2SO_4 or $HClO_4$ base electrolyte. Since the oscillation frequency is a function of the anion concentration, a rough quantitative estimation of the anion concentration is possible.

While the oscillatory instability occurs independent of the chemical nature of the anions, a surprising difference in the dynamic responses was found for different supporting electrolytes. Thus, in $HClO_4$ containing base electrolyte only irregular oscillations established, in aqueous H_2SO_4, in contrast, also nicely periodic oscillations could be adjusted. This raises the fundamental question about the interaction of these anions with platinum. As a working electrode, polycrystalline as well as low indexed Pt electrodes were employed. Though, with all four different WEs oscillations could be detected, parameter ranges, typical oscillation shapes etc. were different. This points to the fact

that details of the dynamics can only be understood when taking into account structural effects. These findings expand not only the experimentally verified categories of electrochemical oscillators but makes it also likely that spatio-temporal patterns of the reaction-diffusion type, as opposed to reaction-migration patterns that form in 'traditional electrochemical oscillating systems', may establish on the electrode surfaces. Concerning the fundamental aspects of CO catalysis, the observed dynamic instabilities underline that it is necessary to incorporate the possibility for cooperative phenomena when analysing the experimental data, and especially when trying to bridge the gap between microscopic measurements and mean field behaviour.

Chapter 7: Conclusions

In this work, new results on bulk CO electrooxidation on polycrystalline and single crystal platinum are presented. The emphasis of the studies is on investigations of cooperative effects, i.e. effects that cannot be explained by the simple superposition of the individual elementary steps but require their nonlinear interaction. Besides, also questions related to surface physical aspects are addressed.

A simple reaction network of CO electrooxidation, which had been discussed in the literature before this thesis was taken up, contains a positive, i.e. self-enhancing, feedback loop, and thus an intrinsic source of dynamic instabilities. For example, it can lead to bistability between a high and a low current branch in a certain range of applied voltage, the current-voltage characteristic being thus S-shaped. Hence, it had been postulated that bulk CO electrooxidation belongs to the class of so-called S-shaped negative differential resistance (S-NDR) systems that are especially prone to instabilities. Therefore, we first tested in an independent way whether bulk CO electrooxidation is indeed an S-NDR system. This was done by applying a derivative feedback control to the system. The control was designed such that its only impact was to alter the effective capacitance of the electrode|electrolyte interface. S-NDR systems are known to undergo an oscillatory instability if the double layer capacitance is sufficiently large, the low double layer capacitance of a Pt - aqueous electrolyte interface, however, impedes the occurrence of oscillations. When employing the control strategy, oscillations in the reaction rate could indeed be adjusted. We thus obtained independent evidence that the reaction mechanism of CO electrooxidation contains a positive feedback loop, and that the system can be classified as an S-NDR system. Furthermore, we could semi-

quantitatively reproduce the experimental results, most importantly the oscillatory instability, in simulations.

Subsequently, we designed experiments that should shed light on the impact of co-adsorption of anions on the dynamics of CO electrooxidation.

First, diluted sulfuric or perchloric acid electrolytes and low bulk CO concentrations were used and Pt (111), Pt (100) and Pt (110) single crystal electrodes were employed. On Pt(100) and (110), these conditions facilitated the oxidation of adsorbed CO at unusually negative potentials, a result that is especially important in the context of minimizing the CO poisoning of Pt electrodes, e.g., in low-temperature fuel cells. The results were complicated by a slow shift of the electrooxidation peak with time towards higher potentials. By systematically varying the negative turning point in cyclic voltammetry, the bulk CO concentration and the concentration of the supporting electrolyte, the conditions under which the low oxidation potentials appeared were identified, and various possible origins for the positive shift of the reaction peak could be excluded. As most probable reason for this 'peak transition' the slow formation of a water adlayer-structure was conjectured; however, without further experiments this interpretation remains speculative.

Second, the investigations of interactions between anions from the most important supporting electrolytes, namely sulfate and perchlorate, and CO electrooxidation were investigated in the bistable region of this reaction. Previous studies always focused on the onset of oxidation from a CO covered electrode surface. This potential is, however, considerably more positive than the potential at which the system returns from the reactive state to the poisoned state. Thus the question for the lowest potential at which CO oxidation might still commence and how this potential is determined by the interaction of reaction steps, especially adsorption rates of anions, CO and OH, and mass transport cannot be answered by studying the onset potential of the reaction. Rather, studies of the transition from the reactive to the poisoned state are necessary. Since from a bifurcation theoretical point of view the transition between the two states is accompanied with a saddle node bifurcation, we denote this transition as SN2 point. We found that the SN2 point shifts considerably negative with decreasing CO bulk concentration. Furthermore, it sensitively depends on the nature of the anion. The SN2

point is about 60 mV more negative in perchloric acid than in sulfuric acid. Varying the ratio between sulfuric and perchloric acid at constant total anion concentration revealed that already a small amount of sulfate anions lead to a positive shift of the SN2 point by about 60 mV. This was found for both, polycrystalline Pt and Pt(111) electrodes. Comparison of the experimental results with mean field simulations showed that the observed trends of the SN2 point are a consequence of the Langmuir Hinshelwood mechanism and the competitive adsorption of anions with CO and OH. The results could be best fitted assuming a repulsive interaction between the anions.

Finally, anions that are known to strongly adsorb on Pt electrodes were added to perchloric acid or sulfuric acid base electrolyte. These strongly adsorbing anions induced an oscillatory instability. Evidence was given that the oscillations emerge due to the interaction between the above mentioned positive feedback loop arising from the Langmuir-Hinshelwood mechanism and a negative feedback loop caused by anion adsorption. Therefore, the oscillations depend only on chemical variables, while the electrode potential, which is an essential variable in all electrochemical oscillators that had been known before, stays constant during the oscillations and thus acts as a parameter. For the latter reason, the oscillations are called strictly potentiostatic oscillations.

The effect of various experimental parameters on this new type of oscillations was investigated, namely the concentration and the nature of the inhibiting anion, the concentration and the nature of the base electrolyte, the rotation rate of the electrode, the magnitude of an external series resistance and the surface of the Pt electrode. With polycrystalline Pt electrodes tetrafluoroborate, chloride, bromide and iodide were employed as strongly adsorbing anions. With the first three types of anions oscillations could be established, while no oscillations were found using iodide ions. Furthermore, the highest anion concentration that still induced oscillatory behavior depended on the adsorption strength of the anion, and was higher for chloride than for bromide. Yet, for both, chloride and bromide, oscillations were still detected with anion concentrations as low as 10^{-7} M. This might open a new path for detection of trace amounts of chloride and bromide, at least sulfuric or perchloric acid solution. The (mean) oscillation period depended on the anion concentration, pointing to a possible quantitative assessment of the anion concentration.

Distinct differences of the oscillatory behavior were also found when using different base electrolytes: While with sulfuric acid as base electrolyte regular oscillations were found in wide parameter ranges irrespective of the nature of the inhibiting anion, only irregular oscillations could be detected in perchloric acid electrolytes. This demonstrates that at least partially the anions of the base electrolyte play an active role during the oscillations, even though they are not essential for inducing the oscillations. Furthermore, the results strongly suggest that the irregular oscillations and complex wave forms are accompanied by spatial pattern formation.

Using single crystal electrodes we could demonstrate that the oscillatory dynamics sensitively depends on the crystal facet, all three low indexed surfaces exhibiting qualitatively different fingerprints of the oscillatory instability.
Nevertheless, simulations showed that despite the intricate parameter dependences discussed above, an oscillatory instability is already obtained when augmenting the mean field model capturing the Langmuir-Hinshelwood mechanism of CO oxidation by a single equation describing ad- and desorption of anions, the interaction of the anions with CO or OH being restricted to the competition of the three adsorbing species for free surface sites. A semi-quantitative comparison of the oscillatory region reveals, however, that in experiments the oscillations exist in far larger parameter regions (for some parameters several orders of magnitude) than predicted by the simple mean field model. First simulations with a spatially extended model point again to the formation of patterns, which were found in parameter regions in which the lumped model predicted a stable stationary state.

The discovery of oscillations during CO electrooxidation on Pt opens a wide and new field. The investigations carried out in the framework of this thesis helped to better understand several aspects of CO electrooxidation, yet they have uncover even more open questions, ensuring thus that CO electrooxidation on Pt remains an interesting and important system to study for many more years to come.

References

[1] N. M. Markovic. in *Handbook of Fuel cells* edited by W. Vielstich, A. Lamm and H. A. Gasteiger. Chichester, Wiley (**2003**)

[2] T. Iwasita. in *Handbook of Fuel cells* edited by W. Vielstich, A. Lamm and H. A. Gasteiger. Chichester, Wiley (**2003**)

[3] N. M. Markovic and P. N. Ross. Surface science studies of model fuel cell electrocatalysts. *Surface Science Reports* 45, 4-6 (**2002**) 117-229.

[4] B. N. Grgur, N. M. Markovic, C. A. Lucas and P. N. Ross. Electrochemical oxidation of carbon monoxide: from platinum single crystals to low temperature fuel cells catalysts. Part I: Carbon monoxide oxidation onto low index platinum single crystals. *Journal of the Serbian Chemical Society* 66, 11-12 (**2001**) 785-797.

[5] B. Beden, N. Collas, C. Lamy, J. M. Leger and V. Solis. Electrosorption of carbon-monoxide at the platinum electrolyte interface. *Surface Science* 162, 1-3 (**1985**) 789-795.

[6] B. Beden, C. Lamy, N. R. Detacconi and A. J. Arvia. The electrooxidation of CO - a test reaction in electrocatalysis. *Electrochimica Acta* 35, 4 (**1990**) 691-704.

[7] B. Beden, S. Bilmes, C. Lamy and J. M. Leger. Electrosorption of carbon-monoxide on platinum single-crystals in perchloric-acid medium. *Journal of Electroanalytical Chemistry* 149, 1-2 (**1983**) 295-302.

[8] J. M. Leger, B. Beden, C. Lamy and S. Bilmes. Carbon-monoxide electrosorption on low index platinum single-crystal electrodes. *Journal of Electroanalytical Chemistry* 170, 1-2 (**1984**) 305-317.

[9] S. A. Bilmes, N. R. Detacconi and A. J. Arvia. The electrooxidation of chemisorbed CO on polycrystalline platinum - a mechanistic interpretation of the anodic current peak multiplicity. *Journal of Electroanalytical Chemistry* 164, 1 (**1984**) 129-143.

[10] J. M. Leger, B. Beden and C. Lamy. The adsorption of carbon-monoxide on platinum single-crystals in alkaline-medium. *Berichte Der Bunsen-Gesellschaft* 91, 4 (**1987**) 336-341.

[11] J. M. Feliu, J. M. Orts, A. Fernandezvega, A. Aldaz and J. Clavilier. Electrochemical studies in sulfuric-acid-solutions of absorbed CO on Pt (111) electrodes. *Journal of Electroanalytical Chemistry* 296, 1 (**1990**) 191-201.

[12] J. A. Caram and C. Gutierrez. Voltammetric study of the electroadsorption and electrooxidation of CO on Pt in 0.5 M $HClO_4$ - influence of several experimental-variables. *Journal of Electroanalytical Chemistry* 346, 1-2 (**1993**) 451-469.

[13] H. A. Gasteiger, N. M. Markovic and P. N. Ross. H_2 and CO electrooxidation on well-characterized Pt, Ru, and Pt-Ru. 2. Rotating disk electrode studies of CO/H_2 mixtures at 62°C. *Journal of Physical Chemistry* 99, 45 (**1995**) 16757-16767.

[14] N. M. Markovic, B. N. Grgur, C. A. Lucas and P. N. Ross. Surface electrochemistry of CO on Pt(110)-(1x2) and Pt(110)-(1x1) surfaces. *Surface Science* 384, 1-3 (**1997**) L805-L814.

[15] M. Bergelin, J. M. Feliu and M. Wasberg. Study of carbon monoxide adsorption and oxidation on Pt(111) by using an electrochemical impinging jet cell. *Electrochimica Acta* 44, 6-7 (**1998**) 1069-1075.

[16] A. V. Petukhov, W. Akemann, K. A. Friedrich and U. Stimming. Kinetics of electrooxidation of a CO monolayer at the platinum/electrolyte interface. *Surface Science* 404, 1-3 (**1998**) 182-186.

[17] N. M. Markovic, C. A. Lucas, B. N. Grgur and P. N. Ross. Surface electrochemistry of CO and H_2/CO mixtures at Pt(100) interface: Electrode kinetics and interfacial structures. *Journal of Physical Chemistry B* 103, 44 (**1999**) 9616-9623.

[18] C. A. Lucas, N. M. Markovic and P. N. Ross. The adsorption and oxidation of carbon monoxide at the Pt(111)/electrolyte interface: atomic structure and surface relaxation. *Surface Science* 425, 1 (**1999**) L381-L386.

[19] N. P. Lebedeva, M. T. M. Koper, E. Herrero, J. M. Feliu and R. A. van Santen. CO oxidation on stepped Pt n(111) x (111) electrodes. *Journal of Electroanalytical Chemistry* 487, 1 (**2000**) 37-44.

[20] E. Herrero, B. Alvarez, J. M. Feliu, S. Blais, Z. Radovic-Hrapovic and G. Jerkiewicz. Temperature dependence of the CO_{ads} oxidation process on Pt(111) Pt(100), and Pt(110) electrodes. *Journal of Electroanalytical Chemistry* 567, 1 (**2004**) 139-149.

[21] N. M. Markovic, T. J. Schmidt, B. N. Grgur, H. A. Gasteiger, R. J. Behm and P. N. Ross. Effect of temperature on surface processes at the Pt(111)-liquid interface: Hydrogen adsorption, oxide formation, and CO oxidation. *Journal of Physical Chemistry B* 103, 40 (**1999**) 8568-8577.

[22] I. Villegas and M. J. Weaver. Carbon-monoxide adlayer structures on platinum(111) electrodes - a synergy between in-situ Scanning-Tunneling-Microscopy and Infrared-Spectroscopy. *Journal of Chemical Physics* 101, 2 (**1994**) 1648-1660.

[23] I. Villegas, X. P. Gao and M. J. Weaver. Local-structure and phase-transitions within ordered electrochemical, adlayers - Some new insights from in-situ Scanning-Tunneling-Microscopy. *Electrochimica Acta* 40, 10 (**1995**) 1267-1275.

[24] M. Wakisaka, T. Ohkanda, T. Yoneyama, H. Uchida and M. Watanabe. Structures of a CO adlayer on a Pt(100) electrode in $HClO_4$ solution studied by in situ STM. *Chemical Communications* 21 (**2005**) 2710-2712.

[25] L. W. H. Leung, A. Wieckowski and M. J. Weaver. Insitu Infrared-Spectroscopy of well-defined single-crystal electrodes - Adsorption and electrooxidation of CO on Pt(111). *Journal of Physical Chemistry* 92, 24 (**1988**) 6985-6990.

[26] E. A. Batista, T. Iwasita and W. Vielstich. Mechanism of stationary bulk CO oxidation on Pt(111) electrodes. *Journal of Physical Chemistry B* 108, 38 (**2004**) 14216-14222.

[27] N. P. Lebedeva, A. Rodes, J. M. Feliu, M. T. M. Koper and R. A. van Santen. Role of crystalline defects in electrocatalysis: CO adsorption and oxidation on stepped platinum electrodes as studied by in situ infrared spectroscopy. *Journal of Physical Chemistry B* 106, 38 (**2002**) 9863-9872.

[28] E. Zippel, R. Kellner, M. Krebs and M. W. Breiter. ATR-IR studies of CO adsorption from solutions. *Journal of Electroanalytical Chemistry* 330, 1-2 (**1992**) 521-527.

[29] S. G. Sun and A. C. Chen. Insitu FTIRS features during oxygen-adsorption and carbon-monoxide oxidation at a platinum-electrode in dilute alkaline-solutions. *Journal of Electroanalytical Chemistry* 323, 1-2 (**1992**) 319-328.

[30] F. Kitamura, M. Takeda, M. Takahashi and M. Ito. CO adsorption on Pt(111) and Pt(100) single-crystal surfaces in aqueous-solutions studied by Infrared Reflection Absorption-Spectroscopy. *Chemical Physics Letters* 142, 5 (**1987**) 318-322.

[31] F. Kitamura, M. Takahashi and M. Ito. Carbon-Monoxide adsorption on platinum(111) single-crystal electrode surface studied by Infrared Reflection Absorption-Spectroscopy. *Surface Science* 223, 3 (**1989**) 493-508.

[32] E. Pastor, J. L. Rodriguez and T. Iwasita. A spectroscopic proof of a surface equilibrium between on top and bridge bonded CO at Pt(110) in acid solution. *Electrochemistry Communications* 4, 12 (**2002**) 959-962.

[33] C. S. Kim, W. J. Tornquist and C. Korzeniewski. Infrared-Spectroscopy as a probe of CO adsorption at Pt(335) under aqueous electrochemical conditions. *Journal of Physical Chemistry* 97, 24 (**1993**) 6484-6491.

[34] D. Kardash, J. M. Huang and C. Korzeniewski. Surface electrochemistry of CO and methanol at 25-75° C probed in situ by Infrared Spectroscopy. *Langmuir* 16, 4 (**2000**) 2019-2023.

[35] S. A. Wasileski, M. J. Weaver and M. T. M. Koper. Potential-dependent chemisorption of carbon monoxide on platinum electrodes: new insight from quantum-chemical calculations combined with vibrational spectroscopy. *Journal of Electroanalytical Chemistry* 500, 1-2 (**2001**) 344-355.

[36] V. Stamenkovic, K. C. Chou, G. A. Somorjai, P. N. Ross and N. M. Markovic. Vibrational properties of CO at the Pt(111)-solution interface: the anomalous stark-tuning slope. *Journal of Physical Chemistry B* 109, 2 (**2005**) 678-680.

[37] C. S. Kim, W. J. Tornquist and C. Korzeniewski. Site-dependent vibrational coupling of CO adsorbates on well-defined step and terrace sites of monocrystalline platinum - Mixed-isotope studies at Pt(335) and Pt(111) in the aqueous electrochemical environment. *Journal of Chemical Physics* 101, 10 (**1994**) 9113-9121.

[38] N. M. Markovic, B. N. Grgur, C. A. Lucas and P. N. Ross. Electrooxidation of CO and H_2/CO mixtures on Pt(111) in acid solutions. *Journal of Physical Chemistry B* 103, 3 (**1999**) 487-495.

[39] E. Herrero, J. Li and H. D. Abruna. Electrochemical, in-situ surface EXAFS and CTR studies of CO monolayers irreversibly adsorbed onto Pt(111). *Electrochimica Acta* 44, 14 (**1999**) 2385-2396.

[40] K. C. Chou, N. M. Markovic, J. Kim, P. N. Ross and G. A. Somorjai. An in situ time-dependent study of CO oxidation on Pt(111) in aqueous solution by voltammetry and sum frequency generation. *Journal of Physical Chemistry B* 107, 8 (**2003**) 1840-1844.

[41] G. Q. Lu, A. Lagutchev, D. D. Dlott and A. Wieckowski. Quantitative vibrational sum-frequency generation spectroscopy of thin layer electrochemistry: CO on a Pt electrode. *Surface Science* 585, 1-2 (**2005**) 3-16.

[42] C. K. Rhee, J. M. Feliu, E. Herrero, P. Mrozek and A. Wieckowski. Auger-Electron Spectroscopy, Low-Energy-Electron Diffraction, and Electrochemistry of Carbon-Monoxide on a Pt(100) Electrode. *Journal of Physical Chemistry* 97, 38 (**1993**) 9730-9735.

[43] G. Jerkiewicz, G. Vatankhah, J. Lessard, M. P. Soriaga and Y. S. Park. Surface-oxide growth at platinum electrodes in aqueous H_2SO_4 Reexamination of its mechanism through combined cyclic-voltammetry, electrochemical quartz-crystal nanobalance, and Auger electron spectroscopy measurements. *Electrochimica Acta* 49, 9-10 (**2004**) 1451-1459.

[44] N. P. Lebedeva, M. T. M. Koper, J. M. Feliu and R. A. van Santen. Mechanism and kinetics of the electrochemical CO adlayer oxidation on Pt(111). *Journal of Electroanalytical Chemistry* 524, (**2002**) 242-251.

[45] M. T. M. Koper, T. J. Schmidt, N. M. Markovic and P. N. Ross. Potential oscillations and S-shaped polarization curve in the continuous electro-oxidation of CO on platinum single-crystal electrodes. *Journal of Physical Chemistry B* 105, 35 (**2001**) 8381-8386.

[46] K. J. J. Mayrhofer, M. Arenz, B. B. Blizanac, V. Stamenkovic, P. N. Ross and N. M. Markovic. CO surface electrochemistry on Pt-nanoparticles: A selective review. *Electrochimica Acta* 50, 25-26 (**2005**) 5144-5154.

[47] A. Wieckowski, M. Rubel and C. Gutierrez. Reactive sites in bulk carbon-monoxide electrooxidation on oxide-free platinum(111). *Journal of Electroanalytical Chemistry* 382, 1-2 (**1995**) 97-101.

[48] M. T. M. Koper, N. P. Lebedeva and C. G. M. Hermse. Dynamics of CO at the solid/liquid interface studied by modeling and simulation of CO electro-oxidation on Pt and PtRu electrodes. *Faraday Discussions* 121, (**2002**) 301-311.

[49] I. R. Epstein and J. A. Pojman. *An introduction to nonlinear chemical dynamics.* New York, Oxford University Press (**1998**).

[50] K. Krischer. in *Modern Aspect of Electrchemistry, Number 32* edited by B. E. Conway. New York, Kluwer Academic/Plenum (**1999**)

[51] K. Krischer. in *Advances in Electrochemical Science in Engineering, Volume 8,* edited by R. C. Alkire. Weinheim, Wiley VCH (**2002**)

[52] A. S. Mikhailov. *Foundations of synergetics.* Berlin, Springer (**1996**).

[53] R. Kapral and K. Showalter. *Chemical waves and patterns.* Dordrecht, Kulwar Academic Publishers (**1995**).

[54] M. T. M. Koper. in *Advances in Chemical Physics* edited by I. Prigogine and S. A. Rice. New York, Wiley (**1996**)

[55] G. Nicolis. *Introduction to nonlinear science.* Cambridge, Cambridge Univ. Press (**1995**).

[56] G. Nicolis and I. Prigogine. *Self-organization in nonequilibrium systems.* New York, Wiley (**1977**).

[57] J. D. Murray. *Mathematical Biology.* Berlin, (**1990**).

[58] E. Scholl. *Nonlinear spatio-temporal dynamics and chaos in semiconductors,.* Cambridge, Cambridge Unviersity Press (**2001**).

[59] M. C. Cross and P. C. Hohenberg. Pattern formation outside of equilibrium. *Reviews of Modern Physics* 65, 3 (**1993**) 851 - 1112.

[60] H. Haken. Cooperative phenomena in systems far from thermal equilibrium and in nonphysical systems. *Reviews of Modern Physics* 47, 1 (**1975**) 67 - 121.

[61] A. Bonnefont, H. Varela and K. Krischer. Stationary small and large amplitude patterns during bulk CO electrooxidation on platinum. *Chemphyschem* 4, 11 (**2003**) 1260-1263.

[62] A. Bonnefont, H. Varela and K. Krischer. Stationary spatial patterns during bulk CO electrooxidation on platinum. *Journal of Physical Chemistry B* 109, 8 (**2005**) 3408-3415.

[63] D. C. Azevedo, A. L. N. Pinheiro and E. R. Gonzales. *Electrochem. and Solid-State Lett.* 5, (**2002**) A51.

[64] N. M. Markovic, C. A. Lucas, A. Rodes, V. Stamenkovi and P. N. Ross. Surface electrochemistry of CO on Pt(111): anion effects. *Surface Science* 499, 2-3 (**2002**) L149-L158.

[65] A. J. Bard and L. R. Faulkner. *Electrochemical methods fundamentals and applications.* New York, Wiley (**2001**).

[66] W. Vielstich, C. H. Hamann and A. Hamnett. *Electrochemistry.* Weinheim, Wiley VCH (**1998**).

[67] J. Bockris, O.M. and A. N. Reddy. *Modern electrochemistry.* New York, Plenum (**1970**).

[68] R. Parsons. Electrical double layer: Recent experiments and theoretical developement. *Chemical Review* 90, (**1990**) 813-826.

[69] J. O. M. Bockris, M. Devanathan and K. Müller. On structure of charged interfaces. *Proc. R. Soc. Lon. Ser. A* 274, (**1963**) 55.

[70] R. Guidelli and W. Schmickler. Recent developments in models for the inter-face between a metal and an aqueous solution. *Electrochimica Acta* 45, 15-16 (**2000**) 2317-2338.

[71] D. C. Grahame. The electrical double layer and the theory of electrocapillarity. *Chemical Reviews* 41, 3 (**1947**) 441-501.

[72] M. A. V. Devanath and B. V. K. Tilak. Structure of electrical double layer at metal-solution interface. *Chemical Reviews* 65, 6 (**1965**) 635-684.

[73] F. P. Buff and F. H. Stilling. Statistical mechanical theory of double-layer structure and properties. *Journal of Chemical Physics* 39, 8 (**1963**) 1911-1923.

[74] H. L. F. v. Helmholtz. *Ann. Physik* 7, (**1853**) 337.

[75] H. L. F. v. Helmholtz. *Ann. Physik* 89, 211 (**1879**)

[76] G. Gouy. *J. Phys. Radium* 9, (**1910**) 457.

[77] D. L. Chapman. *Phil. Mag.* 25, (**1913**) 475.

[78] O. Stern. The theory of the electrolytic double shift. *Zeitschrift Fur Elektrochemie Und Angewandte Physikalische Chemie* 30, (**1924**) 508-516.

[79] P. Hänggi, P. Talkner and M. Borkovec. Reaction-rate theory: fifty years after Kramers. *Reviews of Modern Physics* 62, 2 (**1990**) 251- 341.

[80] B. E. Conway and B. V. Tilak. Behavior and characterization of kineticaly involved chemisorbed intermediates in electrocatalysis of gas evolution reaction. *Advances in Catalysis* 38, (**1993**) 1-146.

[81] M. T. M. Koper and J. H. Sluyters. Electrochemical oscillators - Their description through a mathematical-model. *Journal of Electroanalytical Chemistry* 303, 1-2 (**1991**) 73-94.

[82] M. T. M. Koper and J. H. Sluyters. A mathematical-model for current oscillations at the active passive transition in metal electrodissolution. *Journal of Electroanalytical Chemistry* 347, 1-2 (**1993**) 31-48.

[83] V. I. Arnold. *Bifurcation theory and catastrophe theory.* Berlin, Springer (**1999**).

[84] Y. A. Kuznetsov. *Elements of applied bifurcation theory.* New York, Springer (**2004**).

[85] R. Seydel. *Practical bifurcation and stability analysis.* New York, Springer (**1994**).

[86] J. H. Hubbard and B. H. West. *Differential equations: A dynamical system approach higher dimensional systems.* New York, Springer (**1995**).

[87] S. H. Strogatz. *Nonlinear dynamics and chaos with applications to physics, biology, chemistry, and engineering.* Reading, Addison Wesley (**1994**).

[88] J. M. Thompson and H. B. Stewart. *Nonlinear dynamics and chaos.* New York, Wiley (**2002**).

[89] H. Varela. Phd Thesis, Spatiotemporal pattern formation during electrochemical oxidation of hydrogen on platinum. (**2003**) Free University Berlin, Berlin.

[90] K. Krischer, N. Mazouz and G. Flatgen. Pattern formation in globally coupled electrochemical systems with an S-Shaped current-potential curve. *Journal of Physical Chemistry B* 104, 31 (**2000**) 7545-7553.

[91] Y. J. Li, J. Oslonovitch, N. Mazouz, F. Plenge, K. Krischer and G. Ertl. Turing-type patterns on electrode surfaces. *Science* 291, 5512 (**2001**) 2395-2398.

[92] P. Strasser, M. Eiswirth and M. T. M. Koper. Mechanistic classification of electrochemical oscillators - operational experimental strategy. *Journal of Electroanalytical Chemistry* 478, 1-2 (**1999**) 50-66.

[93] K. Krischer. New directions and challenges in electrochemistry - Spontaneous formation of spatiotemporal patterns at the electrode vertical bar electrolyte interface. *Journal of Electroanalytical Chemistry* 501, 1-2 (**2001**) 1-21.

[94] K. Krischer, N. Mazouz and P. Grauel. Fronts, waves, and stationary patterns in electrochemical systems. *Angewandte Chemie International Edition* 40, 5 (**2001**) 850-869.

[95] A. Groß. *Theoretical surface science.* Berlin, Springer (**2003**).

[96] P. J. Feibelman and D. R. Hamann. Electronic structure of a "poisoned" transition-metal surface. *Physical Review Letters* 52, 1 (**1984**) 61- 64.

[97] J. Harris and S. Andersson. H_2 dissociation at metal surfaces. *Physical Review Letters* 55, 15 (**1985**) 1583 - 1586.

[98] G. Blyholder. Molecular orbital view of chemisorbed carbon monoxide. *Journal of Physical Chemistry* 68, 10 (**1964**) 2772-2778.

[99] T. Engel and G. Ertl. Elementary steps in the catalytic oxidation of carbon monoxide on platinum metals. *Advances in Catalysis* 28, (**1983**) 1-78.

[100] P. J. Feibelman, B. Hammer, J. K. Norskov, F. Wagner, M. Scheffler, R. Stumpf, R. Watwe and J. Dumesic. The CO/Pt(111) puzzle. *Journal of Physical Chemistry B* 105, 18 (**2001**) 4018-4025.

[101] B. E. Conway. Electrochemical oxide film formation at noble-metals as a surface-chemical process. *Progress in Surface Science* 49, 4 (**1995**) 331-452.

[102] B. V. Tilak, B. E. Conway and H. Angersteinkozlowska. Real condition of oxidized Pt electrodes 3. Kinetic-theory of formation and reduction of surface oxides. *Journal of Electroanalytical Chemistry* 48, 1 (**1973**) 1-23.

[103] B. E. Conway, B. Barnett, H. Angersteinkozlowska and B. V. Tilak. A surface-electrochemical basis for the direct logarithmic growth law for initial-stages of extension of anodic oxide-films formed at noble-metals. *Journal of Chemical Physics* 93, 11 (**1990**) 8361-8373.

[104] H. Angersteinkozlowska, B. E. Conway and W. B. A. Sharp. Real condition of electrochemically oxidized platinum surfaces 1. Resolution of component processes. *Journal of Electroanalytical Chemistry* 43, 1 (**1973**) 9-36.

[105] V. I. Birss, M. Chang and J. Segal. Platinum oxide film formation reduction - an in-situ mass measurement study. *Journal of Electroanalytical Chemistry* 355, 1-2 (**1993**) 181-191.

[106] D. A. Harrington. Simulation of anodic Pt oxide growth. *Journal Electroanalytical Chemistry* 420, (**1997**) 101 - 109.

[107] G. Vatankhah, J. Lessard, G. Jerkiewicz, A. Zolfaghari and B. E. Conway. Dependence of the reliability of electrochemical quartz-crystal nanobalance mass responses on the calibration constant, C-f: analysis of three procedures for its determination. *Electrochimica Acta* 48, 11 (**2003**) 1613-1622.

[108] M. Alsabet, M. Grden and G. Jerkiewicz. Comprehensive study of the growth of thin oxide layers on Pt electrodes under well-defined temperature, potential and time conditions. *Journal of Electroanalytical Chemistry* 589, (**2006**) 120-127.

[109] I. Siegmeir. Diploma Thesis (**2005**) Technical University Munich, Munich.

[110] M. W. Breiter. Double layer capacity and methanol coverage on platinum in perchloric acid solution. *Electrochimica Acta* 7, 5 (**1962**) 533-542.

[111] V. S. Bagotzky, Y. B. Vassiyev, J. Weber and J. Pirtskha. Adsorption of anions on smooth platinum electrodes. *Journal of Electroanalytical Chemistry* 27, 1 (**1970**) 31.

[112] D. M. Novak and B. E. Conway. Competitive adsorption and state of charge of halide-ions in monolayer oxide film growth-processes at Pt anodes. *Journal of the Chemical Society-Faraday Transactions I* 77, (**1981**) 2341-2359.

[113] H. Angersteinkozlowska, B. E. Conway, B. Barnett and J. Mozota. Role of ion adsorption in surface oxide formation and reduction at noble-metals - General features of the surface process. *Journal of Electroanalytical Chemistry* 100, 1-2 (**1979**) 417-446.

[114] R. I. Masel. *Principles of adsorption and reaction on solid surfaces.* New York, Wiley (**1996**).

[115] K. W. Kolasinski. *Surface science foundations of catalysis and nanoscience.* Chichester, Wiley (**2002**).

[116] V. P. Zhdanov and B. Kasemo. Simulation of CO electrooxidation on nm-sized supported Pt particles: stripping voltammetry. *Chemical Physics Letters* 376, 1-2 (**2003**) 220-225.

[117] F. C. Tomkins. *Chemisorption of gases on metals.* London, Academic Press (**1978**).

[118] S. D. Kevin, D. C. Skelton and D. H. Wei. Molecular interaction and simple surface processes. *Crit. Rev. Surf. Chem.* 4, (**1994**) 77-140.

[119] E. E. Mola, D. A. King, I. M. IIrurzun, M. Rafti and J. L. Vicente. Embedded mean field approach to analyzing pattern formation in surface chemical reaction. *Surface Review and Letters* 11, 1 (**2004**) 57-70.

[120] F. Zaera. Kinetics of chemical reactions on solid surfaces: Deviations from conventional theory. *Accounts of Chemical Research* 35, 2 (**2002**) 129-136.

[121] M. D. Xu, J. Y. Liu and F. Zaera. Kinetic evidence for the dependence of surface reaction rates on the distribution of reactants on the surface. *Journal of Chemical Physics* 104, 21 (**1996**) 8825-8828.

[122] M. Silverberg and A. Ben-Shaul. Adsorbate islanding in surface reactions: A combined Monte Carlo-lattice gas approach. *The Journal of Chemical Physics* 87, 5 (**1987**) 3178-3194.

[123] M. Eiswirth, A. Freund and J. Ross. in *Advances in Chemical Physics Vol-80* edited by I. Prigogine and S. A. Rice. New York, Wiley (**1991**)

[124] L. A. Kibler, A. Cuesta, M. Kleinert and D. M. Kolb. In-situ STM characterisation of the surface morphology of platinum single crystal electrodes as a function of their preparation. *Journal of Electroanalytical Chemistry* 484, 1 (**2000**) 73-82.

[125] I. M. Tidswell, N. M. Markovic and P. N. Ross. Potential-dependent surface relaxation of the Pt(001) electrolyte interface. *Physical Review Letters* 71, 10 (**1993**) 1601-1604.

[126] C. A. Lucas, N. M. Markovic and P. N. Ross. Surface structure and relaxation at the Pt(110)/electrolyte interface. *Physical Review Letters* 77, 24 (**1996**) 4922-4925.

[127] N. M. Markovic, H. A. Gasteiger and P. N. Ross. Oxygen reduction on platinum low-Index single-crystal surfaces in sulfuric acid solution - Rotating ring - Pt(hkl) - disk Studies. *Journal of Physical Chemistry* 99, 11 (**1995**) 3411-3415.

[128] T. J. Schmidt, P. N. Ross and N. M. Markovic. Temperature-dependent surface electrochemistry on Pt single crystals in alkaline electrolyte: Part 1: CO oxidation. *Journal of Physical Chemistry B* 105, 48 (**2001**) 12082-12086.

[129] A. C. Gutierrez, A. L. N. Pinheiro, E. Leiva, E. R. Gonzalez and T. Iwasita. Abnormally fast mobility of CO at electrochemical interfaces. *Electrochemistry Communications* 5, 7 (**2003**) 539-543.

[130] A. V. Tripkovic, K. D. Popovic and J. D. Lovic. The influence of the oxygen-containing species on the electrooxidation of the C1–C4 alcohols at some platinum single crystal surfaces in alkaline solution. *Electrochimica Acta* 46, 20 (**2001**) 3163-3173.

[131] N. Hoshi, A. Sakurada, S. Nakamura, S. Teruya, O. Koga and Y. Hori. Infrared Reflection Absorption Spectroscopy of sulfuric acid anion adsorbed on stepped surfaces of platinum single-crystal electrodes. *Journal of Physical Chemistry B* 106, 8 (**2002**) 1985 - 1990.

[132] J. Clavilier. in *Interfacial Electrochemistry: Theory: Experiment, and Applications* edited by A. Wieckowski. New York, Marcel Dekker Inc. (**1999**)

[133] N. P. Lebedeva, M. T. M. Koper, J. M. Feliu and R. A. van Santen. The effect of the cooling atmosphere in the preparation of flame-annealed Pt(111) electrodes on CO adlayer oxidation. *Electrochemistry Communications* 2, 7 (**2000**) 487-490.

[134] J. Clavilier, R. Faure, G. Guinet and R. Durand. Preparation of mono-crystalline Pt microelectrodes and electrochemical study of the plane surfaces cut in the direction of the (111) and (110) planes. *Journal of Electroanalytical Chemistry* 107, 1 (**1980**) 205-209.

[135] C. G. M. Hermse, A. P. van Bavel, M. T. M. Koper, J. J. Lukkien, R. A. van Santen and A. P. J. Jansen. Modelling the butterfly: (root 3 x root 7) ordering on fcc(111) surfaces. *Surface Science* 572, 2-3 (**2004**) 247-260.

[136] K. Aljaafgolze, D. M. Kolb and D. Scherson. On the voltammetry curves of Pt(111) in aqueous-solutions. *Journal of Electroanalytical Chemistry* 200, 1-2 (**1986**) 353-362.

[137] E. Ott, C. Grebogi and J. A. Yorke. Controlling chaos. *Physical Review Letters* 64, 11 (**1990**) 1196 - 1199.

[138] B. Peng, V. Petrov and K. Showalter. Controlling chemical chaos. *Journal of Physical Chemistry* 95, 13 (**1991**) 4957-4959.

[139] R. W. Rollins, P. Parmananda and P. Sherard. Controlling chaos in highly dissipative systems: A simple recursive algorithm. *Physical Review E* 47, 2 (**1993**) R780-R783.

[140] W. L. Ditto, S. N. Rauseo and M. L. Spano. Experimental control of chaos. *Physical Review Letters* 65, 26 (**1990**) 3211- 3214.

[141] E. R. Hunt. Stabilizing high-period orbits in a chaotic system: The diode resonator. *Physical Review Letters* 67, 15 (**1991**) 1953 - 1955.

[142] C. Reyl, L. Flepp, R. Badii and E. Brun. Control of NMR-laser chaos in high-dimensional embedding space. *Physical Review E* 47, 1 (**1993**) 267-272.

[143] R. Roy, T. W. Murphy, T. D. Maier, Z. Gills and E. R. Hunt. Dynamical control of a chaotic laser: Experimental stabilization of a globally coupled system. *Physical Review Letters* 68, 9 (**1992**) 1259-1262.

[144] P. Parmananda, P. Sherard, R. W. Rollins and H. D. Dewald. Control of chaos in an electrochemical cell. *Physical Review E* 47, 5 (**1993**) R3003 - R3006.

[145] K. Pyragas. Continuous control of chaos by self-controlling feedback. *Physics Letters A* 170, 6 (**1992**) 421-428.

[146] W. Just, T. Bernard, M. Ostheimer, E. Reibold and H. Benner. Mechanism of time-delayed feedback control. *Physical Review Letters* 78, 2 (**1997**) 203 - 206.

[147] E. C. Zimmermann and J. Ross. Light induced bistability in $S_2O_6F_2$ - 2 SO_3F: Theory and experiment. *The Journal of Chemical Physics* 80, 2 (**1984**) 720-729.

[148] A. Hjelmfelt and J. Ross. Experimental stabilization of unstable steady states in oscillatory and excitable reaction systems. *Journal of Physical Chemistry* 98, 4 (**1994**) 1176-1179.

[149] Z. Gills, C. Iwata, R. Roy, I. B. Schwartz and I. Triandaf. Tracking unstable steady states: Extending the stability regime of a multimode laser system. *Physical Review Letters* 69, 22 (**1992**) 3169 - 3172.

[150] A. Rutherford and N. R. Amundson. An analysis of chemical reactor stability and control-I : The possibility of local control, with perfect or imperfect control mechanisms. *Chemical Engineering Science* 7, 3 (**1958**) 121-196.

[151] E. C. Zimmermann, M. Schell and J. Ross. Stabilization of unstable states and oscillatory phenomena in an illuminated thermochemical system: Theory and experiment. *The Journal of Chemical Physics* 81, 3 (**1984**) 1327-1336.

[152] B. Macke, J. Zemmouri and N. E. Fettouhi. Stabilization of unstable stationary states in optical bistability. *Physical Review A* 47, 3 (**1993**) R1609 - R1611.

[153] H.-C. Chang and L.-H. Chen. Bifurcation characteristics of nonlinear systems under conventional pid control. *Chemical Engineering Science* 39, 7-8 (**1984**) 1127-1142.

[154] P. Parmananda, M. A. Rhode, G. A. Johnson, R. W. Rollins, H. D. Dewald and A. J. Markworth. Stabilization of unstable steady states in an electrochemical system using derivative control. *Physical Review E* 49, 6 (**1994**) 5007 - 5011.

[155] J. P. Laplante. Stabilization of unstable states in the bistable iodate-arsenous acid reaction in a continuous flow stirred tank reactor. *Journal of Physical Chemistry* 93, 10 (**1989**) 3882 - 3885.

[156] I. Z. Kiss, Z. Kazsu and V. Gaspar. Experimental strategy for characterization of essential dynamical variables in oscillatory systems: Effect of double-layer capacitance on the stability of electrochemical oscillators. *Journal of Physical Chemistry A* 109, 42 (**2005**) 9521-9527.

[157] P. Strasser, M. Eiswirth and G. Ertl. Oscillatory instabilities during formic acid oxidation on Pt(100), Pt(110) and Pt(111) under potentiostatic control. 2. Model calculations. *Journal of Chemical Physics* 107, 3 (**1997**) 991-1003.

[158] S. C. Chang and M. J. Weaver. Coverage-dependent and potential-dependent binding geometries of carbon-monoxide at ordered low-Index platinum aqueous and rhodium aqueous interfaces - Comparisons with adsorption in corresponding metal vacuum environments. *Surface Science* 238, 1-3 (**1990**) 142-162.

[159] F. C. Nart, T. Iwasita and M. Weber. Sulfate adsorption on well-defined Pt(100) electrodes. *Electrochimica Acta* 39, 13 (**1994**) 2093-2096.

[160] T. Iwasita, F. C. Nart, A. Rodes, E. Pastor and M. Weber. Vibrational spectroscopy at the electrochemical interface. *Electrochimica Acta* 40, 1 (**1995**) 53-59.

[161] A. Frumkin. Hydrogen overvoltage and the structure of the double layer. *Zeitschrift Fur Physikalische Chemie-Abteilung a-Chemische Thermodynamik Kinetik Elektrochemie Eigenschaftslehre* 164A, (**1933**) 121-133.

[162] A. Frumkin. Adsorptionserscheinungen Und Elektrochemische Kinetik. *Zeitschrift Fur Elektrochemie* 59, 7-8 (**1955**) 807-822.

[163] R. Parsons. Effect of specific adsorption on rate of an electrode process. *Journal of Electroanalytical Chemistry* 21, 1 (**1969**) 35-43.

[164] M. Breiter, M. Kleinerman and P. Delahay. Structure of the double layer and electrode processes. *Journal of the American Chemical Society* 80, 19 (**1958**) 5111-5117.

[165] B. Timmer, Sluyters.M and J. H. Sluyters. Electrode kinetics and double layer structure. *Surface Science* 18, 1 (**1969**) 44-59.

[166] K. Asada, P. Delahay and A. K. Sundaram. Local field effect and failure of double layer correction in electrode kinetics. *Journal of the American Chemical Society* 83, 16 (**1961**) 3396-3400.

[167] J. M. Parry and R. Parsons. Adsorption of aromatic sulphonates at a mercury electrode .1. Sodium benzene M-disulphonate. *Transactions of the Faraday Society* 59, 481 (**1963**) 241-256.

[168] M. E. Gamboaaldeco, E. Herrero, P. S. Zelenay and A. Wieckowski. Adsorption of bisulfate anion on a Pt(100) electrode - a comparison with Pt(111) and Pt(Poly). *Journal of Electroanalytical Chemistry* 348, 1-2 (**1993**) 451-457.

[169] Y. A. Kuznetsov. CONTENT - Integrated environment for analysis of dynamical systems. (**1998**)

[170] O. M. Magnussen. Ordered anion adlayers on metal electrode surfaces. *Chemical Review* 102, (**2002**) 679-725.

[171] A. M. Funtikov, U. Linke, U. Stimming and R. Vogel. An in-situ STM study of anion adsorption on Pt(111) from sulfuric-acid-solutions. *Surface Science* 324, 1 (**1995**) L343-L348.

[172] A. M. Funtikov, U. Stimming and R. Vogel. Anion adsorption from sulfuric acid solutions on Pt(111) single crystal electrodes. *Journal of Electroanalytical Chemistry* 428, 1-2 (**1997**) 147-153.

[173] O. M. Magnussen, J. Hageböck, J. Hotlos and R. J. Behm. In situ scanning tunnelling microscopy observations of a disorder - order phase transition in hydrogensulfate adlayers on Au(111). *Faraday Discussions* 94, (**1992**) 329.

[174] G. J. Edens, X. Gao and M. J. Weaver. The adsorption of sulfate on Au(111) in acidic aqueous-media - Adlayer structural inferences from Infrared-Spectroscopy and Scanning-Tunneling-Microscopy. *Journal Electroanalytical Chemistry* 375, (**1994**) 357.

[175] W. Savich, S. G. Sun, J. Lipkowski and A. Wieckowski. Determination of the Sum of Gibbs Excesses of Sulfate and Bisulfate Adsorbed at the Pt(111) Electrode Surface Using Chronocoulometry and Thermodynamics of the Perfectly Polarized Electrode. *Journal of Electroanalytical Chemistry* 388, 1-2 (**1995**) 233-237.

[176] D. M. Kolb. An atomistic view of electrochemistry. *Surface Science* 500, 1-3 (**2002**) 722-740.

[177] S. L. Chen, D. Lee and M. Schell. Enhancement of the electrochemical oxidation of formic acid. Effects of anion adsorption and variation of rotation rate. *Electrochimica Acta* 46, 23 (**2001**) 3481-3492.

[178] S. L. Chen, D. Lee and M. Schell. Increases in reaction rates and improvement of current-potential characteristics in the electrochemical oxidation of formic acid. *Electrochemistry Communications* 3, 2 (**2001**) 81-85.

[179] B. E. K. Swamy, C. Vannoy, J. Maye and M. Schell. Increases in reaction rates achieved by replacing anions in the electrolyte with more inhibiting ones. *Electrochemistry Communications* 6, 10 (**2004**) 1032-1036.

[180] N. Markovic and P. N. Ross. The effect of specific adsorption of ions and underpotential deposition of copper on the electrooxidation of methanol on platinum single-crystal surfaces. *Journal of Electroanalytical Chemistry* 330, 1-2 (**1992**) 499-520.

[181] A. Zolfaghari, B. E. Conway and G. Jerkiewicz. Elucidation of the effects of competitive adsorption of Cl^- and Br^- ions on the initial stages of Pt surface oxidation by means of electrochemical nanogravimetry. *Electrochimica Acta* 47, 8 (**2002**) 1173-1187.

[182] B. E. Conway, A. Zolfaghari, W. G. Pell and G. Jerkiewicz. Voltammetry, nanogravimetry and double-layer capacitance studies on chemisorption of Cl^- and Br^-, competitive with potential-dependent electrosorption of O species at Pt electrodes. *Electrochimica Acta* 48, 25-26 (**2003**) 3775-3778.

[183] B. E. Conway and D. M. Novak. Chloride-ion adsorption effects in the recombination-controlled kinetics of anodic chlorine evolution at Pt electrodes. *Journal of the Chemical Society-Faraday Transactions I* 75, (**1979**) 2454-2472.

[184] B. E. Conway and D. M. Novak. Electrocatalytic effect of the oxide film at Pt anodes on Cl recombination kinetics in chlorine evolution. *Journal of Electroanalytical Chemistry* 99, 2 (**1979**) 133-156.

[185] B. E. Conway and J. Mozota. Chloride-ion effects on the reversible and irreversible surface oxidation processes at Pt electrodes, and on the growth of monolayer oxide-films at Pt. *Journal of the Chemical Society-Faraday Transactions I* 78, (**1982**) 1717-1732.

[186] M. C. Perez, A. Rincon and C. Gutierrez. Effect of chloride ions on the electrooxidation at low potentials of dissolved carbon monoxide on platinum. *Journal of Electroanalytical Chemistry* 511, 1-2 (**2001**) 39-45.

[187] S. B. Hall, E. A. Khudaish and A. L. Hart. Electrochemical oxidation of hydrogen peroxide at platinum electrodes. Part V: inhibition by chloride. *Electrochimica Acta* 45, 21 (**2000**) 3573-3579.

[188] A. Lopez-Cudero, A. Cuesta and C. Gutierrez. The effect of chloride on the electrooxidation of adsorbed CO on polycrystalline platinum electrodes. *Journal of Electroanalytical Chemistry* 548, (**2003**) 109-119.

[189] J. Bolton. Diploma Thesis (**2006**) Technical University Munich, Munich.

Acknowledgement

First of all, I would like to thank Prof. Katharina Krischer for giving me an opportunity to work on a very interesting field of natural science in one of the world best scientific institution. I am grateful to her for suggesting the research direction, non-stop support, active discussion, encouragement and help. Likewise I would like to thank Prof. G. Ertl, Dr. B. Pettinger (FHI Berlin), Prof. J. Wintterlin (LMU Munich) and Dr. P. Faulner (TUM Physics) for their help regarding the experimental methods. And I gratefully acknowledge the help of Prof. A. Bonnefont, Prof. A. Birzu, Dr. H. Varela and Prof. E. Savinova throughout my work.

I would like to thank Ms. I. Miethe, Mr. J. Siegmeier, Mr. P. Bauer, Mr. R. Hoelzel, Ms. T. Pourrostami, Dr. N. Baba, Mr. J. Bolten, Dr. V. G. Morales and all members of Prof. Stimming group for their valuable help and encouragement during my stay in Munich. Specially, I would like to thank Mr. S. Scheirer, Mr. G. Mueller and to all employees from the mechanical workshop in physics dep. TUM for the preparation of the experimental setup.

I would also like to mention the persons who inspired and motivate me for the study of physics, my first physics teacher Tapan Kumar Bhattacharjee (Nimta High School), Dr. Kalobaron Maity (Presidency College), Dr. P. Mukherjee, Dr. K. Mitra, Dr. B.K. Majumdar, Dr. A. Som, Dr. G.B. Mukherjee, Dr. K.B. Choudhury and Dr. S. Mukhopadhyay (BKC College Kolkata), Dr. P.N. Banerjee (Surendranath College), Prof. D. Ghosh, Prof. K.K. Chottopadhyay, Prof. N. Banerjee, Prof. A. Manna, Prof. A. M. Basu, Prof. D.P. Bhattacharya, Prof. D. Lohar, and Dr. N.B. Manik, Prof. Manoranjan Khan, Prof. Dipankar Ray (Jadavpur University), Prof. K. Gopakumar, Prof. S.K. Sinha (Indian Institute of Science), Dr. V.T. Somasekhar (RE College Warangal) and Prof. B.N. Biswas (Burdwan University). I would like to thank my wife Mrs. Paramita Das for

her support during my stay in Munich. Further I would like to thank Vineet, Arnab, Suresh, Aparna, Shaw, Nithu, Nina, Mani, Sudha, Subhasis, Kiron, Somnath, Amjad, Ruhi, Vinod, Shital, Arvind, Mainakda, Piudi, Supratik Das and Shaktivhel for their support and help. I would like to thank Mrs. Chakrabarti from German Consulate, Kolkata for her help during the thesis submission. Finally, I would like to thank Mrs. K. Wilson and all employees of the office of the Dep. of Physics, TUM for their valuable assist throughout my stay in Munich.

List of Publications

1. S. Malkhandi, A. Bonnefont, K. Krischer. Strictly potentiostatic current oscillations during bulk CO electro-oxidation on platinum in the presence of inhibiting anions. *Electrochemistry Communications*, 7, (**2005**), 710–716.

2. S. Malkhandi, A. Bonnefont, K. Krischer. Dynamic instabilities during the continuous electro-oxidation of CO on poly- and single crystalline Pt electrodes. *Communicated.*